University of Massachusetts Amherst
ScholarWorks@UMass Amherst

Masters Theses 1911 - February 2014

2011

# Terahertz Radiation From Single Walled Carbon Nanotubes

Martin M. Muthee
*University of Massachusetts Amherst*

Follow this and additional works at: https://scholarworks.umass.edu/theses

Part of the Electromagnetics and Photonics Commons, and the Nanotechnology Fabrication Commons

Muthee, Martin M., "Terahertz Radiation From Single Walled Carbon Nanotubes" (2011). *Masters Theses 1911 - February 2014*. 701.
Retrieved from https://scholarworks.umass.edu/theses/701

This thesis is brought to you for free and open access by ScholarWorks@UMass Amherst. It has been accepted for inclusion in Masters Theses 1911 - February 2014 by an authorized administrator of ScholarWorks@UMass Amherst. For more information, please contact scholarworks@library.umass.edu.

# Terahertz Radiation from Single Walled Carbon Nanotubes

A Thesis Presented

by

MARTIN M. MUTHEE

Submitted to the Graduate School of the
University of Massachusetts Amherst in partial fulfillment
of the requirements for the degree of
Master of Science in Electrical and Computer Engineering

September 2011

Electrical and Computer Engineering

© Copyright Martin Muthee 2011
All Rights Reserved

# Terahertz Radiation from Single Walled Carbon Nanotubes

A Thesis Presented

by

MARTIN M. MUTHEE

Approved as to style and content by the thesis committee:

Sigfrid Yngvesson, *Chair*

Eric Polizzi, *Member*

Robert Jackson, *Member*

C. V. Hollot, *Department Head*
Electrical and Computer Engineering

*Dedicated to my family*

## ACKNOWLEDGEMENTS

I would like to express my deepest gratitude to my adviser Dr. Sigfrid Yngvesson, for the opportunity to work in his lab and the guidance he has offered throughout the course of this work. His zealousness and commitment has truly been an inspiration to me. This work would undoubtedly not have been possible without his support and input. To him, I will forever be thankful.

I would also like to thank the other members of the committee, Professors Eric Polizzi and Robert Jackson, who in their capacity as teachers provided a unique and enjoyable classroom learning experience. Furthermore for agreeing to serve as my thesis committee members.

I would also like to thank the CHM Nanofabrication lab manager, John Nicholson, for teaching me almost all that I know about fabrication. He ostensibly knows everything about fabrication and offered the best hands-on training one could have ever asked for.

Many thanks to the THz lab mates, Ric Zanoni, Kan Fu, Jason Donovan, Benjamin St. Peter, for their useful discussions and help in the lab, and especially to Enrique Carrion whom I worked closely with to develop the many experimental methods. Thanks also to Yiming Chen for help with e-beam lithography. Finally I would like to thank my family for being very supportive and encouraging: I thank you all.

**ABSTRACT**

**TERAHERTZ RADIATION FROM SINGLE WALLED CARBON NANOTUBES**

SEPTEMBER 2011

MARTIN MUTHEE

B.S.E.C.E, UNIVERSITY OF MASSACHUSETTS AMHERST

M.S.E.C.E, UNIVERSITY OF MASSACHUSETTS AMHERST

**Directed by: Dr. Sigfrid Yngvesson**

The Terahertz region of the electromagnetic spectrum is the region between microwaves and infra-red, dubbed the terahertz 'gap' due to its relative underdevelopment in terms of technology. This region is marked by expensive and inconvenient sources that are bulky or that require cryogenic cooling for normal operation, therefore creating a need for cheap and easy to use terahertz sources.

Carbon nanotubes have received considerable attention since their discovery due to their unique physical and electronic properties. Many applications have been proposed using especially Single-Walled Carbon Nanotubes (SWCNTs), and a number of commercial technologies exist. In this work, we have proposed to use SWCNTs as the basis for a cheap, compact and room temperature-operating Terahertz source.

We have characterized the SWCNT source, and we present results on transport characteristics (I–V curves), radiation patterns, spectra, polarization as

well as optical, SEM and AFM imaging. We show that the radiation spectrum is determined by integrated antennas coupled to the SWCNTs, and preliminary power calibration indicates that the radiated power exceeds the power predicated by the Nyquist formula.

# TABLE OF CONTENTS

Page

**ACKNOWLEDGEMENTS** ..... **v**

**ABSTRACT** ..... **vi**

**LIST OF TABLES** ..... **vii**

**LIST OF FIGURES** ..... **ix**

**CHAPTER**

**1. INTRODUCTION** ..... **1**

1.1 Overview ..... 1
1.2 Terahertz Sources ..... 2
1.3 Carbon Nanotube Basics ..... 5

1.3.1 Synthesis ..... 5
1.3.2 Physical Structure ..... 6
1.3.3 Bandstructure ..... 8
1.3.4 Electronic transport ..... 10

1.3.4.1 Ballistic versus diffusive regimes ..... 12
1.3.4.2 Scattering processes ..... 12
1.3.4.3 Contact resistance ..... 13

**2. BACKGROUND AND MOTIVATION** ..... **15**

2.1 Blackbody Radiation ..... 15
2.2 Light Emission From Single Walled Carbon Nanotubes. ..... 17
2.3 Carbon Nanotubes and Terahertz ..... 22

2.3.1 Absorption Measurements ..... 22
2.3.2 Terahertz Time Domain Spectroscopy Experiments ..... 26
2.3.3 Review of EM Calculations ..... 28

2.3.3.1 Terahertz Conductivity Peak....34

2.3.4 Antenna and Silicon Lens coupling ....35

2.3.4.1 Single Mode Antenna Theorem....36
2.3.4.2 Silicon Lens Coupling....36

**3. EXPERIMENTAL METHODS....38**

3.1 Fabrication....38
3.2 Dielectrophoresis....40
3.3 Transport Measurements....43
3.4 Terahertz Detectors....43
3.5 Power Calibration....45
3.6 Beam Pattern Measurements....46
3.7 Fourier Transform Spectrometer(FTS)....47

3.7.1 Basic Operation....48
3.7.2 Interferogram Fourier Transform....50
3.7.3 Implementation....52

**4. RESULTS and DISCUSSIONS....58**

4.1 Devices....58
4.2 Transport Measurements....63

4.2.1 Current Saturation....64
4.2.2 Contact Barriers....65
4.2.3 Annealing....67

4.3 Radiation Patterns....69
4.4 Spectra....72

4.4.1 Device Comparison....74
4.4.2 Bias Dependence....78

4.5 Polarization....80
4.6 Power Considerations....80

**5. FUTURE WORK** ..... **85**

5.1 Antenna Designs ..... 85
5.2 Terahertz Detection Using Patch Antennas. ..... 86
5.3 Terahertz integrated circuits ..... 86

**APPENDIX** ..... **87**

A : PROCESS PARAMETERS ..... 87
B : INTERFEROGRAMS AND SPECTRA ..... 89
C: BOLOMETER FILTER TRANSMISSION CURVES ..... 112

**BIBLIOGRAPHY** ..... **113**

## LIST OF TABLES

**Table** **Page**

1.1 Comparison of commonly used THz sources .....4

4.1 Typical Results from polarization measurements.....80

## LIST OF FIGURES

**Figure** **Page**

1.1 Electromagnetic spectrum showing the microwave, terahertz and infra red regimes.....3

1.2 Power versus frequency comparisons for various terahertz sources [8].....4

1.3 (left) Sheet of graphene (right) rolled up sheet to form a SWCNT [14]....7

1.4 Graphene section showing basis vectors $a_1$ and $a_2$.....8

1.5 Band structure diagrams (left plots) and the resulting density of states (right plots) for (10,0) and (5,5) SWCNTs.....9

1.6 (a) DOS diagram showing a small band gap near zero[19] (b) (top panel) band gap dependence on the radius- top curves are semiconducting SWCNTs, middle curves are quasi-metallic SWCNTs and bottom curves are metallic SWCNTs. (bottom panel) close up of top [16].....10

1.7 Illustration of a SWCNT bridging two metal contacts.....10

1.8 Energy band diagram showing various scattering processes [21].....13

1.9 I-V characteristics for (a) low resistance contacts and (b) high resistance contacts. Inset is SEM picture of the device [22].....14

2.1 Blackbody emission spectrum at various temperatures.....17

2.2 Emission spectrum for a (4,0) SWCNT.....18

2.3 DOS diagram illustrating the thermal light emission. The curve on the blue region corresponds to the electron population at various energies calculated by multiplying the DOS (black line) and the Fermi-Dirac distribution function (red line) at 1200K. $E_{11}$ and $E_{22}$ are the energies associated with first and second VHS respectively.(b) The emission spectra for the supported and suspended parts of the tube. Inset shows the SEM picture of the device [25].....19

2.4 (a)Light emission spectra in the infrared for three 2um long QM-SWNTs (red,green and blue) at a gate voltage of -20V and biased at V = 1.4, 1.1, 1.3V respectively.(b) Corresponding emission spectra for the three tubes in the visible range. V=1.5, 1.3,1.5 respectively [25].....20

2.5 Illustration of a SWCNT device with supported and suspended sections [26].....20

2.6 (a) Emisson spectrum of suspended (lower curve) and supported (upper curve)sections of the same tube. Redlines represent Lorentzian fits to the results and the green lines are fits to the individual peaks. (b) Illustration showing various emission processes- direct $M_{11}$(a-b), phonon assisted (c-d-b) Black dots denote excitons. The phonon-assisted emission energy is $M_{11} + \Delta E - E$ph, where $M_{11}$ is the lowest excitonic transition energy for metallic SWCNTs, $\Delta E$ is the average energy difference between the excitons at "c" and the excitons at "a", and $E$ph is the phonon energy [26].....21

2.7 Absorbance spectra for purified SWCNT films [29].....23

2.8 Schematic representation of the density of states (DOS) of SWCNTs contributing to the near-IR and far-IR absorption [29].....24

2.9 Optical conductivity curves from SWCNT films synthesized differently [30].....24

2.10 Optical conductivity curves for a SWCNT film sample at various temperatures [31].....25

2.11 (a) Frequency dependence of the dielectric function and best fits to the data (solid lines) (b) Conductivity with Lorentz and Drude model fits [34].....27

2.12 Dots: experimental dependence of the photoconductive component *UPh* on excitation frequency left scale. Lines: calculated absorbance of SWCNT plates of thickness *d* right scale. Inset: the experimental photoconductive component vs laser power [36].....28

2.13 Input impedance for a 10um SWCNT and TDBA copper of the same length. Squares denote the resonances [37].....31

2.14 Frequency dependence of the imaginary part of the polarizability for an individual and a bundle of SWCNTs of 1um length [40].....33

2.15 Thermal radiation spectra from a metallic SWCNT with L=1um, at distances of 0.5L (black solid line) and 100L (blue dotted line) [40].....33

2.16 Absorption as a function of frequency for a SWCNT with various mean free paths as indicated. 0.5,0.1,0.02 represent clean, intermediate and dirty SWCNTs respectively [39].....35

2.17 Circuit diagram representation of a SWCNT coupled to an antenna.....36

2.18 Illustration showing coupling to a Silicon lens. Red section indicating a point source and the resulting radiation shown by the extended lines....37

2.19 Schematic showing ray tracing from an off-center source and the resulting tilted wavefront [43].....37

3.1 Results of development after UV lithography.....38

3.2 Optical Images showing the results of the second lithography step.....39

3.3 DEP set-up.....41

3.4 Current versus time graph during the DEP process.....42

3.5 SMA connected block showing mounted device.....43

3.6 Illustration showing the cross section of the dewar [54].....45

3.7 Picture showing the beam pattern measurement set- up.....47

3.8 Illustration of the Fourier transform spectrometer [58].....48

3.9 (left) Interferogram from a SiC source, with the resulting spectrum (right).....49

3.10 Beam intensities at various sections of the interferometer.....50

3.11 Mylar beam splitter efficiencies for 23, 12, 6 and 3.5*um* mylar thickness [59].....54

3.12 (a) Illustration of the FTS set-up. (b)Picture of actual FTS set-up used in measurements; Radiation from the source is collimated by OAP1 and directed to the beam splitter, where it is split into two beams, one towards the movable mirror (M1) and the other towards the fixed mirror (M2). Upon reflection, the two beams combine and part of the resulting beam is sent to the focusing mirror(OAP2).....56

4.1 (a-c) SEM images of different LPA4 devices. (d) Optical, SEM and AFM images of the same rope device. (e) AFM picture of a rope device and (f) SEM picture of a rope device. Scale bars: (a-c) 4um, (d-f) 9um.....59

4.2 SEM (a, b,d) images of 'mat' devices on 9um bars. (c) Optical picture of 9um bar device. (e) close up of contact area marked by red box in (a). Scale bars (a-d) 9um, (e) 2.5um.....60

4.3 Patch antenna devices showing various dimensions, with the exception of the 9um device.....61

4.4 SEM picture of a close up of the gap area of a patch antenna device. Scale bar 1um.....62

4.5 SEM pictures of two suspended SWCNT devices. Scale bars 1um.....62

4.6 I-V curves for device 4.1(c) blue curve, 4.1(d) green curve, 4.2(b) red curve, 4.4 black curve, and 4.5(b) purple curve.....63

4.7 I-V curves for device 4.1(c) before (left) and after (right) Palladium top contact.....64

4.8 I-V curves for three patch antenna devices with different gaps.....65

4.9 (a-c) IV Curves for device in figure 4.4 at T=4.2K, 65K and 135K respectively. (d-e) IV curves for device in figure 4.1(c) at T= 4.2K and 293K respectively. Blue curves are for resistance (right axes) while red curves are for current (left axes).....66

4.10 (a) I-V curves showing effect of SEM and subsequent annealing on the resistance.(a) device in figure 4.4 and b is device in figure 4.1(c).....67
(b) I-V curves showing effect of SEM and subsequent annealing on the resistance.(a) device in figure 4.4 and b is device in figure 4.1(c).....68

4.11 Beam patterns for a variety of devices in the Azimuth and Elevation directions.....69

4.12 Normalized beam pattern results for the elevation results in 4.11(b)...70

4.13 Typical beam pattern results. (a,c)elevation and (b,d) azimuth.....71

4.14 SiC globar radiation spectra with different filters taken with bolometer 2 (a,b) and bolometer 1 (c,d). (a,c) taken using 25um mylar, (b,d) taken using 6um mylar.....73

4.15 Patch antenna showing dimensions.....74

4.16 Spectra from three patch antenna devices with varying *W*.....75

4.17 Spectra from three patch antennas devices with varying *L*.....76

4.18 Spectra from three different patch antennas with varying *g*.....76

4.19 Spectra from 9*um* bar coupled devices.....77

4.20 Spectra showing bias dependency for 9um bars (a,b), patch devices (c,e,f) and a suspended device (d). (f) is from the same device as (e) but taken using 6um mylar.....79

4.21 (a)Results for output signal versus input power for a variety of devices and signal attenuation per manilla folder for bolometer 1 (b) and bolometer 2(c).....81

4.22 Bandwidth estimation illustration.....84

5.1 Antenna-coupling schemes.(top) Bowtie (bottom) Slot.....85

# CHAPTER 1

# INTRODUCTION

## 1.1 Overview

The main goal of this work has been to demonstrate a terahertz source based on SWCNTs. Using a quasi-optical coupling scheme, we have demonstrated such a source and characterized the radiated beam by looking at the radiation beam pattern and spectrum. Furthermore, we have used various imaging techniques and transport measurements to characterize the SWCNT devices.

Drawing from previous work on terahertz detection using SWCNTs [1,2] we have developed experimental techniques suited for the reverse problem of generating terahertz using SWCNTs, even though the various processes involved may be different. A big part of this project has been to develop the experimental techniques necessary to first create a device that radiates and thereafter one that radiates strongly enough to have it's spectrum measured.

Part of the motivation for this project has been the successful demonstration of radiation in the near infrared and visible spectral regions from joule heated SWCNTs [3] and MWCNT [4]. Furthermore, the prediction of terahertz radiation from Joule heated SWCNTs [5], which has not been realized experimentally. The prediction from[5] was also that the radiation spectrum would show evidence of plasmon resonances, and while the plasmon resonances have not been verified, we have demonstrated that joule heated SWCNTs can produce strong terahertz

radiation, opening up a new avenue to study interactions between radiating SWCNTs and electromagnetic structures. Importantly, we found that the radiated power is at least an order of magnitude greater than predicted for thermal Nyquist noise, hinting at the possibility of a so far unrealized non-equilibrium radiation process. With the ability to control the spectrum using integrated antennas and with room temperature operation, the SWCNT terahertz source has many potential applications.

The structure of this thesis is as follows: we begin with an introduction summarizing the state of the art terahertz sources and a brief look at some carbon nanotube basics in chapter 1. Chapter 2 looks at the background and motivation of this work and in chapter 3 we describe the experimental details. Results are then presented in chapter 4 where we demonstrate Terahertz radiation from SWCNTs. Ideas for future work are then briefly presented in chapter 5.

## 1.2 Terahertz Sources

The Terahertz region of the electromagnetic spectrum, commonly referred to as the terahertz gap, is the region between microwaves and infra red as shown in figure 1.1. It represents the intersection of classical and quantum mechanical descriptions of electromagnetic waves; one can ignore energy quantization at microwaves since the photon energy at microwaves is smaller than room temperature thermal energy, while quantization is strictly adhered to in the IR

region [6]. In terms of technology, THz is at the intersection of electronics and optics.

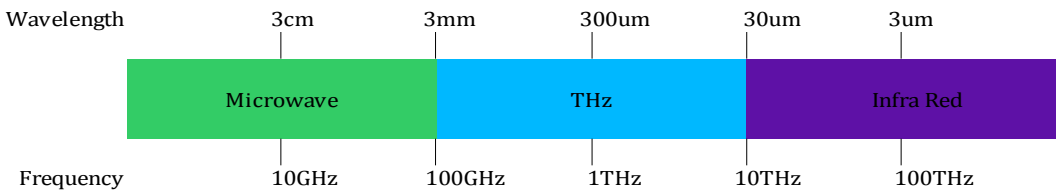


**Figure 1.1**: Electromagnetic spectrum showing the microwave, terahertz and infra red regimes

The origin of the name 'terahertz gap' lies in the fact that the terahertz region has been lacking in reliable terahertz sources and detectors and therefore underdeveloped in terms of technology. Historically, the push to develop new sources came from time domain spectroscopists and astronomers [7], where the spectroscopists sought lower frequencies while the astronomers sought higher ones.

Presently, many different types of sources exist and some of their attributes are summarized in table 1 [7]. Most of the sources are expensive, bulky or require cryogenic cooling for normal operation. There is therefore a need for cheap, compact and room temperature operating sources that can match the usability of the current systems. Figure 1.2 shows a plot of output power versus frequency for the most common type of sources used [8].

| | Optically Pumped Terahertz lasers | Time Domain Spectroscopy | Backward Wave Oscillators | Frequency Multipliers | Frequency Mixers | Quantum Cascade Lasers |
|---|---|---|---|---|---|---|
| **Average power** | >100mW | ~1uW | 10mW | uW-mW | nW | mW |
| **Usable Range** | 0.3-10 THz | ~0.1-20 THz | 0.1-1.5 THz | 0.1-1 THz | 0.3-20 Thz | 1-4 THz |
| **Tunability** | Discrete lines | Broadband | 200GHz | ~10-15% of center frequency | Continuous | |
| **CW/Pulsed** | CW or Pulsed | pulsed | CW | CW | CW | CW |
| **Turnkey systems available?** | Yes | Yes | No | Yes | Yes | No |

**Table 1.1**: Comparison of various THz sources commonly used [7].

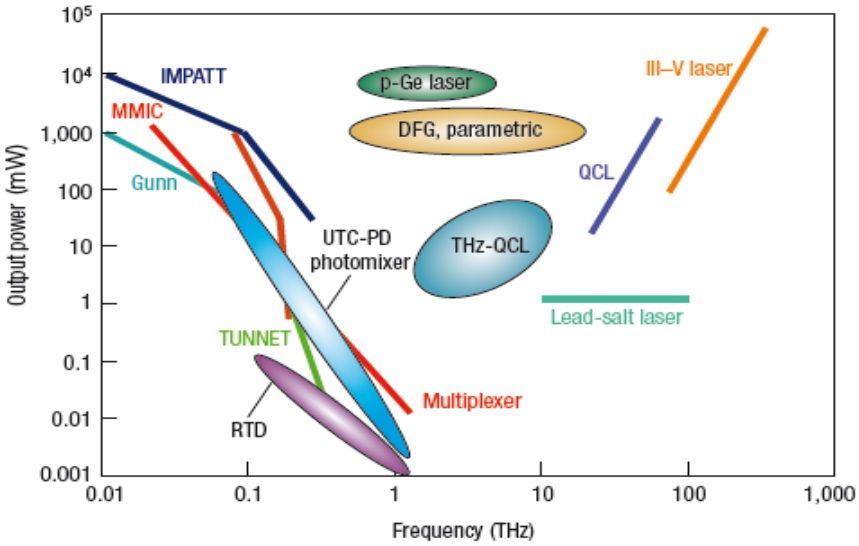


**Figure 1.2**: Power versus frequency comparisons for various terahertz sources [8].

### 1.3 Carbon Nanotube Basics

Since their discovery by S. Iijima in 1991 [9], research and technology based on Carbon nanotubes(CNTs) has grown immensely, leading many to tout them as the frontrunner for the next generation devices. Many applications have been proposed and some realized in fields ranging from optics [10], medicine [11], integrated circuits [12] among others. Propelling all the hype that surrounds CNTs, specifically the single-walled CNTs (SWCNTs), are unique properties that arise from their 1D structure . This section looks at the synthesis, structure and electrical properties of the SWCNTs.

#### 1.3.1 Synthesis

Several CNT synthesis methods have been developed that allow for production of large quantities. The main methods are briefly described below [13]:

a) *Arc discharge:* S. Iijima in his initial experiment [9] produced multi - walled CNTs using DC arc discharge. The principle is generally as follows: An arc discharge is generated between two graphite electrodes in a chamber with a partial He/Ar pressure, which causes the temperature to increase to 6000°C. At this high temperature, the Carbon in the graphite anode sublimates and during the process Carbon atoms are ejected forming a plasma. The atoms migrate towards cooler parts of the chamber, arranging themselves such that nanotubes accumulate on the

cathode. MWNTs are naturally formed, but the presence of catalysts, transition metals like Fe, Co and Ni, causes SWNTs to be produced

b) *Laser ablation:* Two methods exist depending on whether the laser is pulsed or CW. In a pulsed laser system, a Nd-YAG laser pulse sublimates a solid graphite target into an inert gas which flows through a quartz tube inside a high temperature oven. Nanotubes grow on the cooler parts of the chamber as the vapor condenses. In CW, a much lower laser light intensity is used.

c) *High Pressure Carbon monoxide (HiPCO)*: SWCNTs are grown in high pressure, high temperature flowing CO on catalytic clusters of Iron. The iron clusters serve as particles on which the SWCNTs nucleate and grow.

d) C*atalytic Chemical Vapor Deposition***:** In this process, a Carbon-containing gas like Acetylene is catalytically decomposed over a metal catalyst, leading to CNT growth.

### 1.3.2 Physical Structure

CNTs can be understood starting from the viewpoint that they are rolled up sheets of graphene. A single graphene sheet is shown in figure 1.3 then rolled up to form a closed cylinder- the CNT. Multiwalled CNTs can be envisioned as several graphene sheets rolled up concentrically.

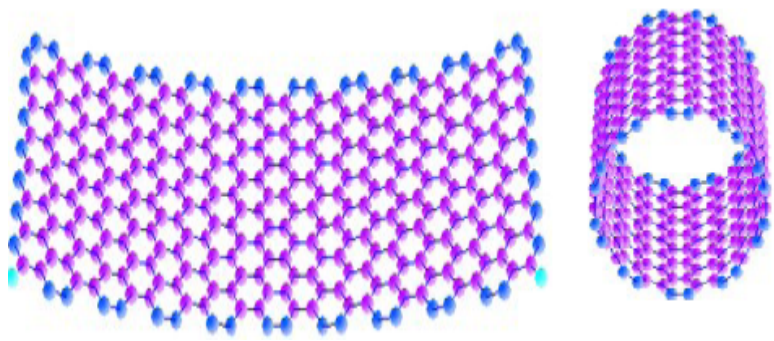

**Figure 1.3**: (left) Sheet of graphene (right) rolled up sheet to form a SWCNT [14]

Basis vectors $\mathbf{a_1}$ and $\mathbf{a_2}$ generate the graphene lattice as shown in figure 1.4 where the Carbon- Carbon bond length is 0.142nm [15]. The circumferential vector which corresponds to the side of the graphene sheet that will eventually become the CNT circumference is given by

$$\boldsymbol{C} = n\boldsymbol{a_1} + m\boldsymbol{a_2} \tag{1.1}$$

where the nanotube radius is obtained as

$$R = \frac{C}{2\pi} = \frac{\sqrt{3}}{2\pi} a \sqrt{(m^2 + mn + n^2)} \tag{1.2}$$

Three different classes of CNTs arise:

- Zigzag : m = 0 and C lies along either $a_1$ or $a_2$
- Armchair : n = m and C lies along the direction exactly between $\mathbf{a_1}$ and $\mathbf{a_2}$
- Chiral : n ≠ m

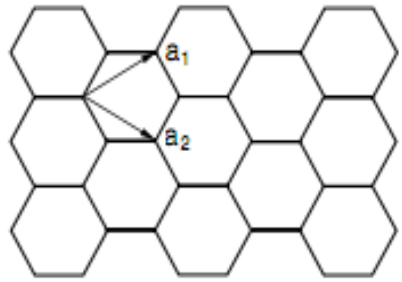


**Figure 1.4**: Graphene section showing basis vectors a1 and a2

### 1.3.3 Bandstructure

The electronic properties of CNTs arise from the geometry dictated by equations (1) and (2). CNTs are either metallic or semiconducting depending on the indices *n, m* and their diameter [16]. Metallic tubes are formed when *n-m = 3p* where p is an integer, semiconducting when *n-m = 3p +1*. Furthermore, they are *zigzag* type when p is not 0 and *armchair* type when p is 0. Periodic boundary conditions are imposed in the circumferential direction ***C***, requiring the quantization of the wavevector *k* to satisfy the condition in equation (1.3).

$$k.\boldsymbol{C} = k_x C + k_y C + k_z C \qquad (1.3)$$

Band structure calculated from the plane wave method [17] and the resulting density of states are shown in figure 1.5 for various indices. We see sharp peaks in the DOS known as the van Hove Singularities (VHS), a characteristic of 1D structures [18].

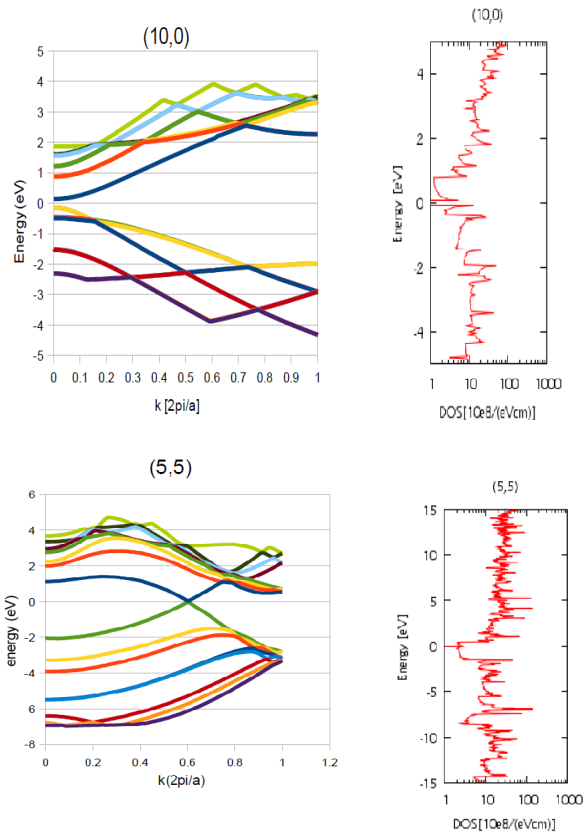


**Figure 1.5**: Band structure diagrams (left plots) and the resulting density of states (right plots) for a (10,0) and (5,5) SWCNTs.

In principle, metallic tubes have no band gaps while semiconducting ones do. In reality however, this dichotomy is disrupted by curvature effects [19]. In terms of band gaps three types of SWCNTs exist: metallic (armchair) tubes which remain purely metallic as a result of their symmetry, quasi-metallic (zigzag) tubes which are ideally metallic tubes but have small band gaps in their bandstructure, shown in figure 1.6(a) and Semiconducting (chiral) tubes which always have band gaps. Apart from the purely metallic tubes, the rest have bands that are modulated by the radius as shown in figure 1.6 (b)

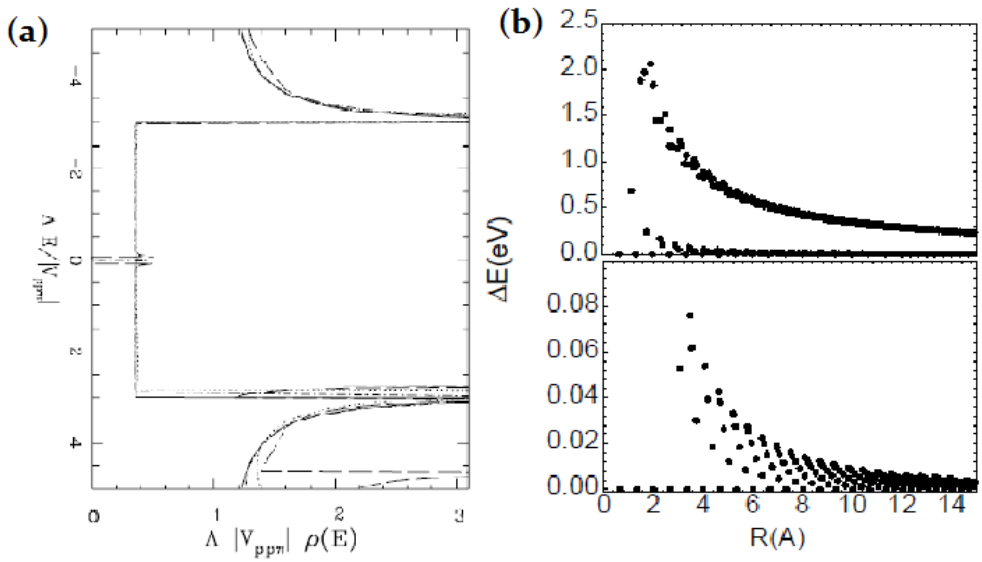


**Figure 1.6(a)** DOS diagram showing a small band gap near zero [19] **(b)**(top panel)band gap dependence on radius- top curves are semiconducting SWCNTs, middle curves are quasi-metallic SWCNTs and bottom curves are metallic SWCNTs. (bottom panel) close up of top [16].

### 1.3.4 Electronic transport

Transport in CNTs is described starting with the Landauer formalism [20], which establishes conductance as a transmission coefficient through a carbon nanotube. Considering two metal contacts separated by a CNT as shown in figure 1.7, the problem consists of understanding the movement of electrons from one contact to the other.

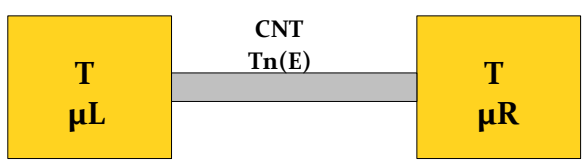


**Figure 1.7**: Illustration of a SWCNT bridging two metal contacts

The two metal conductors are electron reservoirs in thermodynamic equilibrium at temperature $T$ and electrochemical potential $\mu_L$ and $\mu_R$. Electrons injected into the CNT are distributed over energy $E$ according to the Fermi-Dirac distribution function

$$f(E) = \frac{1}{e^{\frac{E-E_f}{kT}}+1} \tag{1.4}$$

Electrons move along the CNT with a transmission probability as a result of elastic scattering, generating a current in the CNT given by [21]

$$I = -\frac{e}{\pi\hbar}\int dE \sum_n [f_l(E)-f_r(E)]T_n(E) \tag{1.5}$$

where $f_L$ and $f_R$ are the left and right electron distribution functions, and $T_n(E)$ is the total transmission probability. Expressing the electrochemical potentials as [21]:

$$\begin{aligned} \mu_L &= -E_L+\frac{eV}{2} \\ \mu_R &= -E_R-\frac{eV}{2} \end{aligned} \tag{1.6}$$

and assuming a small applied voltage $V$, in the low temperature limit ($K_bT<<eV$) the total current becomes [21]:

$$I = -\frac{e^2}{\pi\hbar}V\sum_n T_n(E_F) = GV \tag{1.7}$$

Where $G$ is given by the Landauer formula [21]:

$$G = \frac{e^2}{\pi\hbar}\sum_n T_n(E_F) \tag{1.8}$$

$n$ is the number of modes. For a metallic CNT, due to spin degeneracy (X2 for the subbands per spin), $n$ = 4, and assuming Ohmic(perfect) contacts with the metal reservoirs, the maximum conductance that can be attained is

$$G = 4\frac{e^2}{\hbar} = \frac{1}{6.45\mathrm{K}\,\Omega} \tag{1.9}$$

**1.3.4.1 Ballistic versus Diffusive regimes**

Ballistic transport occurs when there is unrestricted motion of electrons from one reservoir to another, implying no scattering events. This implies that the conductance of the sample does not depend on the channel length, but on the availability of transport modes. Diffusive transport occurs in the event of electron scattering. The motion of the electrons is stochastic, subject to scatterers along a particular channel. The concept of the electronic *mean free path* arises and it is defined to be the average length through which an electron moves ballistically.

**1.3.4.2 Scattering Processes**

Elastic scattering has been mentioned in the Landauer formalism, however, other scattering mechanisms also occur in metallic SWCNTs. Some scattering mechanisms include [21]:

a. Impurity scattering (elastic)

b. Electron-electron scattering (elastic)

c. Acoustic phonon scattering (inelastic)

d. Optical phonon scattering (inelastic)

e. Zone boundary phonon scattering (Inelastic)

Figure 1.8 is a  illustrates how these processes may occur.

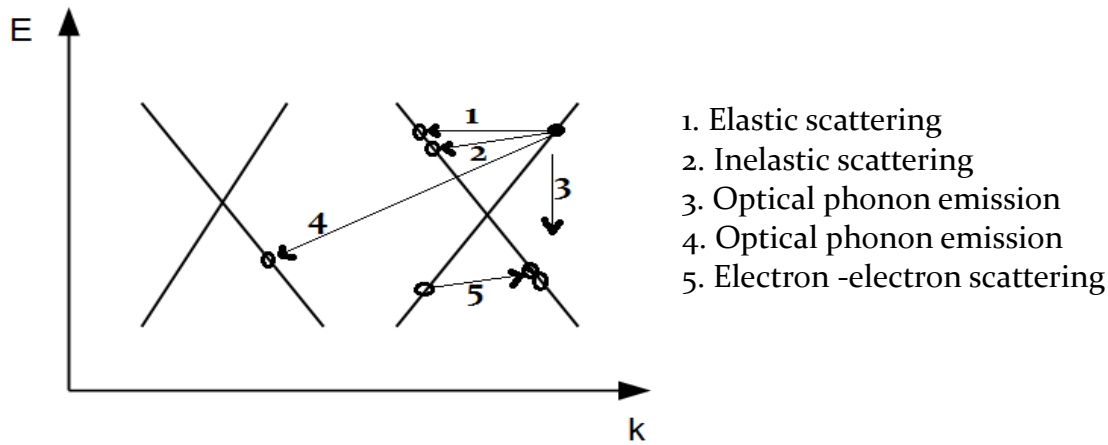


**Figure 1.8**: Energy band diagram showing various scattering processes [21]

### 1.3.4.3 Contact Resistance

In the absence of Ohmic contacts, Schottky barriers form at the metal-CNT interface. Yao *et al.* [22] performed experiments on high-field electrical transport in SWCNTs and categorized contacts  into low resistance contacts (LRC) and high resistance contacts (HRC). The two types of contacts manifest themselves differently in the I-V curves as shown in figure  1.9.

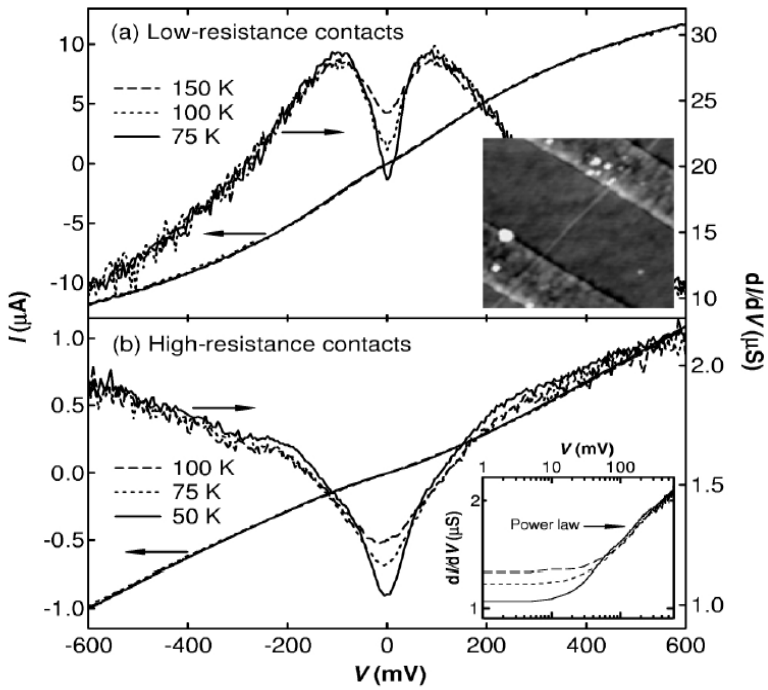


**Figure 1.9**: I-V Characteristics for (a) low resistance contacts and (b) high resistance contacts. Inset is SEM picture of the device [22]

The total resistance in the presence of imperfect contacts is therefore the sum of the ideal resistance and the contact resistance. In the scope of this work, I-V curves are used primarily to probe the transport characteristics from which we mainly infer the type of contacts, the various transport regimes (acoustic versus optical scattering) and an idea of the SWCNT configuration[1].

[1] Single tubes, ropes, films etc.

# CHAPTER 2

# BACKGROUND AND MOTIVATION

## 2.1 Blackbody Radiation

Any object with a temperature above absolute zero emits thermal radiation, and since we'll be dealing with devices emitting radiation at room temperature and above, it is instructive to at look the general properties of thermal radiation. The formula describing the blackbody emission spectrum was discovered by Planck in 1900 while investigating the spectral distribution of the light emitted by heated objects [23]. In this context, a blackbody is defined as a cavity in which the electromagnetic modes are in thermodynamic equilibrium with the cavity walls at a temperature $T$ [23], where the average energy in a mode of frequency $v$ is given by the average number of photons in the mode multiplied by the energy of the photons:

$$E_v = \frac{hv}{e^{\frac{hv}{kT}} - 1} \tag{2.1}$$

Taking the mode density per unit frequency and volume as [23]:

$$\rho_m(v) = \frac{8\pi v^2}{c^3} \tag{2.2}$$

The energy density per unit frequency per unit volume in the cavity, is the product of equations (2.1) and (2.2) and, is the Planck's blackbody law:

$$\rho_{energy}(v) = \frac{8\pi h v^3}{c^3} \frac{1}{e^{\frac{hv}{kT}} - 1} \tag{2.3}$$

The power flow of thermal radiation (spectral emittance) through an area A in the cavity is obtained by integrating (2.3) over all solid angles [24], expressed in terms of wavelength (λ) and frequency (v) [23] respectively as:

$$\frac{d}{d\lambda} S(\lambda, T) = \frac{2\pi hc^2}{\lambda^5} \left( \frac{1}{e^{\frac{hc}{\lambda kT}} - 1} \right) \tag{2.4}$$

$$dS(v, T) = \frac{2\pi h}{c^2} \frac{v^3 dv}{e^{\frac{hv}{kT}} - 1} \tag{2.5}$$

Two limiting cases are [23];

1) *Short wavelength limit*: hc/λ >> kT , in which case (2.4) becomes:

$$\frac{d}{d\lambda} S(\lambda, T) \approx \frac{2\pi hc^2}{\lambda^5} e^{\frac{hc}{\lambda kT}} - 1 \tag{2.6}$$

2) *Long wavelength limit:* hc/λ << kT, in which case (2.4) becomes:

$$\frac{d}{d\lambda} S(\lambda, T) \approx 2\pi ckT\lambda^{-4} \tag{2.7}$$

It is often convenient to use the long wavelength limit in the infrared to millimeter wave region [24]. Figure 2.1 shows a plot of the spectral emittance in [$Wm^{-2}um^{-1}$] for a blackbody at several different temperatures. Of relevance to this work is the featureless spectrum which is a characteristic of blackbody radiation. Furthermore, since we will be operating our devices at room temperature, it will be

important to filter out the 10*um* (30THz) room temperature peak. This is accomplished by using a detector equipped with low pass filters, since our anticipated region of interest is up to around 10 THz.

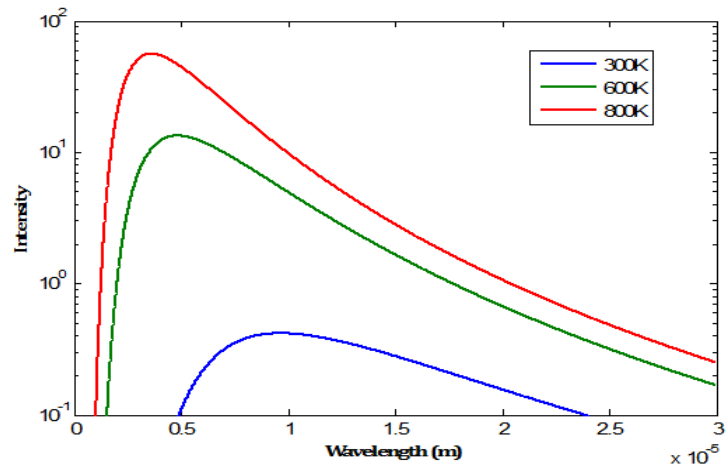


**Figure 2.1**: Blackbody emission spectrum at various temperatures

## 2.2 Light Emission from Single Walled Carbon Nanotubes

Light emission has been observed from electrically heated SWCNTs, with wavelength specific peaks that correspond to band gap transitions in the *van Hove singularities* [25, 26], in contrast to the featureless black body radiation spectrum. The observed spectrum is in the near IR regime and is attributed to Joule heating of the SWCNTs [25]. The light emission spectrum owing to band gap transitions can be calculated using [25]:

$$S(E) = \frac{1}{\tau(e)} D_J(E) f_o(E_C(k) - F_C) \cdot (1 - f_o(E_V(k) - F_V)) \qquad (2.8)$$

Where $E$ is the emitted photon energy $D_j(E)$ is the joint density of states $f_0(E)$ is the Fermi Dirac distribution and $1/\tau(E)$ is the emission rate, which comes from the photon transition rate given by the Fermi Golden Rule [27] as shown below:

$$\frac{1}{\tau_{(nk)}} = \frac{2\pi}{\hbar}\sum_{k'}|\langle n'k'|H|nk\rangle|^2\,\delta[E_n(k)-E_n'(k)+\hbar\omega] \tag{2.9}$$

Figure 2.2 shows the calculated emission spectrum from a semiconducting (4,0) SWCNT at two different temperatures: 3000K - Green curve, 1200K – Blue curve.

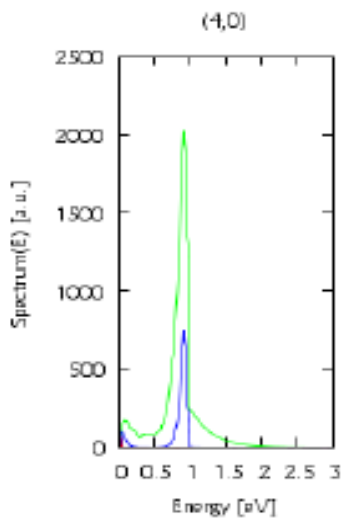


**Figure 2.2**: Emission spectrum for a (4,0) SWCNT.

In the experiment performed by Mann *et al.* [25], light emission is observed from an electrically biased individual SWCNT. They determined the tubes to be quasi-metallic due to a negligible gate effect on the current. Light emission is attributed to Joule heating of the SWCNT where the applied electric field causes a

high electronic temperature which increases the distribution of electron and holes as described by the Fermi Dirac distribution. These carriers then radiatively recombine producing light with peaks that correspond to first and second *van Hove singularities* as shown in figure 2.3(left).

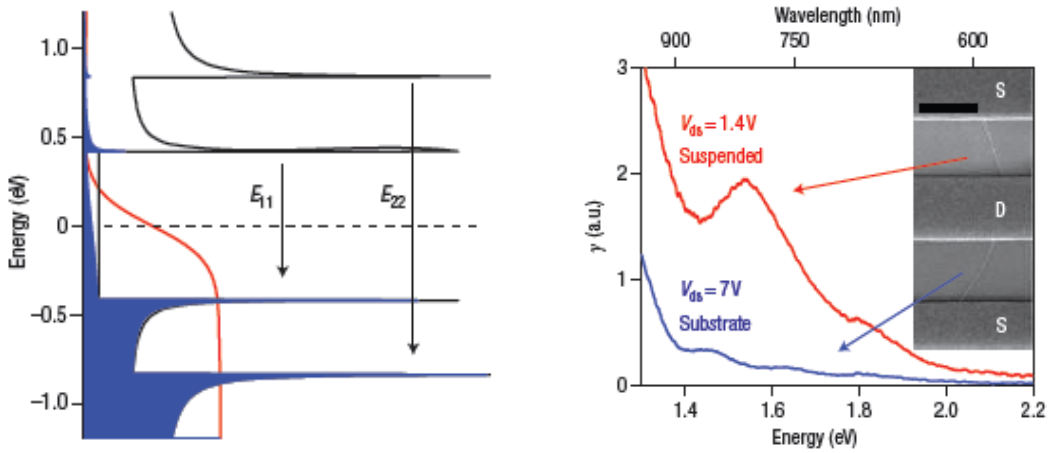


**Figure 2.3**: **(a)** DOS diagram illustrating the thermal light emission. The curve on the blue region corresponds to the electron population at various energies calculated by multiplying the DOS (black line) and the Fermi-Dirac distribution function (red line) at 1200K. $E_{11}$ and $E_{22}$ are the energies associated with first and second VHS respectively. **(b)** The emission spectra for the supported and suspended parts of the tube. Inset shows the SEM picture of the device [25].

Comparison of the light emitted from the suspended section of the tube with that of the supported section supports the Joule heating model; As shown in figure 2.3(b), the peak near 1.6eV is more pronounced in the suspended section even though the supported section receives a greater electrical bias. This implies that the suspended tube is able to sustain a high electronic temperature and therefore a greater electronic distribution in the VHS than in the supported part of the tube, which in comparison loses heat to the substrate faster. Their experiments span the near-IR and the visible regime. By changing the source drain-voltage, they were able to tune the peaks in both regimes, though not predictably. Quantum effects

like phonon assisted transitions, transitions from defect states in the long tubes and inter-band transitions were proposed as possible reasons for the inexplicable peaks. Figure 2.4 shows the emission spectra in the near- IR (a) and in the visible (b).

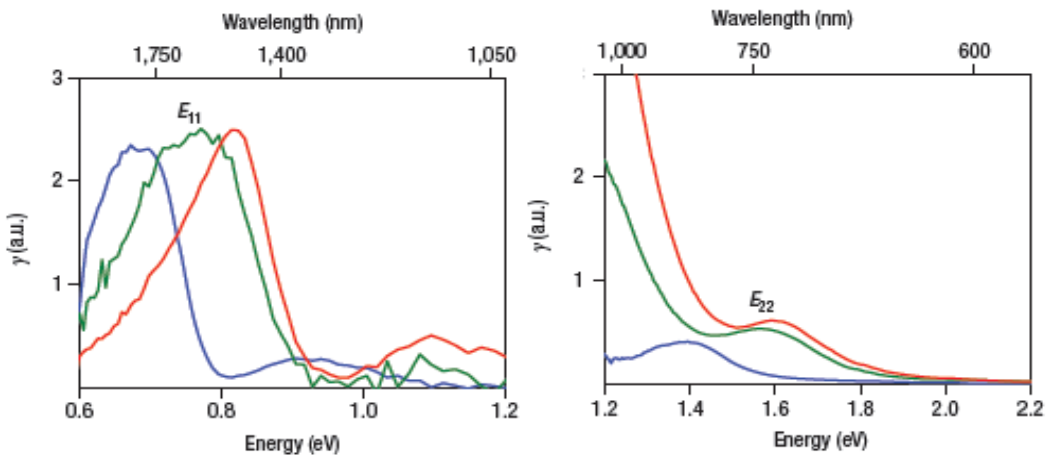


**Figure 2.4: (a)** Light emission spectra in the infrared for three 2um long QM-SWNTs (red,green and blue) at a gate voltage of -20V and biased at V = 1.4, 1.1, 1.3V respectively. **(b)** Corresponding emission spectra for the three tubes in the visible range. V=1.5, 1.3,1.5 respectively [25].

Xie *et al.* [26] have performed the same experiment, where a SWCNT is electrically driven to emit light. As shown in figure 2.5 they also investigate emission from supported and suspended sections of the same SWCNT.

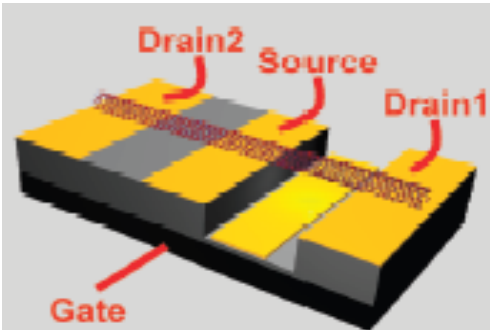


**Figure 2.5:** Illustration of SWCNT device with supported and suspended sections [26].

In the emission spectrum for the supported tube section, figure 2.6(a), an extra smaller peak is observed and attributed to a phonon assisted transition [26] because the energy difference between the two peaks (0.17 eV) is close to the 0.2eV and 0.16eV optical phonon energies. Figure 2.6(b) shows a depiction of phonon assisted emission.

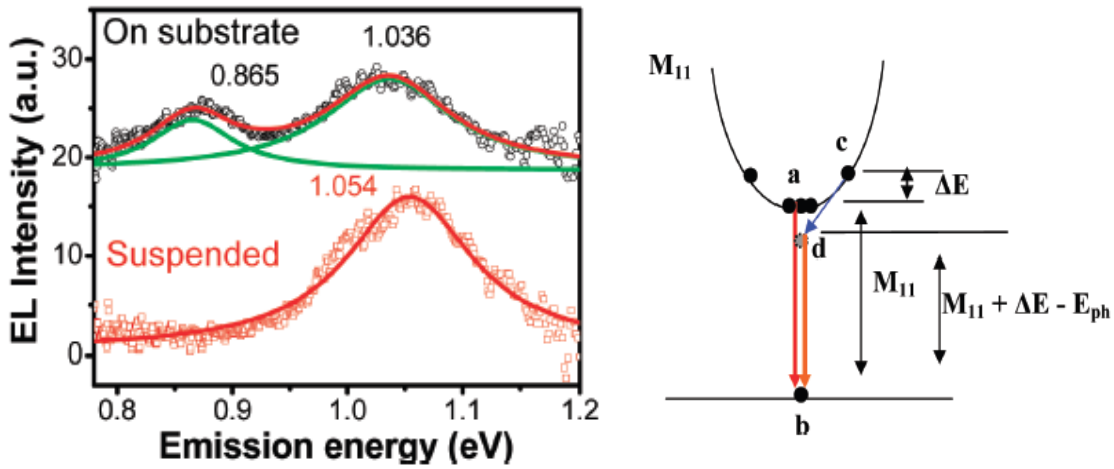


**Figure 2.6: (a)** Emisson spectrum of suspended (lower curve) and supported (upper curve)sections of the same tube. Redlines represent Lorentzian fits to the results and the green lines are fits to the individual peaks. **(b)** Illustration showing various emission processes- direct $M_{11}$(a-b), phonon assisted (c-d-b) Black dots denote excitons. The phonon-assisted emission energy is $M_{11} + \Delta E - E_{ph}$, where $M_{11}$ is the lowest excitonic transition energy for metallic SWCNTs, $\Delta E$ is the average energy difference between the excitons at "c" and the excitons at "a", and $E_{ph}$ is the phonon energy [26].

All emission experiments on SWCNTs so far have resulted in observation of spectra in the infrared to visible. While there is theory [28] predicting THz emission from SWCNTs, no experimental results have been published or reported. In the band gap transition model described by (2.8), there is no explicit rule that limits transitions to semi- conducting bands, and it presumably extends to transitions due to small-band gaps. It is therefore foreseeable that THz radiation will be emitted if such

transitions were to occur. In the following section absorption measurements on SWCNTs are shown, where the *SBG model* of SWCNT- THz interaction is invoked to explain a THz peak.

### 2.3. Carbon Nanotubes and Terahertz

SWCNTs have mainly been considered for use in optoelectronic devices, propelled mainly by a lot of research in semi-conducting SWCNTs. In this section, THz experiments with metallic SWCNTs are discussed as part of the motivation of this project. Furthermore, some EM calculations are presented that go further than the interaction of THz and SWCNTs, like in absorption and TDS experiments, to prediction of plasmon resonances in the THz emission spectra.

#### 2.3.1 Absorption Measurements

Majority of the absorption experiments consist of transmission spectroscopy in SWCNT thin films. This approach is advantageous especially due to the availability of many sources that span a wide range of the EM spectrum, for example Mercury arc lamps (Near IR), tungsten-based filaments(Mid IR), SiC globars (Far IR) *etc.* In essence, absorption measurements are a probe of the electronic structure, specifically the density of states in SWCNTs [29].

Itkis *et al.* [29] investigate the absorbance of SWCNT thin films synthesized using the HiPCO process, laser ablation and arc discharge. Using different

synthesis methods yields SWCNTs with different diameters which is especially important because of the radial (curvature) dependence of small band gaps (and therefore radiation spectrum), as shown in figure 1.6(b). The as-prepared SWCNTs were purified to remove amorphous carbon, catalysts and other nanoparticles. Absorption spectra from the three different SWCNT films are shown in figure 2.7, where curve **a** is from SWCNTs produced by electric arc discharge, b by laser ablation and **c** from the HiPCO process. The diameters are 1.37±0.1nm, 1.22 ±0.1nm and 0.8±0.1nm respectively.

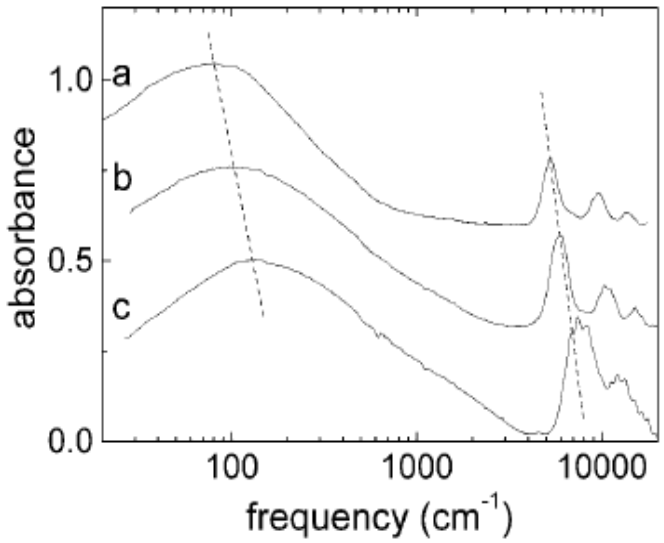


**Figure 2.7**: Absorbance spectra for purified SWCNT films. (Note 100cm$^{-1}$ = 1THz) [29].

The main features in the spectra are the peaks in the near and far IR. The near IR peaks between 4000-15000 cm$^{-1}$ are attributed to band transitions in metallic ($M_{11}$) and semiconducting ($S_{11}$, $S_{22}$) SWCNTs as shown in figure 2.8.

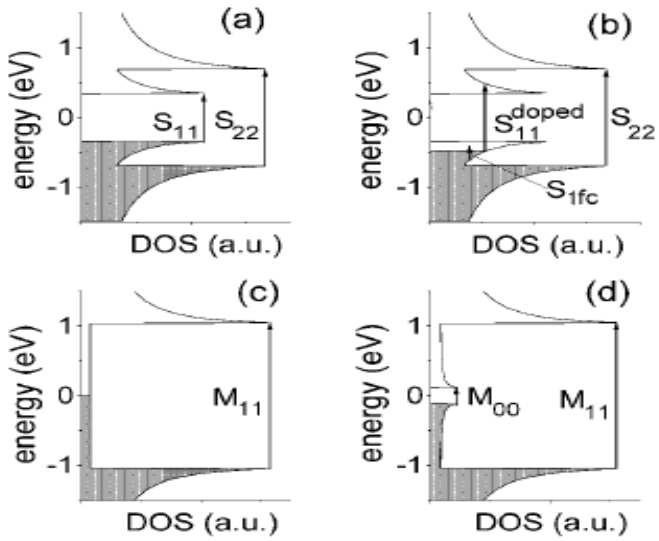


**Figure 2.8**: Illustration showing the density of states showing interband transitions from **(a)** Semiconducting SWCNT, **(b)** Hole doped semiconducting SWCNT, **(c)** Metallic SWCNT **(d)** Quasi-metallic SWCNT [29].

The far IR peaks are attributed to the small band gaps ($M_{00}$) that open up in the otherwise purely metal SWCNTs. The dotted line in figure 2.7 helps to visualize the shift in peaks as the diameter shifts from the largest (a) to the smallest (c) which supports a band gap modulated peak. A similar study by Pekker *et al.* [30] also correlates the diameter and small band gap to the observed peaks, figure 2.9.

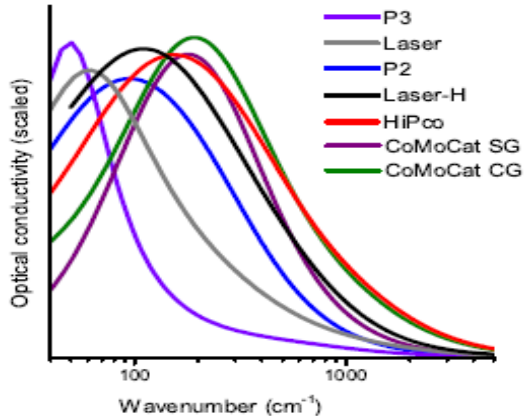


**Figure 2.9**: Optical conductivity curves from SWCNT films synthesized differently. The films have different SBG that is related to their diameter . Diameters in nm are: P3~1.43,Laser~1.25, P2~1.43,Laser-H~1.25, HiPCO~1.15,CoMoCat SG~0.8,CoMoCat CG~0.8 [30].

While Itkis *et al.* measure the absorption spectrum, another similar transmission experiment performed by Borondics *et al.* [31] derive the conductivity of the thin SWCNT samples over a similar frequency range. The conductivity is estimated for the films between 50K and 300K temperatures. While they experiment on various SWCNT (laser ablated) films investigating doping effects, of interest here is the Terahertz conductivity peak (TCP) and the temperature dependence. Figure 2.10 shows the conductivity of one of their samples at different temperatures.

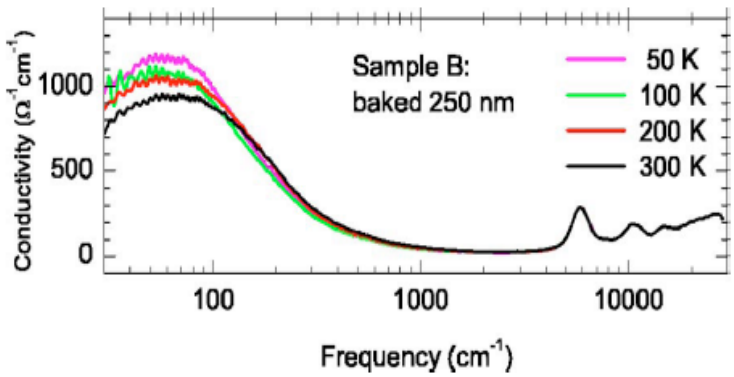


**Figure 2.10**: optical conductivity curves for SWCNT film sample at various temperatures [31].

We see similar near and far IR peaks to those of the absorption spectrum in figure 2.7. In terms of the conductivity, the far IR peak is described by a two component model consisting of a Drude free-electron contribution and a Lorentzian peak centered near 10meV, implying that the peak is due to SBGs. The temperature dependence in the far IR peak can be interpreted as follows: since room temperature thermal energy ~25meV contributes to spontaneous transitions in small band gaps, lowering the temperature implies that more carriers will now be

involved in absorption of the incident source radiation.

It is the far IR peak, dubbed the TCP, that provides an impetus to perform the inverse emission experiment. While its origin is a contentious issue (being ascribed to either small band gaps as described or to plasmon resonances), its existent cannot be ignored. The next section looks at some TDS experiments that have also resulted in the observation of a conductivity peak in the THz region.

### 2.3.2 Terahertz Time Domain Spectroscopy Experiments

THz-TDS is a technique in spectroscopy where material properties of a sample are probed with short pulses of THz radiation [32]. In general, the pulse photoexcites the sample which then re-radiates a THz pulse due to a change in the current or polarization of the sample. This re-radiated THz pulse is analyzed to uncover the dynamics of the underlying processes [33]. In one such experiment [34] Kampfrath *et al.* probe the THz properties of SWCNT thin films synthesized through the HiPCO method. From the transmitted THz pulse through the SWCNT film, they extract the effective dielectric function $\varepsilon_{eff}(\omega)$ averaged over the length scale of the pulse wavelength. The complex part of the dielectric function is obtained from effective-medium theory [34], and the real part of the conductivity is derived as: $Re\ \sigma(\omega) = \varepsilon_o \omega\ Im\ \varepsilon(\omega)$. Figure 2.11(a) shows the complex dielectric function. The Drude model predicts a large negative real part of the dielectric constant which means that light can penetrate only to a very small extent [35]. The

imaginary part of the dielectric constant describes the dissipation of energy associated with the motion of electrons [35]. Figure 2.11(b) shows the resulting conductivity, which quantifies how strongly the sample absorbs light of frequency $\omega$ [35].

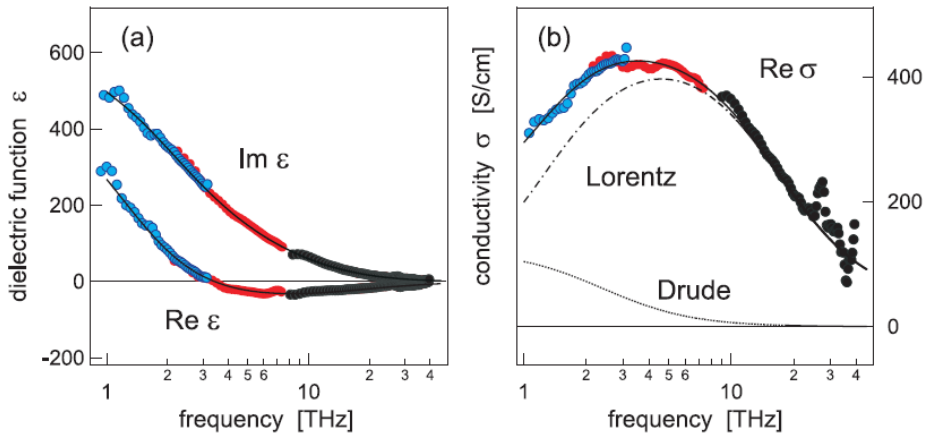


**Figure 2.11:** (a) Frequency dependence of the dielectric function and best fits to the data (solid lines) (b) Conductivity with Lorentz and Drude model fits. The blue, red and black dots denote different THz sources [34].

The best fit for the conductivity curve is from the Lorentz model, whereas the Drude model typically used for metals gives a poor fit. As in the previous interpretation, the peak is SBG mediated since the Lorentz contribution corresponds to direct band transitions in small band gaps. While all the experiments mentioned so far deal with free standing SWCNT films, there are others that have SWCNTs supported by a substrate. Seliuta *et al.* [36] perform THz-TDS experiments on $SiO_2$-CNT structures. By looking at the photoresponse, figure 2.12, they observed maxima at 1 and 4THz which they attribute to antenna resonances of SWCNTs corresponding to reduced current excitation.

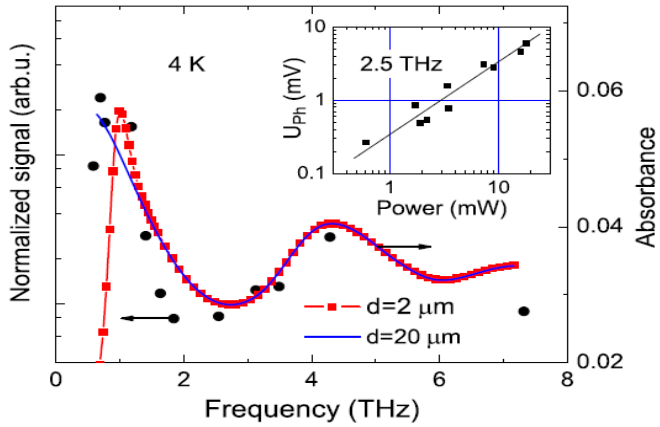


**Figure 2.12**: Dots: experimental dependence of the photoconductive component *UPh* on excitation frequency left scale. Lines: calculated absorbance of SWCNT plates of thickness *d* right scale. Inset: the experimental photoconductive component vs laser power [36].

With the antenna resonance interpretation in mind, the next section looks at some of the calculations that predict the surface waves in the SWCNTs.

### 2.3.3 Review of EM Calculations

Theoretical studies into the interaction of SWCNTs with electromagnetic waves as discussed here have been performed by Hanson [37], Nakanishi *et al.* [38] and Slepyan *et al.* [39], and are mainly motivated by the idea of a SWCNT as an optical antenna[39]. The calculations consist of numerical solutions to the Hallén integral equation[37] / Pocklington's integro-differential equation and the Leontovich – Levin equation is solved approximately analytically [39,40].

*Problem Statement:* To find the scattered electric field from a finite length SWCNT due to currents induced by an incident field.

*Approach:* An incident electric field $\mathbf{E}_z$ polarized in the direction of the tube

impinges on a SWCNT with a finite length $L$ and a radius $a$, inducing an axial current. The electron motion is characterized by a distribution function which satisfies the Boltzmann kinetic equation [37].

$$\frac{\partial f}{\partial t}+eE_z\frac{\partial f}{\partial p_z}+v_z\frac{\partial f}{\partial z} = v[f_o(\boldsymbol{p})-f(\boldsymbol{p},z,t)] \tag{2.10}$$

Where $f$ is the electron's distribution function, $v_z$ is the electron velocity, $e$ is the electron's charge, $v$ is the relaxation frequency, $p$ the 2D electron momentum and $f_o$ the equilibrium Fermi-Dirac distribution function.

Assuming the axial field to have the form of a traveling wave [37] :

$$E_z = Re[E_z^0 e^{(hz-j\omega t)}] \tag{2.11}$$

and

$$f = f_o+Re[\delta f\, e^{(hz-j\omega t)}] \tag{2.12}$$

With $\delta f$ as a small quantity to be found as (Assuming $h=0$ for local conductivity [37])

$$\delta f = j\frac{\delta f_0}{\delta p_z}\frac{E_z^0}{\omega-jv} \tag{2.13}$$

The surface axial current density is given by [37]

$$J_z = \frac{2e}{(2\pi\hbar)^2}\iint v_z f\, d^2\boldsymbol{p} \tag{2.14}$$

which when used with equation (2.13) yields [39]

$$J_z = \sigma_{zz}(h,\omega)E_z^0 \tag{2.15}$$

The axial conductivity is then given by [37, 39]:

$$\sigma_{zz}(h,\omega) = j\frac{2e^2}{(2\pi\hbar)^2}\iint \frac{\partial fo}{\partial p_z}\frac{v_z}{\omega - jv}d^2\boldsymbol{p} \tag{2.16}$$

The analytical expression for the axial conductivity is approximated for metallic SWCNTs using the appropriate dispersion relation [37, 39] and it is found to be

$$\sigma_{zz}(0,\omega) \simeq -j\frac{2e^2 v_F}{\pi^2\hbar a(\omega - jv)} \tag{2.17}$$

Where the propagation constant $h = 0$, implying local conductivity [39]. The rest of the formulation follows standard antenna procedure [41], where Hallén's integral equation is used since the SWCNT length is much larger than the radius $L>>a$ and the wavelengths of interest (THz) also much larger than the radius $\lambda>>a$. The current is related to the axial current density by $I(z) = J_z(z)2\pi a$ and Ohm's law becomes [37]:

$$\frac{I(z)}{2\pi a} = \sigma_{zz}(E_z^{\,s}(z) + E_z^{\,i}(z)) \tag{2.18}$$

where $E_z^{\,s}$ is the scattered field while $E_z^{\,i}$ is the incident field. A major result in [37] is shown in figure 2.13 for the input impedance for a 10 um long, 2.712nm diameter SWCNT together with that of two dimensional bulk approximation (TDBA) Copper tube with similar length and diameter, where the SWCNT has a resonance whereas the TDBA copper does not. The resonances are attributed to plasmons with the slowed down propagation velocity of $v_p \sim 0.02c$ [37]

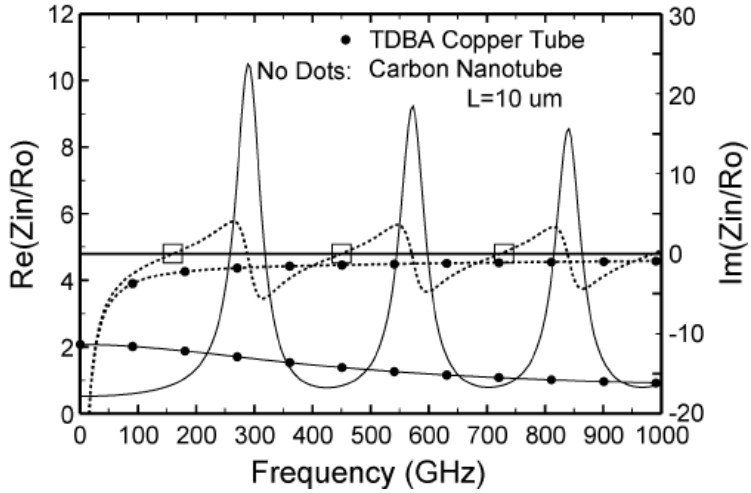


**Figure 2.13**: Input impedance for a 10um SWCNT and TDBA copper of the same length. Squares denote the resonances [37].

To find this propagation velocity, (at 160 GHz, but also applies at other resonances) the current distribution is sinusoidal, with a peak at the center of the tube with length 2L, and zero amplitude at the ends. In this case:

$\lambda_p = 4L$ , therefore, for $L = 10um$, $\lambda_p = 40um$,

For a linear dispersion relation, the plasmon velocity is

given by : $v_p = \lambda_p . f_r$

where $f_r$ is the resonant frequency, therefore,

$$v_p = 0.213c$$

where $c$ is the speed of light. This plasmon velocity can be compared to the electron Fermi velocity ($v_f = 9.7 \times 10^7$), where $v_p \sim 6.6 v_f$. Using a different approach, based on modeling a SWCNT as a transmission line Burke *et al.* [45] found that $v_p = 3v_f$.

The approximate analytical solution is found for the Leontovich - Levin equation [39, 40], and it is agrees well with the numerical solution presented in [38]. The polarizability scalar determines the electromagnetic properties of the SWCNT and is given by [40]:

$$\alpha = \frac{2\pi i R}{\omega} \int_{\frac{-L}{2}}^{\frac{L}{2}} j(z)\,dz \tag{2.19}$$

In [40], bundles of SWCNTs were also included in the calculation. A relevant result from [39, 40] is the frequency dependence of the polarizability as shown in figure 2.13. Resonances in the polarizability scalar occur at frequencies related to the SWCNT length by:

$$Re[k(\omega)]L \simeq \pi(2s-1) \tag{2.20}$$

where $k(\omega)$ is the plasmon wavenumber and $s$ is a positive integer .

The result indicates that radiation properties of the SWCNT are mainly determined by the slowed down plasmon resonances (alternatively referred to as geometric resonances) [40]. For the SWCNT lengths of interest ($L \sim 1um$), the resonances lie in the THz range where the long wavelength limit applies ($L<<\lambda$). They find the velocity of the slowed down plasmons to be ~0.02c comparable to that in [37].

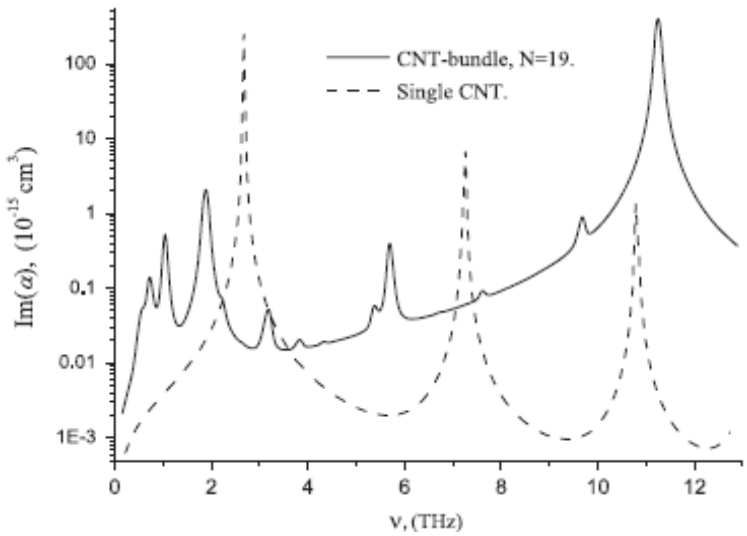


**Figure 2.14**: Frequency dependence of the imaginary part of the polarizability for an individual and a bundle of SWCNTs of 1um length [40].

Thermal radiation spectra shown in figure 2.15 also have resonances which are attributed to slowed down plasmons [40].

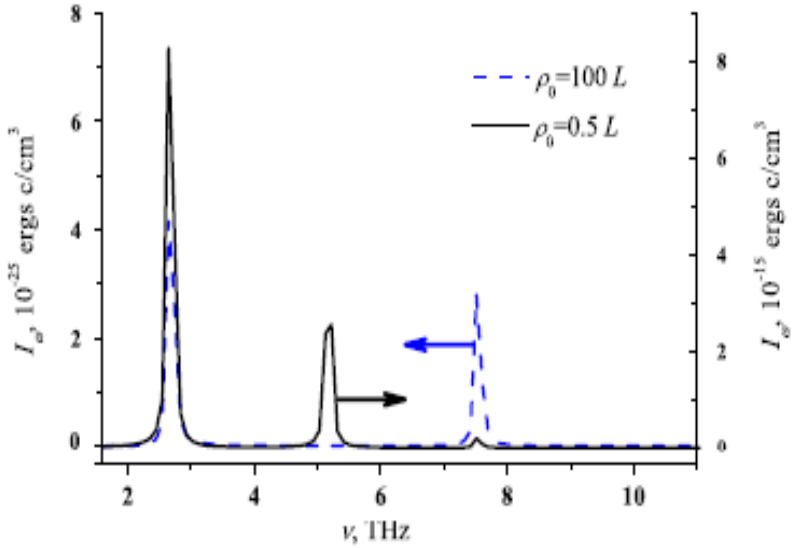


**Figure 2.15**: Thermal radiation spectra from a metallic SWCNT with L=1um, at distances of 0.5L (black solid line) and 100L (blue dotted line) [40].

#### 2.3.3.1 Terahertz Conductivity Peak

The peak in the absorption spectrum (TCP) has previously been explained using the small band gap model. A different explanation derived from the EM calculations based on polarizability is now offered. The power absorbed by a quantum system is related to the absorption cross section by [35]:

$$\sigma(\omega)=\frac{\langle P(\omega)\rangle}{I(w)}=\frac{\omega}{3}\sqrt{(\frac{\mu_o}{e_o})}\frac{Im[\alpha(\omega)]}{n(\omega)} \tag{2.21}$$

Where $\sigma(\omega)$ is the absorption cross section, $\langle P(\omega)\rangle$ is the absorbed power and $I(\omega)$ is the intensity of the incident radiation, $\alpha(\omega)$ is the polarizability and $n(\omega)$ is the refractive index.

Since the polarizability is subject to the finite-length induced plasmon resonances, and given the direct relation of the absorbed power to the polarizability, we expect to see resonances in the absorption spectrum. Broadening of the otherwise sharp resonances can be mediated by the mean-free path of the SWCNTs as shown in figure 2.16 [38] and since absorption experiments are normally performed on SWCNT thin films, where the mean free path is expected to decrease as result of disorder and impurities present in films, this works to explain the broad peak observed experimentally.

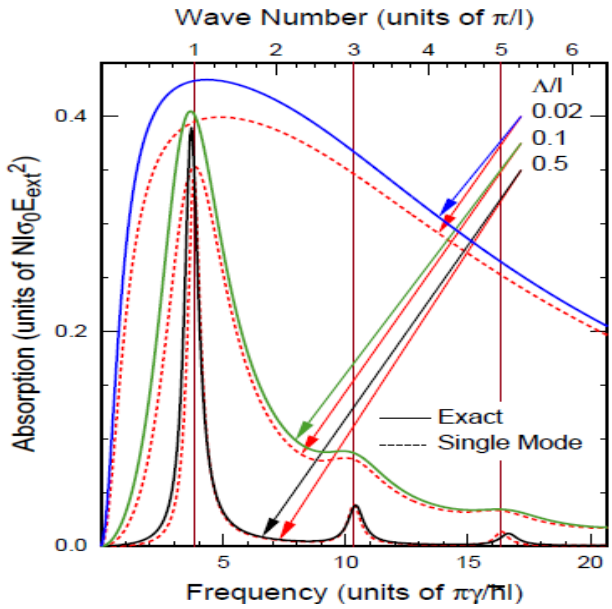


**Figure 2.16**: Absorption as a function of frequency for a SWCNT with various mean free paths as indicated. 0.5,0.1,0.02 represent clean, intermediate and dirty SWCNTs respectively [39].

### 2.3.4 Antenna and Silicon Lens Coupling

Antenna and Si lens coupling was employed previously in THz detection using SWCNTs [1,42]. In this work, we implement the same scheme for the reverse experiment, that is, THz radiation from SWCNTs. In using an antenna, we hope to couple a single mode EM single mode into space, and, as we shall see later on to tune the radiation. Used in conjunction with a Si lens, we are able to efficiently couple THz radiation to free space which in turn allows us to perform the necessary beam characterization.

#### 2.3.4.1 Single Mode Antenna Theorem

An antenna is a device that couples a single propagation mode to space [24,41]. By coupling SWCNTs to an antenna, assuming a matched impedance, the antenna will radiate all the power delivered to it thereby transforming the 3D em mode to a single mode. Using the Nyquist thermal noise formula, the single mode case is modeled as an ideal voltage source connected to resistor, representing the CNTs, in series with an antenna impedance as shown in figure 2.17. Assuming impedance matching, the total power radiated by the antenna is given by the Nyquist formula and it is simply the CNT thermal noise:

$$P = k_b BT \tag{2.22}$$

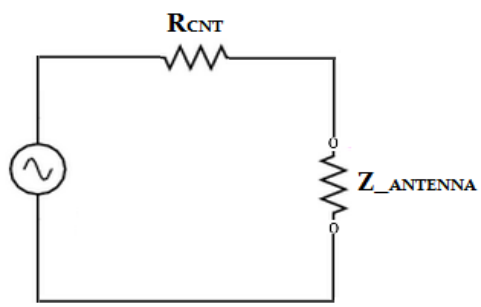


**Figure 2.17:** Circuit diagram representation of a SWCNT coupled to an antenna.

#### 2.3.4.2 Silicon Lens Coupling

Optical coupling to the device is further achieved through an elliptical Silicon lens. The tubes can either radiate directly into the silicon substrate or via an antenna. Either way, the radiation appears as a point source on the surface of the Silicon lens as shown in figure 2.18. By ray tracing, the radiation from the source

becomes a planar wave in the focal plane of the lens [45]. The far field radiation pattern is therefore determined by the diffraction limit of the cross section of the elliptical lens [46]. Due to misalignment of the radiating source, the radiation source is normally off-center relative to the lens, causing a tilted wavefront as shown in figure 2.19. Consequently, beam pattern measurements are normally offset from zero degrees in both azimuthal and elevation directions.

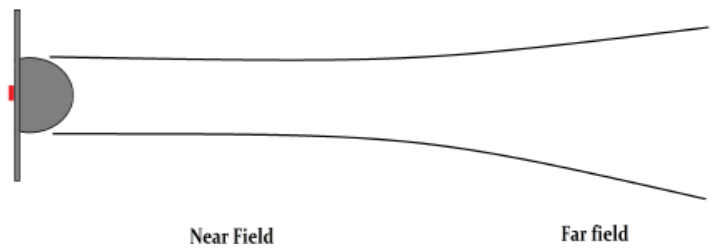


**Figure 2.18**: Illustration showing coupling to a Silicon lens. Red section indicating a point source and the resulting radiation shown by the extended lines.

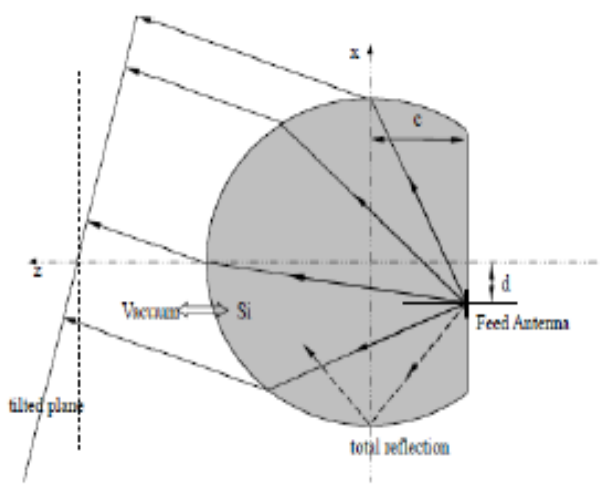


**Figure 2.19**: Schematic showing ray tracing from an off-center source and the resulting tilted wavefront [43].

# CHAPTER 3

# EXPERIMENTAL METHODS

## 3.1 Fabrication

Devices were fabricated on high resistivity Silicon wafers, which are known to have relatively high transmission in the THz range [46]. To begin with, wafers were polished [47] on both sides up to a thickness of 325um.

While the wafers were high resistivity(exact resistivity was not know), when probed directly, they presented a finite resistance (~MΩ) which hindered nanotube deposition via dielectrophoresis (DEP- section 3.2). To eliminate this effect, an SiO2 layer was deposited via Plasma Enhanced Chemical Vapor Deposition (PECVD) to a thickness between 200 – 300nm. UV lithography was then used to define electrical contacts as shown in figure 3.1,

**Figure 3.1**: Results of development after UV lithography. Purple areas indicate soon to be metalized areas. Device 1 is termed 9um Bars, 2 is LPA2 1and 3 is LPA4.

Metalization was then carried out where ~10nm of Titanium and ~200nm of gold were e-beam evaporated. After liftoff, devices were ready for dielectrophoesis (DEP), which we described in the next section. After DEP, devices were annealed in a convection oven at $200^0$ C for ~2-3 hours to reduce the contact resistance of the devices, and thereafter imaged optically, or using a scanning electron microscope (SEM) or using an atomic force microscope (AFM).

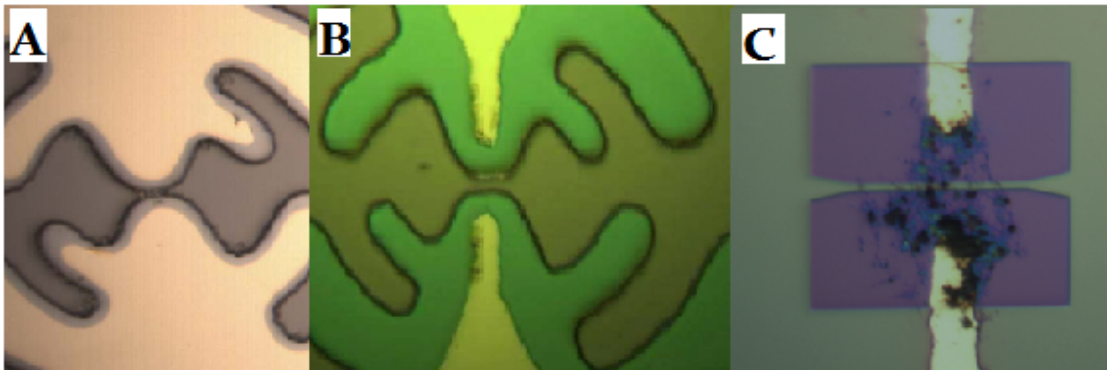


**Figure 3.2**: Optical Images showing the results of the second lithography step. (a) and (b) are log periodic antenna patterns while (c)shows a patch antenna pattern.

While devices at this stage were usable, and in some cases we proceeded with the testing, most of the devices underwent another lithographic step, where either UV lithography was used in a two step alignment process to define log-periodic antennas as shown in figure 3.2 (a) and (b), or e-beam lithography was used to define patch antennas as shown in figure 3.2 (c). Metalization for the second metal layer was done through dc-sputtering of ~50nm Palladium, which is known to create ohmic contacts with SWCNTs [60].

For some of the devices, an SiO2 passivation layer was deposited either by

PECVD or sputtering. In the case of suspended SWCNT devices, DEP was the last step. That is, after fabrication of the patch antennas, reactive ion etching (RIE) was done to remove the oxide layer, using the metalized areas of the device as the etch mask . This effectively created a trench over which SWCNTs were suspended during the DEP process. Some fabrication recipes and process parameters are included in the appendix.

### 3.2 Dielectrophoresis (DEP)

In order to incorporate SWCNTs into devices, we used DEP to deposit them across a predefined electrical gap Moreover, it is effective in separating the metallic from semiconducting tubes. For a given dispersion of particles in a solvent, DEP can be defined according to Pohl [48] as the motion of the particles relative to that of the solvent resulting from polarization forces produced by an inhomogeneous electric field. Depending on the polarizability of the particle to that of the solvent, the field strength could push the particle towards regions of high electric field (Positive DEP) or low electric field (Negative DEP) [49]. The time averaged force on a particle is given by [50]:

$$\boldsymbol{F}_{DEP} = \Gamma \epsilon_m Re\left\{K_f\right\} \nabla \left|\boldsymbol{E}^2\right| \tag{3.1}$$

where $\Gamma$ is a factor depending on geometry, $\varepsilon_m$ is the real part of the permittivity of the suspending medium and E is the electric field. The factor $K_f$ depends on the complex permittivity of both the particle $\boldsymbol{\varepsilon}_p$ and the medium.

For SWCNTs, owing to the fact that semiconducting SWCNTs have a permittivity ~2.5$\varepsilon_o$ [50] and a predicted permittivity of infinity [51] for metallic SWCNTs, the real part of the factor $K_f$ varies as follows in the low and high frequency limits:

$$Re\,K_f = \begin{cases} \dfrac{\sigma_p - \sigma_m}{\sigma_m}, & \omega \to 0 \\ \dfrac{\epsilon_p - \epsilon_m}{\epsilon_m}, & \omega \to \infty \end{cases} \tag{3.2}$$

This means that semiconducting SWCNTs experience a negative DEP force compared to metallic tubes at high frequencies. In the course of this work frequencies in the range of 5-50 MHz have been used successfully. Together with the *ac* field, a small *dc* voltage ~1V was applied via a *bias tee* for the purpose of monitoring the real time resistance across the electrodes, which changed as SWCNTs bridge the gap. Figure 3.3 illustrates the setup.

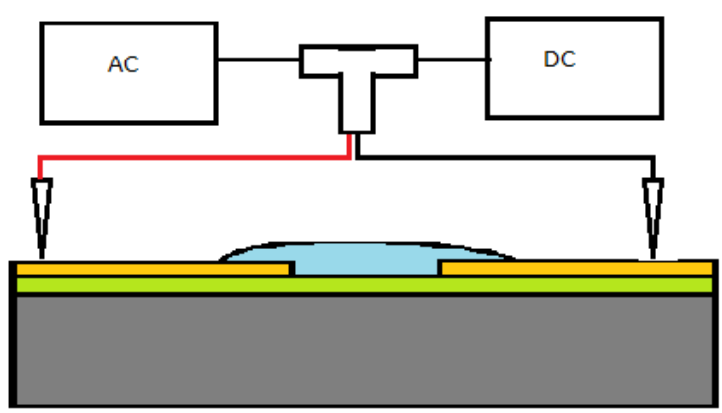


**Figure 3.3**: DEP set-up

Moreover, changing the amplitude of the applied field affected the number and length of tubes that bridge the gap as will be shown in chapter 4. Nominal values between 2-8$V_{pp}$ were used. SWCNTs used in this work were purchased from Brewer Science [52] and are in a de-ionized water (DI) based solution. Prior to DEP, the solution was further diluted in DI water, with concentrations ranging from 1$\mu$l to 1ml of CNTRENE 100 in 20ml of DI water. After the dilution, the resulting solution was ultrasonicated which helped in SWCNT dispersion. A drop of the dispersion was then applied between the electrodes as the resistance was monitored through a LabVIEW program. The process was stopped as soon as the desired resistance is achieved, by turning off the *ac* field and blowing off the drop using a Nitrogen stream. Figure 3.4 shows the real-time current change from the onset of the DEP process to the end of it.

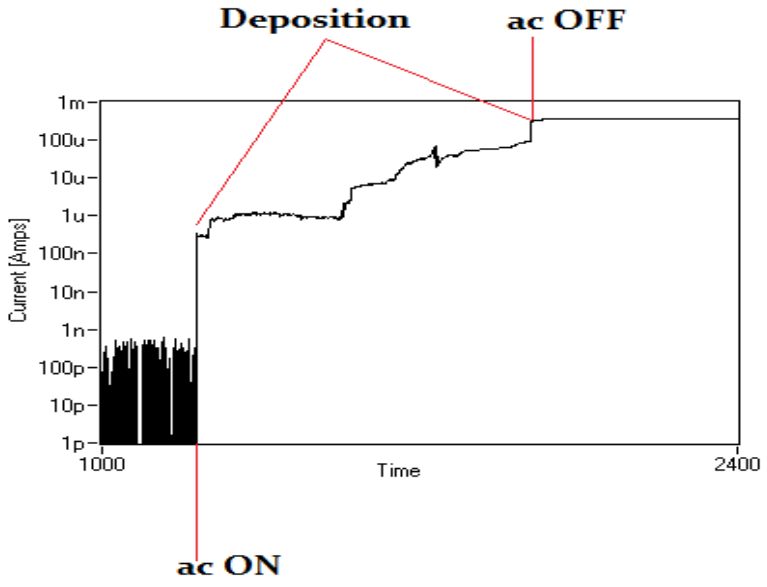


**Figure 3.4**: Current versus time curve during the DEP process

### 3.3 Transport Measurements

The current – voltage (I-V) characteristic curves were measured using a two probe measurement set-up, where a source measuring unit (SMU) was used to apply a voltage while at the same time measuring the current flowing through the sample. The equipment used were the Keithley 2400/2602/4200SCS SMUs, and were controlled via a LabVIEW program. Low temperature measurements were done using a dipstick where devices were connected to an SMA connected block, as in figure 3.5, using indium foil. Attached to the block was a temperature sensor.

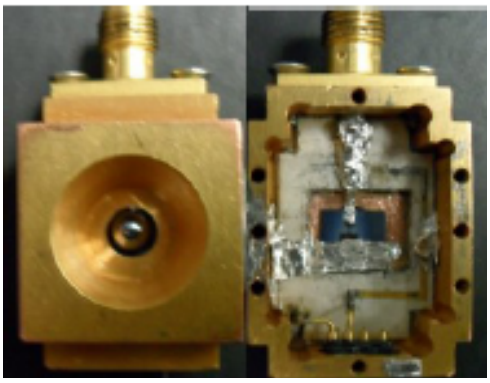

**Figure 3.5**: SMA connected block showing mounted device

### 3.4 Terahertz Detectors

The THz detectors used were the HDL-5 model from Infra-red Laboratories [54]. They are liquid helium cooled Si bolometers, equipped with low pass filters that enable measurement of THz radiation at various frequency ranges: Bolometer 1 has filters at 27um(11.1 THz), 103 um (2.91 THz) and 285um(1.053 THz) and Bolometer 2 (Courtesy of Vermont Photonics) has filters at 12.5um(25 THz), 27um and 100um(3THz). The transmission curves for the relevant filters are shown in the

appendix.

A noise equivalent power (NEP) of $\sim 10^{-13} W/Hz^{0.5}$ enabled detection of the relatively low power radiated by the carbon nanotubes. The Si bolometer is connected to a preamplifier box which provided gain at X200 or X 1000. The dewar also features a Winston cone which is used to [55]: 1) To concentrate the radiation onto the detector, 2) Restrict the field of view of the detector and 3) Distribute the incoming energy uniformly across the detector. Figure 3.6 is a cross-section illustration of the dewar showing the essential parts and THz radiation incident on the dewar window.

In a typical measurement, radiation impinges on the HDPE dewar window, passing through a particular low pass filter and is collected by the Winston cone which then feeds the Si bolometer. There is a first stage amplification inside the dewar and the output of which is then connected to a second amplification stage outside. The output signal can then be connected to a lock-in amplifier or an oscilloscope where it is recorded or visualized respectively.

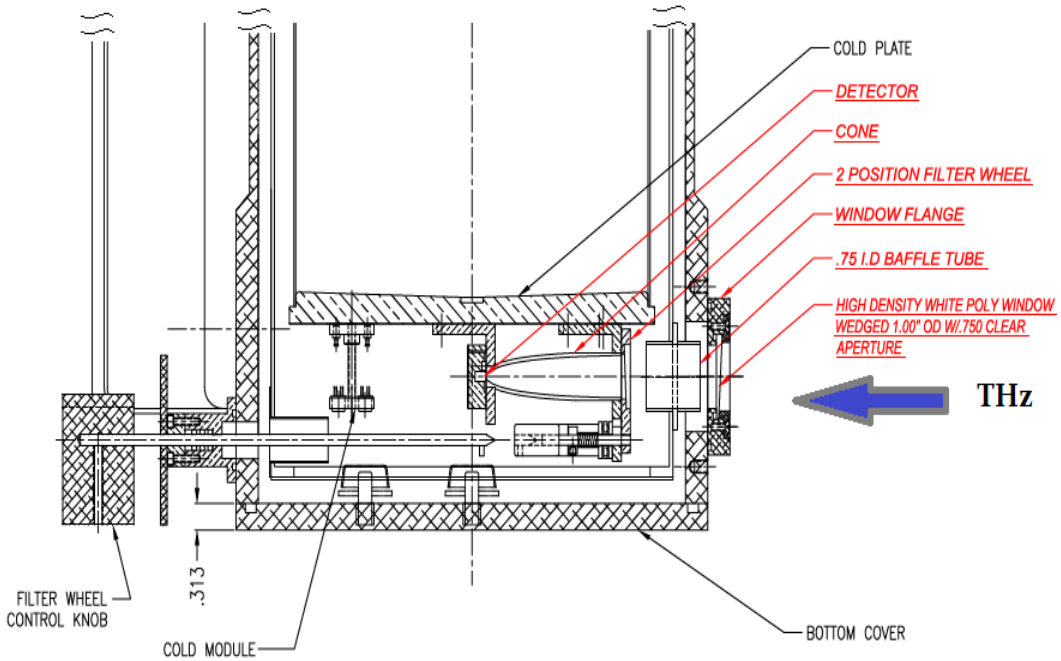


**Figure 3.6**: Illustration showing the cross section of the dewar [54].

### 3.5 Power Calibration

While the output of the detector is directly related to the radiation power, there is no direct measurement available for power radiated by the SWCNTs sources. To estimate the power from the devices we therefore employed the following calibration procedure: We begun by measuring the power from a far-IR THz gas laser using a laser power meter (Scientech Astral AA30), which gave the absolute power in $mW$. Thereafter, we detected the signal from the same gas laser using the Si bolometer detector. Normally the far-IR laser had too much power and therefore saturated the bolometer. To attenuate the laser power, we placed manilla folders at the bolometer window, gradually increasing them until the bolometer was no longer saturated. Finally, we re-measured the laser power using the laser power

meter, to confirm the previous power measurement .We then found the attenuation factor A (for when the bolometer is no longer saturated *i.e.* from the $n^{th}$ folder) as,

$$A = \left(\frac{Signal\ at\ n^{th}\ folder}{Signal\ at\ the\ last\ folder\ (n+x)}\right)^{\frac{1}{x}} \tag{3.3}$$

and the used it to calibrate the power as:

$$SWCNT\ device\ Power\left(\frac{W}{V}\right) = \frac{Laser\ power\,[mW]}{A} \times \frac{1}{Signal\ at\ last\ folder\,[mV]} \tag{3.4}$$

where *x* was the total number of folders used. We calibrated using laser lines at 184um (1.63THz), and since the bolometer's responsivity in the THz range is independent of frequency, we conclude that we get an estimate of the total power radiated by the SWCNT source.

### 3.6 Beam Pattern Measurements

Beam pattern measurements established the angular dependence of the THz signal strength . To facilitate this measurement, the block in figure 3.5 was mounted on a 2D stage that enabled translation in the azimuth and elevation directions as shown in figure 3.7. Measurements were taken every $0.5^{o}$ which provided an acceptable resolution.

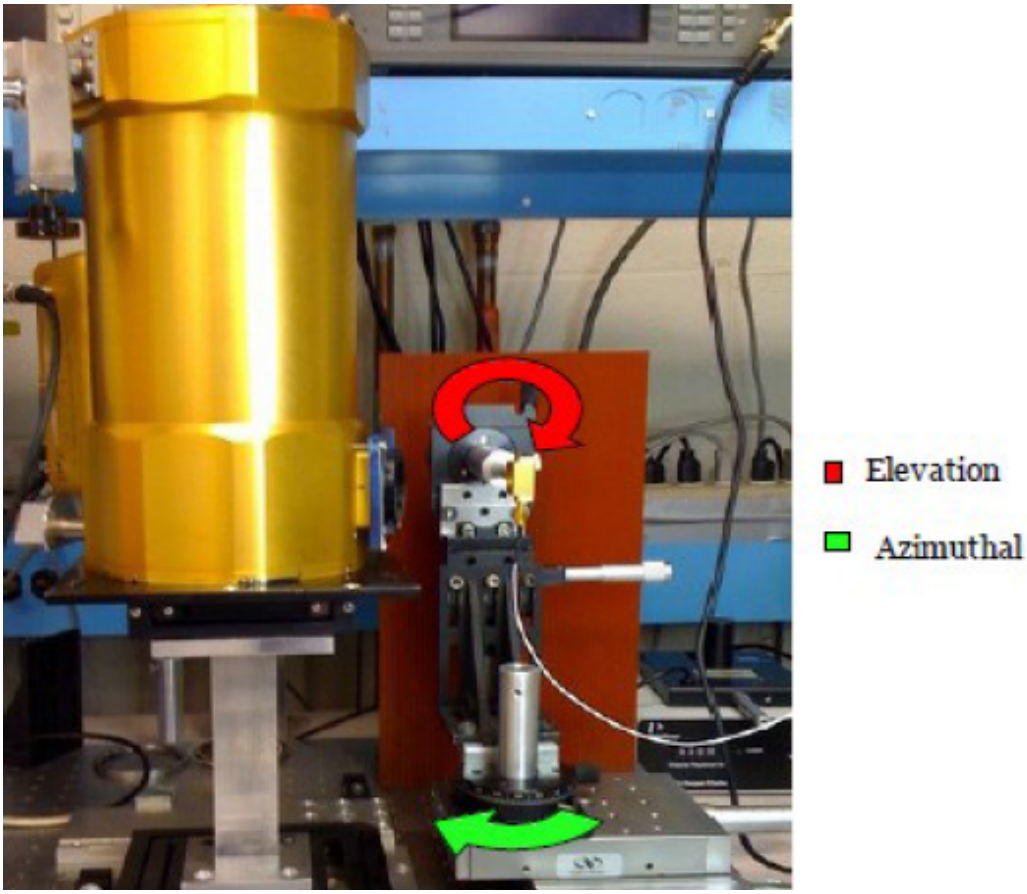


**Figure 3.7**: Picture showing the beam pattern measurement set-up.

### 3.7 Fourier Transform Spectrometer (FTS)

An FTS is an instrument used to measure the spectrum of a radiating source by modulating the radiation through interference in the time domain, then Fourier transforming the signal to reveal the spectrum [56]. Preliminary measurements on a commercial FTIR (Bruker IFS66v) at the UMass Lowell STL indicated that the SWCNT source did not have enough detectable power through the instrument. This motivated us to construct our own interferometer. This section describes the working of an FTS and the specifics of the system as we built it.

### 3.7.1 Basic Operation

The FTS is based on a Michelson interferometer, whose basic components include a movable and fixed mirror, a beam splitter, a source and a detector as shown in figure 3.8. An ideal beam splitter transmits half of the incident radiation and reflects the other half.

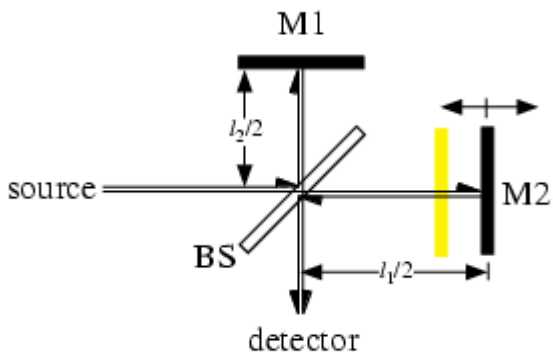


**Figure 3.8**: Illustration of the Fourier transform spectrometer [58].

Radiation from the source is incident on the beam splitter where it is separated into two equal beams. One beam goes to the movable mirror while the other goes to the fixed mirror. The beams are reflected by the two mirrors back towards the beam splitter where they recombine to form a beam which is then transmitted to the detector and the source in two equal proportions. The signal that reaches the detector is a function of the optical path difference (OPD), the difference between the fixed mirror length  and movable mirror length . The effect of translating the movable mirror is to a create a phase difference between the two beams [56]. The zero path difference (ZPD) is defined to be the point at which the OPD is zero, that

is, the two mirrors are equal distances from the beam splitter. At the ZPD, all wavelengths are in phase.

The *interferogram* is the signal acquired by the system. As the movable mirror is translated, an interference pattern is formed as the two phase shifted beams combine (interfere). The interference pattern is then detected and recorded. For a single frequency source, the interferogram is a sinusoid while that of a broadband source is a signal dominated by a centerburst that decays with increasing retardation from the ZPD. Having the ZPD as the reference, as the mirror moves on both sides of the ZPD, the interferogram created is two sided and symmetric. Figure 3.9 (a) shows the interferogram from a SiC broadband source.

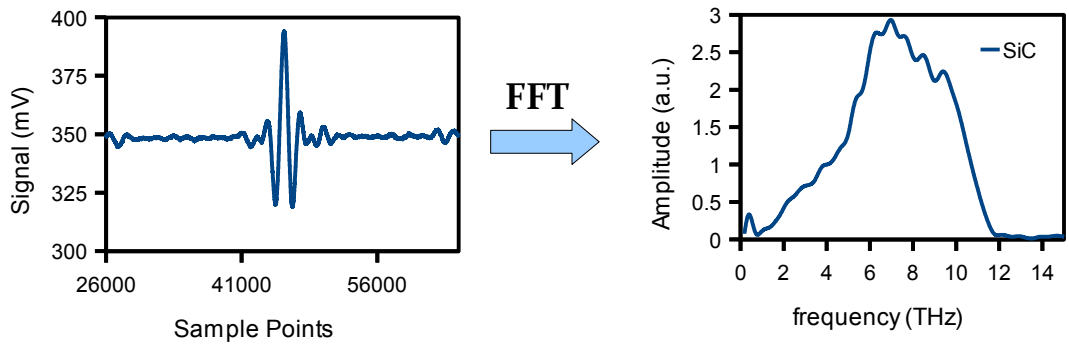


**Figure 3.9:** (left) Interferogram from a SiC source, with the resulting spectrum (right).

Once the interferogram has been acquired, the next step is to get the spectrum, which is done by performing the Fourier transform.

### 3.7.2 Interferogram Fourier Transform

Beam intensities for a monochromatic source are shown in figure 3.10, offset for clarity.

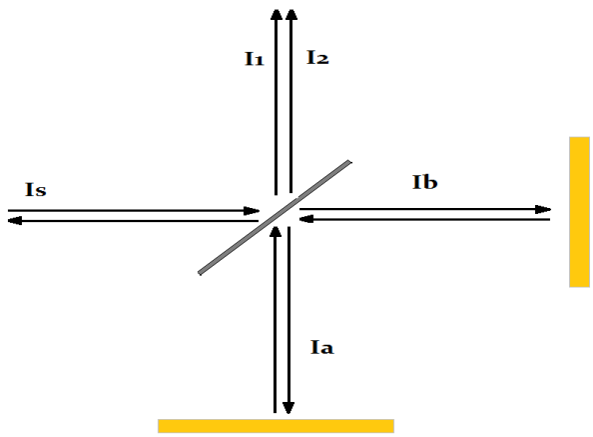


**Figure 3.10**: Beam intensities at various sections of the interferometer.

The detected light intensity is given by the interference function [56]:

$$I = I_1 + I_2 + 2\sqrt{(I_1 I_2)}\cos(\Phi_2 - \Phi_1) \tag{3.4}$$

where $I_1$ and $I_2$ are the intensities and $\phi_1$ and $\phi_2$ are the phases. The interference function is rearranged to[11] :

$$I = (I_1 + I_2)[1 + \frac{2\sqrt{(I_1 I_2)}}{I_1 + I_2}\cos\delta] \tag{3.5}$$

where the relative phase between the two interfering waves $I_a$ and $I_b$ is given by [56]:

$$\delta = 2\pi\frac{OPD}{\lambda} = \frac{4\pi x}{\lambda} \tag{3.6}$$

Assuming ideal optics and beam splitter

$$I_a = I_b = 0.5\mathrm{I}_s$$

$$I_1 = 0.5\mathrm{I}_a \tag{3.7}$$

$$I_2 = 0.5\mathrm{I}_b$$

The interference function given by equation (3.4) becomes [56]:

$$I(x) = 0.5\mathrm{I}_s[1 + \cos(\frac{4\pi x}{\lambda})] \tag{3.8}$$

Of interest is the modulated part of the signal that varies with *x*:

$$I(x) = 0.5\mathrm{I}_s[\cos(\frac{4\pi x}{\lambda})] \tag{3.9}$$

For broadband signals , the spectrum can be synthesized by a superposition of monochromatic sources which are best represented by sinusoidal waves as [56]:

$$f(x) = C_o + C_1 \cos(\frac{2\pi}{\lambda_1} x) + C_2 \cos(\frac{2\pi}{\lambda_2} x) + \ldots, \tag{3.10}$$

where the *C*s are constants.

The interferogram for broadband sources is therefore the summation of such individual monochromatic interference functions given by [56]:

$$I(x) = \sum_{\lambda_{min}}^{\lambda_{max}} C(\lambda) \cos(\frac{4\pi}{\lambda} x) \tag{3.11}$$

Where C(λ) represents the spectral distribution recorded by the detector.

To retrieve the spectral information, the complex Fourier transform is evaluated [56]:

$$C(\lambda)=\int_{-\infty}^{+\infty} I(x)\exp\left(\frac{-i4\pi x}{\lambda}\right)dx \tag{3.12}$$

In practice, this operation is done using the *fast Fourier transform(fft)* digital method of Cooley and Tukey [57] implemented in LabVIEW as *FFT.VI.*

### 3.7.3 Implementation

*a) Mirrors*

The movable and fixed mirrors are 63 by 50 mm gold coated glass mirrors. The movable mirror is mounted on a linear translation stage controlled by a *T-Cube DC Servo Motor Driver (Thorlabs model number TDC001).* It has a 6mm range of motion and a minimum linear resolution of 0.8um and a minimum repeatability of 0.2um. The driver is PC controlled with an *ActiveX* control interfaced to a LabVIEW program. There is a collimating mirror that is a 90° off-axis parabola (OAP) with a focal length of 178mm. There was a shutter at the focal length of the mirror which was used to define the source size.

*b) Beam Splitters*

We used 6um and 25um mylar (polyethylene teraphalate) beam splitters. Radiation incident on the beam splitter is partially reflected and partially

transmitted, and ideally the reflected intensity Ro is equal to the transmitted intensity To. The relative efficiency of the beam splitter is given by [59]

$$4 R_o T_o = \frac{2 R_o T_o}{(2 R_o T_o)_{Ideal}} \tag{3.13}$$

The efficiency as a function of the radiation frequency produces interference fringes or Fabry-Perot resonances. For a freestanding, non-absorbing parallel-sided, thin dielectric material, the frequency dependence of the reflectance and transmittance are [59]

$$T_o = \frac{(1-R)^2}{1+R^2-2\mathrm{R}\cos\delta} \tag{3.14}$$

$$R_o = \frac{2\mathrm{R}^2(1-\cos\delta)}{1+R^2-2\mathrm{R}\cos\delta} \tag{3.15}$$

where $\delta = 4\pi\ \omega nd \cos\theta_i$ is the relative phase shift between two emerging rays, $d$ is the thickness of the film, $n$ is the refractive index, $\theta_i$ is the angle of incidence of the beam inside the film to the surface normal and $R$ is the single bounce reflectance of the material. $R_o$ and $T_o$ depend on the polarization of the incident beam, where the reflectance $R$ depending on the polarization is given by [59]:

$$R_p = \frac{\tan^2(\theta_i - \theta_t)}{\tan^2(\theta_i + \theta_t)} \tag{3.16}$$

$$R_s = \frac{\sin^2(\theta_i - \theta_t)}{\sin^2(\theta_i + \theta_t)} \tag{3.17}$$

where $p$ represents radiation polarized with the electric field parallel to the

plane of incidence and *s* represents radiation polarized with the electric field perpendicular to the plane of incidence, $\theta_i$ and $\theta_t$ are the angles of incidence and transmission respectively. For $n = 1.6$, figure 3.11 shows the beam splitter efficiency as a function of frequency upto the first minimum. For the full frequency range, there are minima at $\delta = 2m\pi$ for $m = 1, 2, 3,\ldots$ and maxima near $\delta = (2m-1)\pi$.

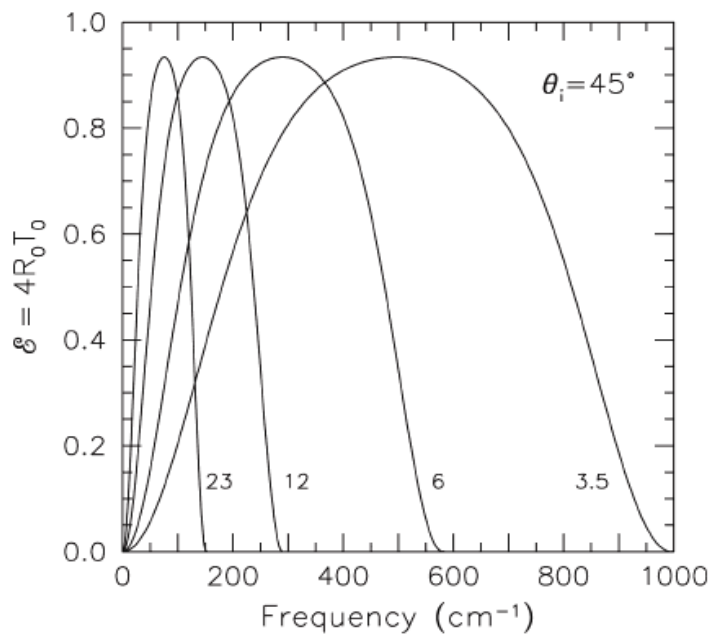


**Figure 3.11:** Mylar beam splitter efficiencies for 23, 12, 6 and 3.5um mylar thickness [59]

*c) Sources*

To measure the spectrum from the SWCNT source, the block with the mounted device as shown in figure 3.5, is placed at the focal length of the OAP, and like in the beam pattern measurements, the voltage bias is turned on and off at a modulation frequency of 100Hz. This signal is also used as the reference for the

lock-in amplifier. The other THz source which is used for alignment of the optics and calibration is a 24W SiC globar (*Newport Corp. part # 80030*). In lieu of a function generator to modulate the signal, we use an optical chopper placed in front of the the shutter.

*d) Alignment*

Alignment is crucial to acquiring an acceptable interferogram. Interferogram alignment errors include phase, modulation and sampling errors [56]. The alignment procedure detailed in [56] was followed.

*e) Data acquisition*

The signal from the detector was connected to a lock-in amplifier as earlier described, which was then connected to a computer via a GPIB interface allowing control of the data acquisition using a LabVIEW program. Allowing for real-timre visualization of the interferogram. The integration time when using the SWCNT source was 1s and 200ms for the SiC. Figure 3.12 (a) shows the block diagram of the FTS system and (b) shows a picture of the actual system.

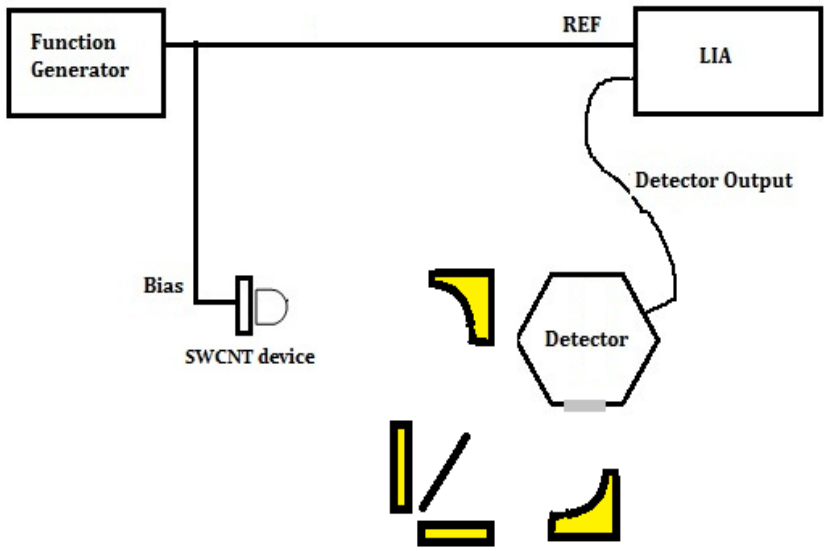


**Figure 3.12(a)** : Illustration of the FTS set-up

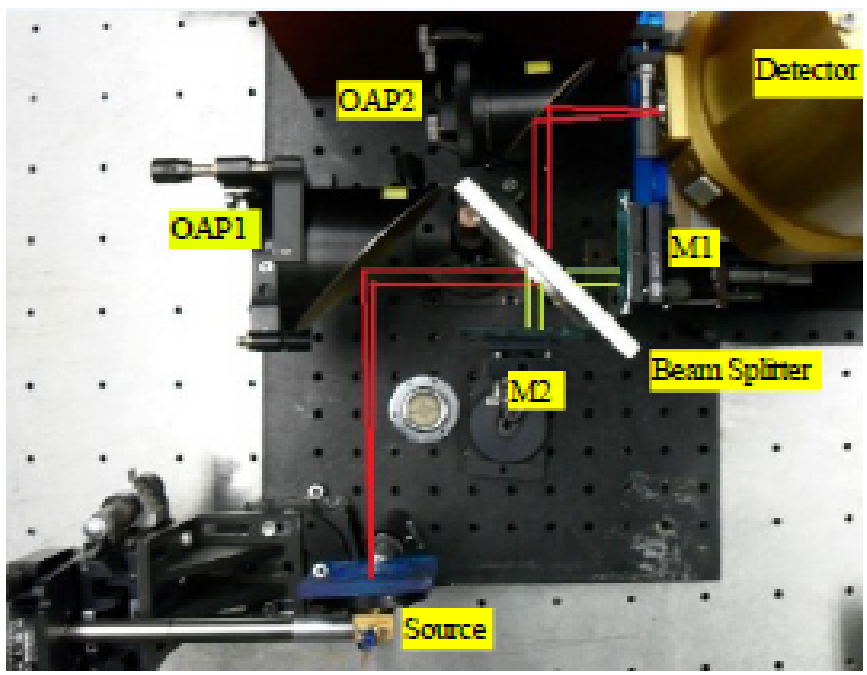


**Figure 3.12(b)**: Picture of actual FTS set-up used in measurements; Radiation from the source is collimated by OAP1 and directed to the beam splitter, where it is split into two beams, one towards the movable mirror (M1) and the other towards the fixed mirror (M2). Upon reflection, the two beams combine and part of the resulting beam is sent to the focusing mirror(OAP2)

The maximum spectral resolution for an FTS is given by [56]:

$$\Delta v = \frac{c}{2 \times maximum\, OPD} \tag{3.18}$$

In a typical measurement, the mirror moved at a velocity of 1um/s for a total distance (OPD) of 1mm. From equation (3.18) the resolution was therefore ~150GHz.

# CHAPTER 4

# RESULTS and DISCUSSION

## 4.1 Devices

THz radiation experiments were performed on a variety of devices based on either the SWCNT configuration (ropes, few tubes, mats) or the type of antenna coupling (9um bars, patch , LPA4). The SWCNT configuration was determined by the dielectrophoresis parameters used. The three main parameters are the SWCNT solution concentration, ac-voltage amplitude and time allowed for deposition. In general, the single tube devices are obtained when using a very low SWCNT solution (~$\mu L$ of CNTRENE 100 in 20mL of DI water) and the ropes and mats are formed with relatively high concentrations ( ~$mL$ of CNTRENE 100 in 20mL DI water). The ropes are obtained by using higher voltages (5-10$V_{pp}$) for longer times (>2min), while mats are obtained by using relatively lower voltages (2-3$V_{pp}$) and time (<2min). Ultimately, the type of SWCNT configuration is not unique to a particular set of deposition parameters since different combinations would achieve the same result. Optical, SEM or AFM microscopy were used to characterize the devices. Figure 4.1 and 4.2 show typical devices .

Few tubes

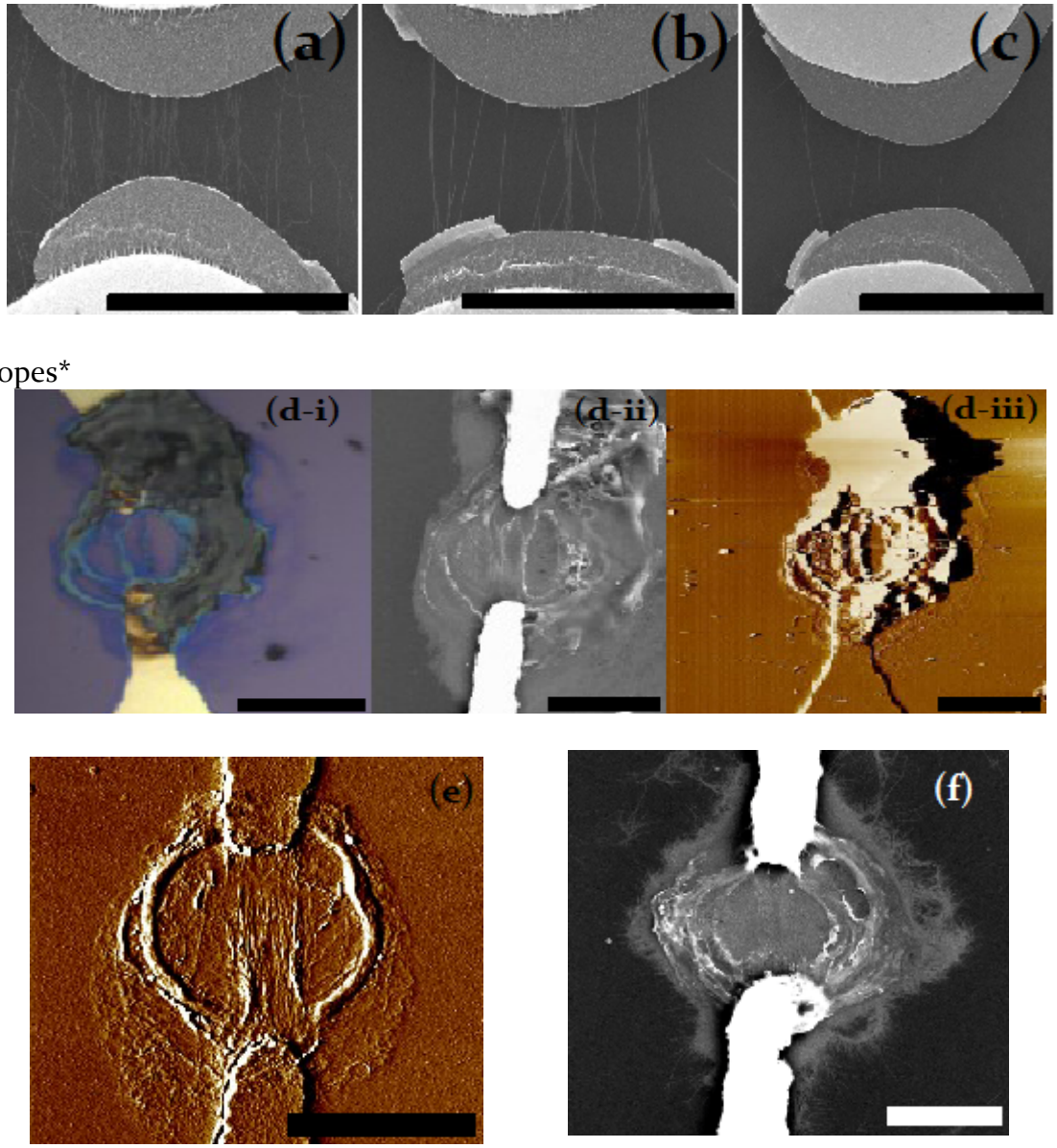


**Figure 4.1**: (a-c) SEM images of different LPA4 devices. (d) Optical, SEM and AFM images of the same rope device. (e) AFM picture of a rope device and (f) SEM picture of a rope device. Scale bars: (a-c) 4um, (d-f) 9um

* Termed 'ropes' due to the rope like structures that form after DEP.

Mats

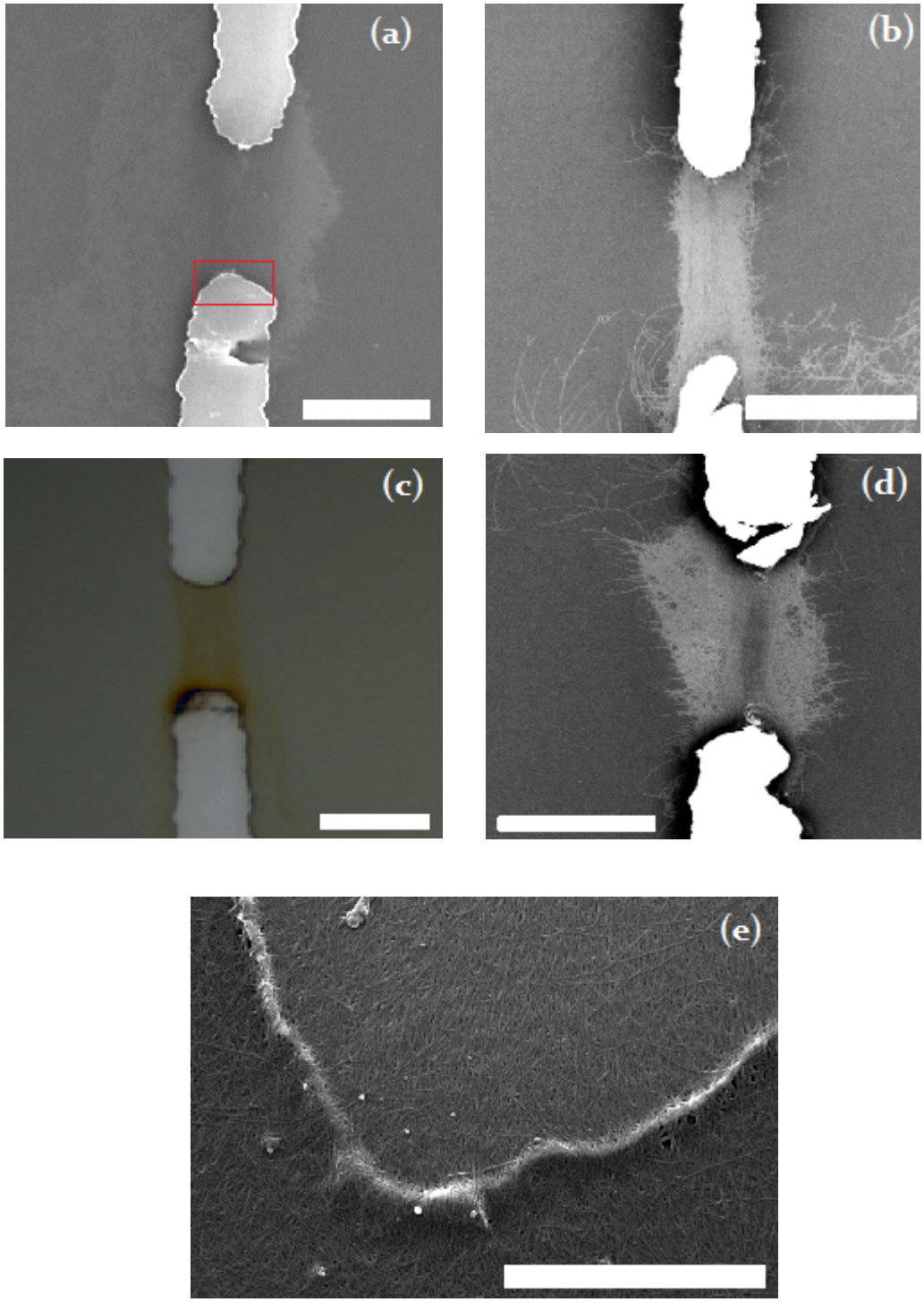


**Figure 4.2**: SEM (a, b, d) images of 'mat' devices on 9um bars. (c) Optical picture of 9um bar device. (e) close up of contact area marked by red box in (a). Scale bars (a-d) 9um, (e) 2.5um

Furthermore, we had other antenna coupled devices where we fabricated patch antennas onto otherwise 9um bar devices. This resulted in an entirely new device, with different transport and radiation properties from the underlying 9-um bar devices. Figure 4.3 shows optical pictures of several patch-antenna coupled devices with different dimensions.

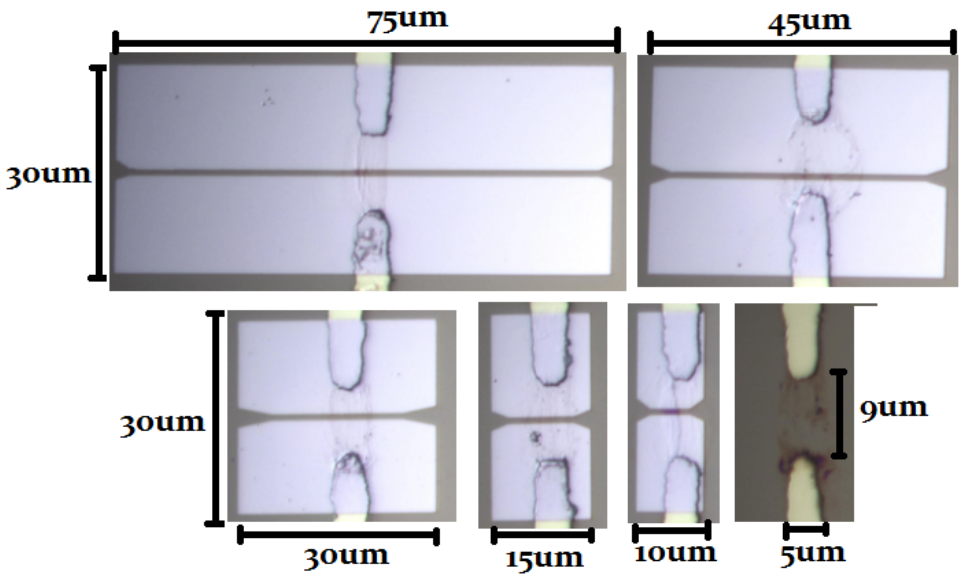


**Figure 4.3**: Patch antenna devices showing various dimensions, with the exception of the 9um device.

Besides having patch antennas, this device configuration is unique because it transforms the highly networked (disordered) nature of films as shown in figure 4.2, by confining the SWCNTs to the gap area formed by the patch antennas. The resulting SWCNTs are relatively well aligned across the gap as shown in figure 4.4. While some of the disorder from the films is evident with some tubes traversing horizontally across the gap, a majority of the tubes run almost parallel to each other, and by varying the gap length, we vary the SWCNT lengths also.

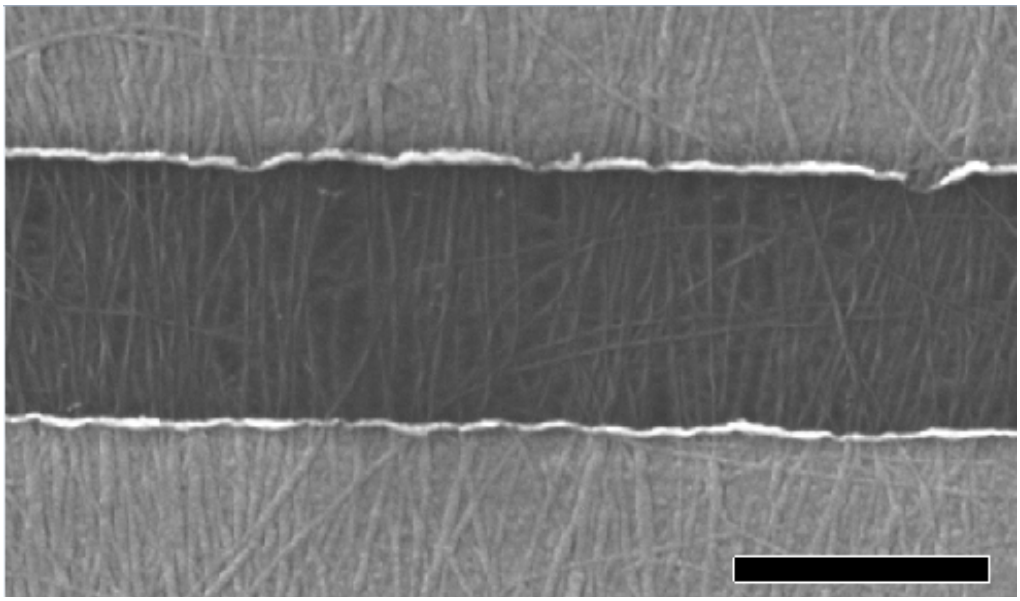

**Figure 4.4**: SEM picture of a close up of the gap area of a patch antenna device. Scale bar 1um

The other main class of antenna devices were the suspended ones as shown in figure 4.5. Here, as described in chapter 3, DEP was done last in the fabrication procedure.

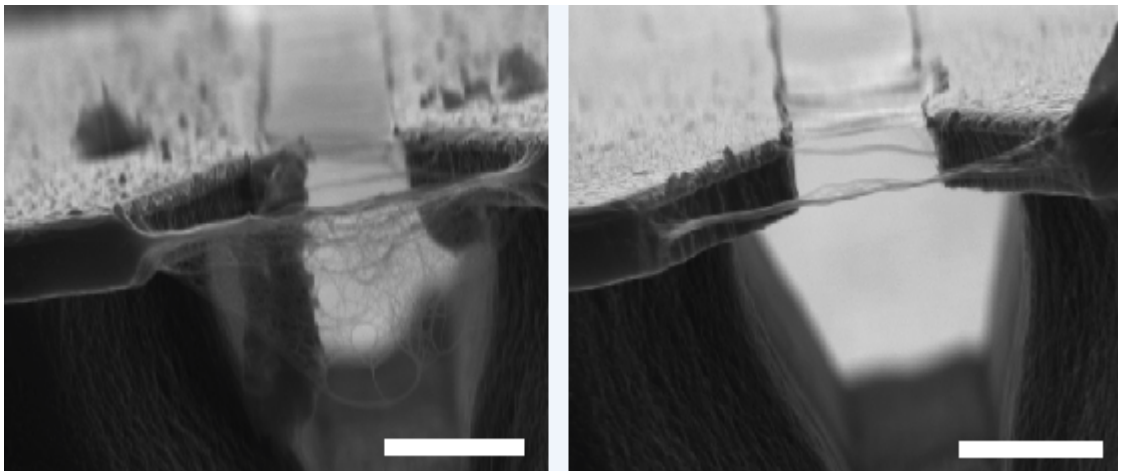

**Figure 4.5**: SEM pictures of two SWCNT devices suspended over a trench made through RIE of the oxide . Scale bars: 1um

## 4.2 Transport Measurements

The transport properties of the devices are indicated by the current-voltage (I-V) characteristics, investigated using a two-probe measurement set up. The different SWCNT configurations observed via imaging also manifested themselves in these transport measurements. I-V curves characteristics were the main factor to consider before testing a device for its radiation properties. Typical I-V characteristic curves for some representative devices are shown in figure 4.6.

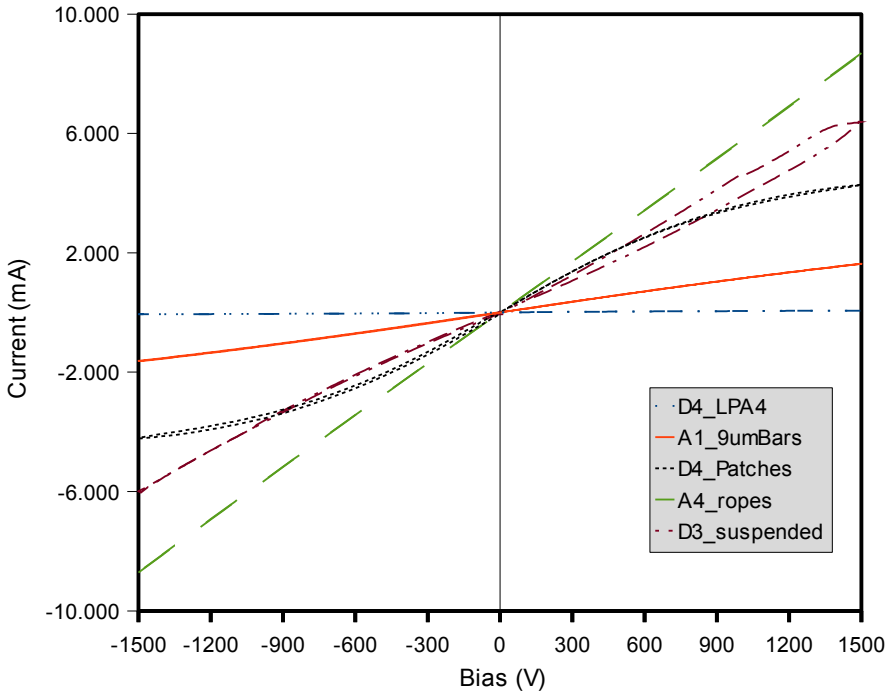


**Figure 4.6**: I-V curves for device 4.1(c) blue curve, 4.1(d) green curve, 4.2(b) red curve, 4.4 black curve, and 4.5(b) purple curve,

The main information garnered was the amount of current each device was able to carry. The rope and mat devices exhibited relatively ohmic behavior, while the few tube and patch devices exhibit non-linear behavior. The ohmic nature of ropes can be explained by the availability of many transport channels that dominate

the conductance. The multiple conduction channels ultimately saturate the conductivity of the SWCNT rope networks [60]. In the SWCNT mats the I-V curves are also approximately ohmic, for the same reason, but with less current density.

### 4.2.1 Current saturation

Devices with Palladium top contacts almost invariably exhibit current saturation. Palladium as a top contact is known to yield ohmic contacts with SWCNTs[61], a prerequisite for current saturation[62]. While the Palladium contacts we had were not perfectly ohmic they fell in the low resistance contact (LRC) category that was earlier described in chapter 1 of this thesis. With those types of contacts, we are able to see the effects of scattering, especially by optical phonons, that resulted in current saturation [64]. The black curve in figure 4.6 indicates current saturation in higher biases. Figure 4.7 shows the before and after top contact fabrication I-V curves, where the improvement in the contact resistance was indicated by the current saturation.

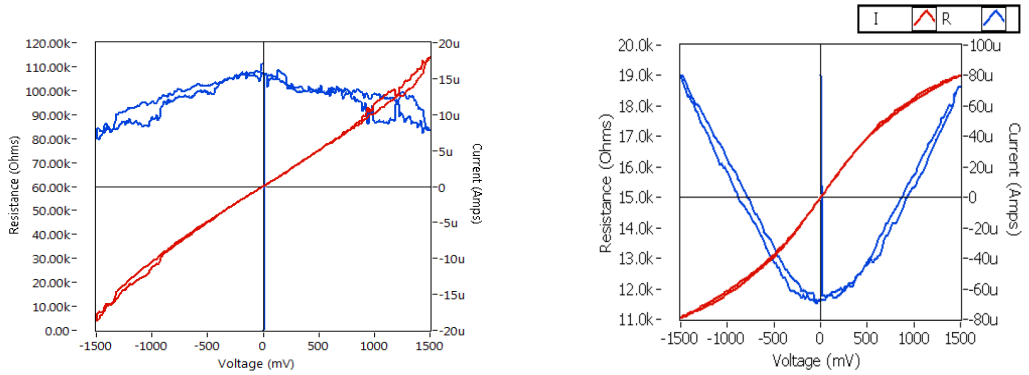


**Figure 4.7**: I-V curves for device 4.1(c) before (left) and after (right) Palladium top contact. Blue curves are for resistance (right axes) while red are for current (left axes)

It has been mentioned that the SWCNT effective length was determined by the gap size as in figure 4.4, and in figure 4.8 we see the effect of length scaling on the I-V curves. Optical phonon scattering is more pronounced in short SWCNTs as they have lower resistance [11]. Network effects like inter-tube junction resistances are also expected to be less.

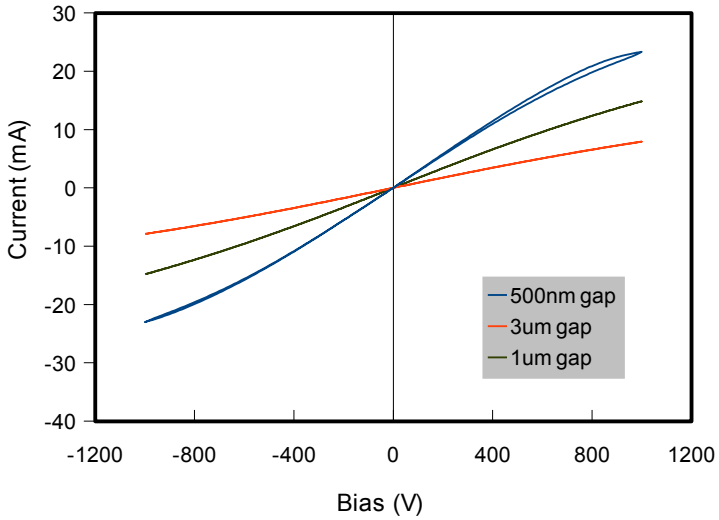


**Figure 4.8**: I-V curves for three patch antenna devices with different gaps

### 4.2.2 Contact Barriers

In the absence of perfect contacts between the metal and SWCNTs, there are contact barriers [63] which present a finite resistance. Room temperature electron transport across the barriers is achieved through tunneling [63]. Although low temperature studies are not an integral part of this work, we took I-V curves at cryogenic temperatures for some devices. Figure 4.9 shows the I-V characteristic curves for devices in figure 4.4 and 4.1(c) at several temperatures below 300K.

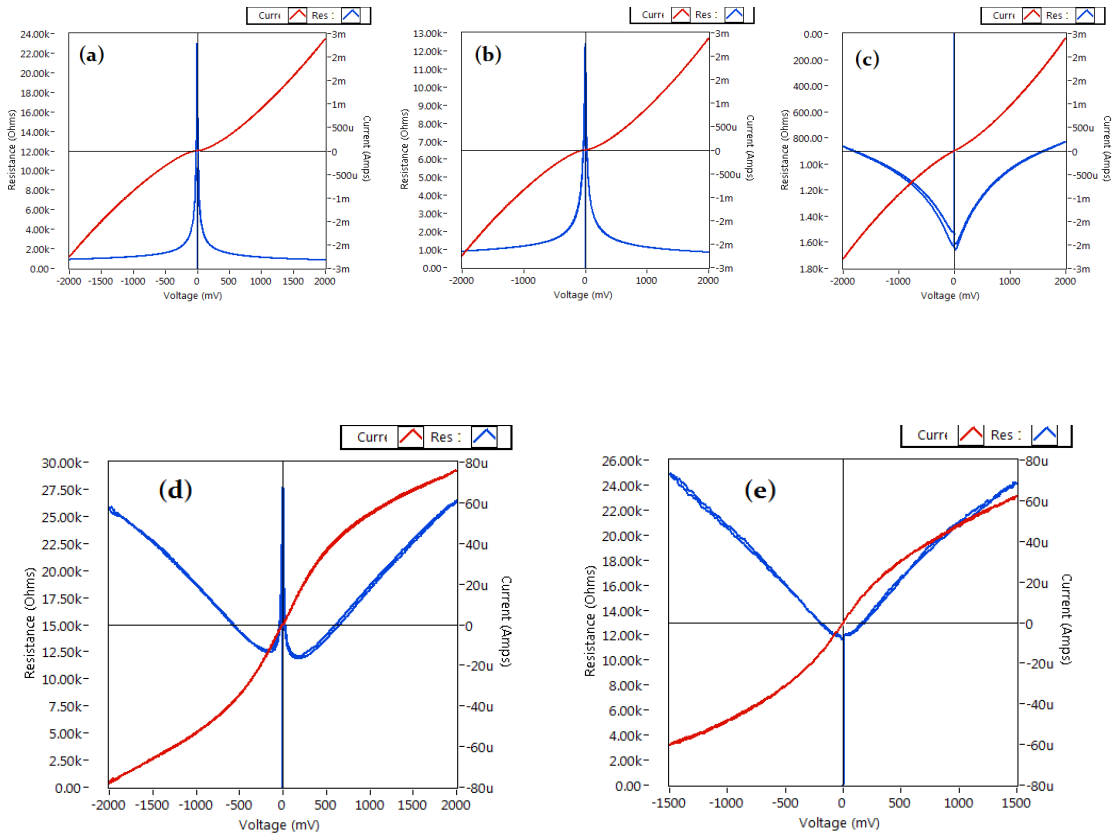


**Figure 4.9**: (a-c) IV Curves for device in figure 4.4 at T=4.2K, 65K and 135K respectively. (d-e) IV curves for device in figure 4.1(c) at T= 4.2K and 293K respectively. Blue curves are for resistance (right axes) while red curves are for current (left axes)

At the low temperatures, near zero bias, we see that the device resistance is relatively high, but decreases with increasing bias. The resistance in this region is dominated by the contact resistance . This is an effect of the contact barriers: at low temperatures and bias, electrons lack enough energy ($E=K_bT$) to tunnel through the barriers. With increasing bias, electrons gain enough energy to tunnel through the barrier, and the resistance that we see thereafter is due to the SWCNT

### 4.2.3 Annealing

The overall effect of annealing was to lower the contact resistance. Devices were annealed after DEP, top contact fabrication or SEM imaging. The change of resistance after annealing was due mainly to out-gassing of adsorbed oxygen and other impurities at the metal - SWCNT contact [66]. In the band diagram picture, the annealing step lines up the bands at the metal - SWCNT junction thereby lowering the barrier and enhancing current injection from the metal to SWCNT [63]. Furthermore, the heat from annealing allows for the healing of defects and alignment of tubes within bundles [68]. Figure 4.10 shows an example of resistance change for devices in figure 4.1(c) and 4.4 due to annealing, after a resistance change caused by SEM imaging, likely due to build up of charge that consequently increases the contact resistance.

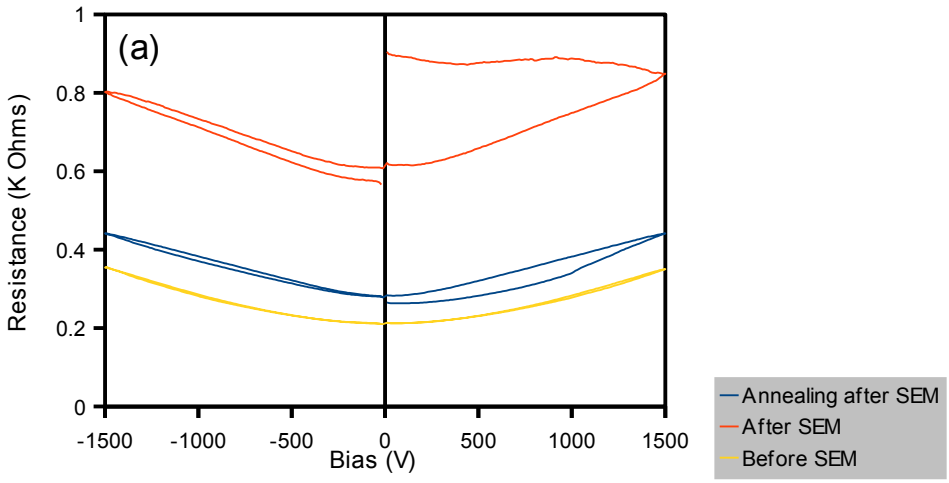


**Figure 4.10(a)**: I-V curves showing effect of SEM and subsequent annealing on the resistance.(a) device in figure 4.4 and b is device in figure 4.1(c)

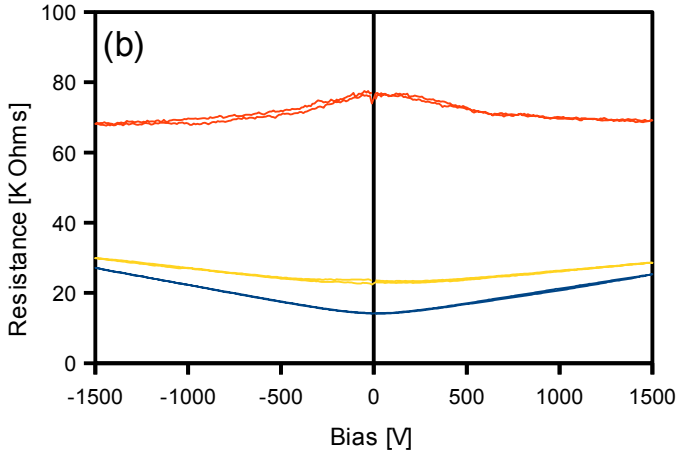


**Figure 4.10(b)**: I-V curves showing effect of SEM and subsequent annealing on the resistance.(a) device in figure 4.4 and b is device in figure 4.1(c)

Investigation into any gate dependence was not comprehensively done but preliminary measurements showed no observable gate modulation effect. We assumed that the DEP process deposited primarily metallic tubes, an assumption justified by the high current densities and regularly ohmic I-V characteristic curves, properties primarily attributed to metallic SWCNTs. Since semiconducting tubes have a much higher resistance, their effect would be negligible on the total resistance. SiO2 passivation resulted in ~ X5 resistance increase regardless of the type of device. It is not clear why SiO2 passivation increased the resistance, but passivated devices could withstand relatively high bias, up to 15V without electrical breakdown. The lack of air (oxygen) in the vicinity of the SWCNTs meant that the SWCNTs would not readily oxidize and breakdown [67]. In summary, we highlight the four main factors that determined the SWCNT transport properties:

- SWCNT Configuration
- Top contacts
- Annealing
- Passivation

### 4.3 Radiation Patterns

The quasi- optical coupling scheme (figure 2.18) allowed us to perform radiation pattern measurements as shown in figure 3.7. Since the radiation pattern was primarily determined by the Si lens, most of the measured patterns have the same basic shape and change mainly due the varying power levels among devices. Figure 4.11 shows typical radiation patterns for some devices in the two perpendicular directions.

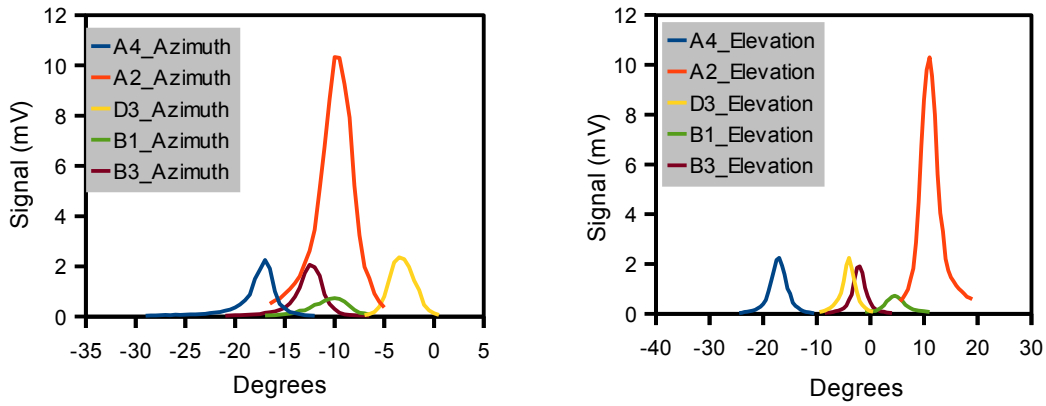


**Figure 4.11**: Beam patterns for a variety of devices in the Azimuth and Elevation directions

We see the varying power intensities among the various devices and the angular dependency of the peaks. Sources that were not at the center of the lens, as

shown in figure 2.17, radiated off- axis and therefore the peaks did not occur at 0°. We define the axis at 0° to be normal incidence on the dewar window and therefore also normal on the detector. In 4.11(a) the radiation from all the devices was offset to the left of zero: a possible reason for *all* of the spectra to be offset in the same direction would be that the detector was also off-axis. Another reason as shown in figure 2.19, is an off-center source. This seems unlikely though since (i) it requires an unrealistically large misalignment (~1 mm) and (ii) that the misalignment occur consistently in one direction. Finally, collective phase shift causing the beam to be steered in one direction, due to some partial coherence in the radiation. Resolving this issue will require further investigation. Centering the spectra and showing the results in dB, as shown in figure 4.12 shows the various beam widths. We conclude that the beams are diffraction limited, with -3dB beam widths between 2-5°,

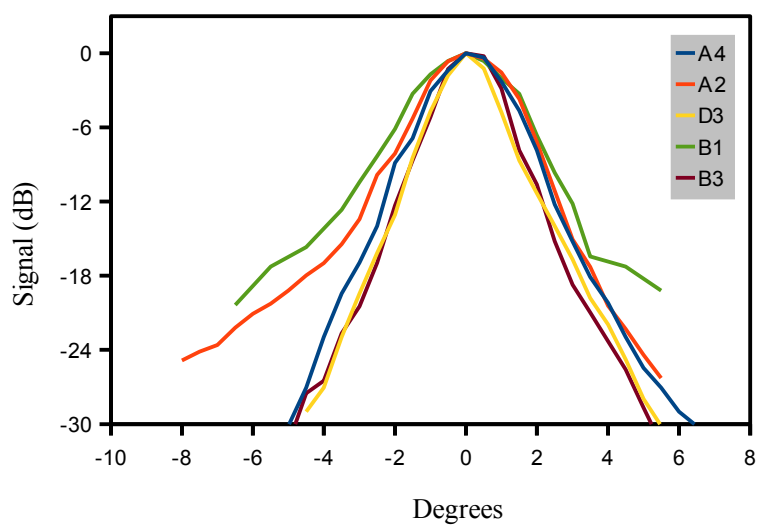


**Figure 4.12**: Normalized beam pattern results for the elevation results in 4.11(b)

Results for the radiation patterns in the near and far fields ( > ~$D^2/\lambda$) are shown in figure 4.13.

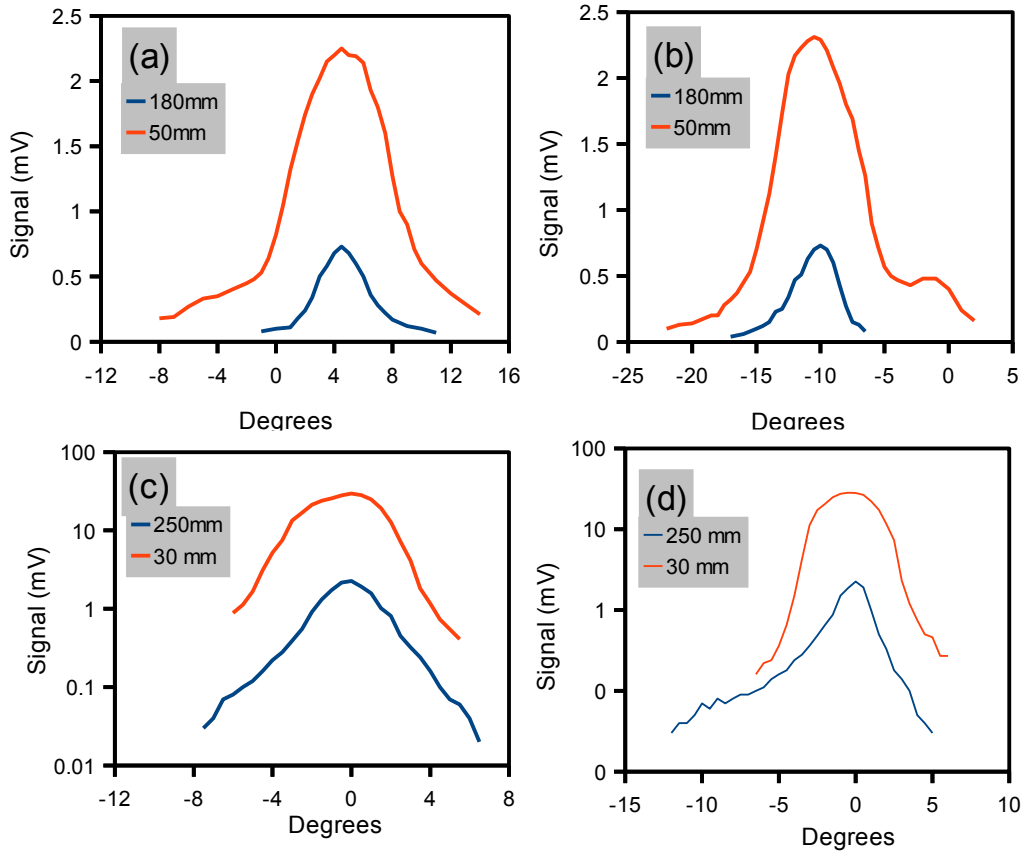


**Figure 4.13**: Typical beam pattern results - (a,c) elevation and (b,d) azimuth.

We see that the near field patterns have wider -3dB beam widths of ~ 6-10$^0$. This is expected since in the near field, the beam is a collimated cylinder (figure 2.18) with about 4mm diameter. Furthermore, in (b) we see an extra peak at in the near field pattern. The small peak is a coma lobe due to aberration caused by an off axis source [69]. Knowledge of the beam patterns will be important when designing SWCNT source detector configurations.

## 4.4 Spectra

A major result of this work is the spectral distribution of the radiation produced by SWCNT devices. As discussed in chapter 2 and 3, there are expectations and predictions as to what the spectrum would be, however, the results we get using Fourier-transform spectroscopy are not purely indicative of the source's spectral distribution. They are also determined by the materials that make up the FTS system, mainly, the beam splitter, the HDPE dewar window, filters and atmosphere (specifically water content). The transmission through the materials is described by equation (3.12), and ultimately shows up in the spectral results. There is no way around this, and it is one of the inherent disadvantaged of Fourier-transform spectroscopy.

While the transmission function for these materials is known, figure (3.11) for beam splitter and Appendix for the filters, it is important to get the actual system response. This was accomplished by using a broadband thermal source , a SiC globar, whose specifications were given in chapter 3. While the peak wavelength was specified at ~1um (300 THz) we assume it had a relatively flat spectrum in the THz range of interest. Therefore, using this source and a variety of beam splitter and filter combinations, we expect to retrieve the overall system response. Figure 4.14 shows the spectral results using the two different bolometer detectors. 4.14(a) and (b) are from bolometer 1, while (c) and (d) are from bolometer 2. The main difference between the two bolometers is the different cut-off filters, evident from

the spectra.

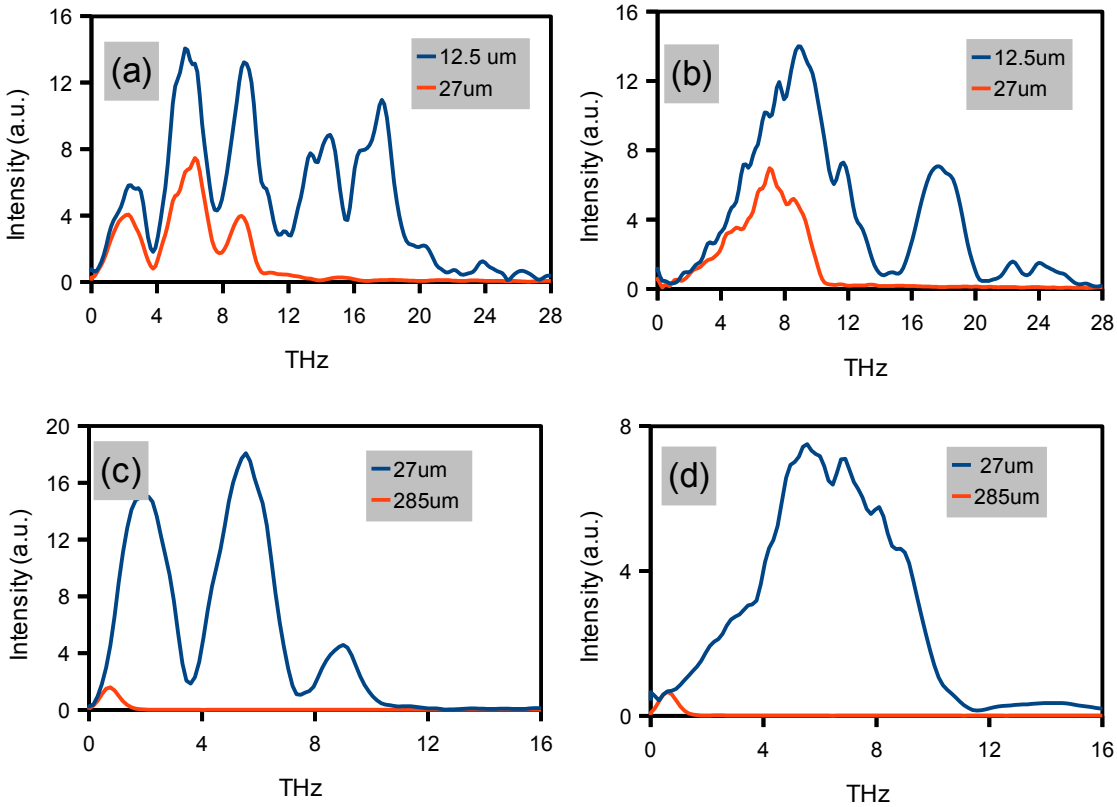


**Figure 4.14**: SiC globar radiation spectra with different filters(shown in legends) taken with bolometer 2 (a,b) and bolometer 1(c,d). (a,c) taken using 25um Mylar, (b,d) taken using 6um Mylar

Spectra from the 25um mylar, (a) and (c) , show the expected Fabry-Perot resonances at every 4THz until the respective filter cutoffs occur. For the 6um mylar, the first Fabre-Perot resonance is noticeable only when using the 12.5um(24THz) filter, blue curve in (b), whereas the 27um and 285um filters cutoff the response at lower frequencies. The main conclusions we drew from these results in figure 4.14 are:

- The 25um beam splitter had  better effieciency at the low frequencies (0-4 THz) save for the beam splitter dips. Since the absorption measurements [12] have a THz peak at this range, this beam splitter is ideal assuming the emission spectra followed the absorption.
- The system has the highest efficiency at ~ 8THz for bolometer 2 and ~6THz for bolometer 1. This was relevant because it implied that otherwise relatively low signals in this range will be better transmitted through the system.

With the two broad conclusions, we can begin to compare SWCNT spectra from different types of devices.

### 4.4.1 Device Comparison

We started off by defining two types of devices: a) 9um bars and b) patch antenna devices. As described earlier, the 9um bar devices form the basic structure on which the patch antennas are later fabricated onto. The antenna dimensions of interest are shown in figure 4.15, and are marked L, W and g.

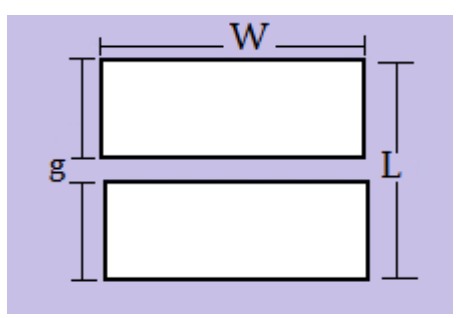


**Figure 4.15**: Patch antenna showing dimensions of interest

Figure 4.16 is a comparison of the devices with different *W* values, taken using the 27um(24THz) filter in bolometer 1. The results were normalized to the largest peak in each case. Lower *W* (15x30 um) shifted the emphasis to the lower frequency *($f_1$)* while increasing *W* (45x30 um) shifted the spectrum to a higher frequency peak *($f_2$)*. The intermediate *W* (30x30um) yielded two peaks with comparable intensity. Note that while the spectrum shifts from one peak to another, the two peaks occurred essentially at fixed frequencies.

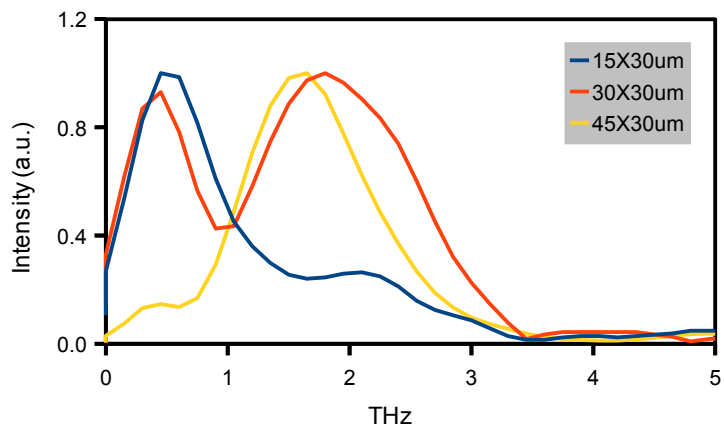


**Figure 4.16**: Spectra from three patch antenna devices with varying *W*

Figure 4.17 shows the result of varying the parameter *L* for a fixed *W* (45 um). There was a clear dependence, where a higher *L* value tuned the higher frequency peak to a relatively lower frequency.

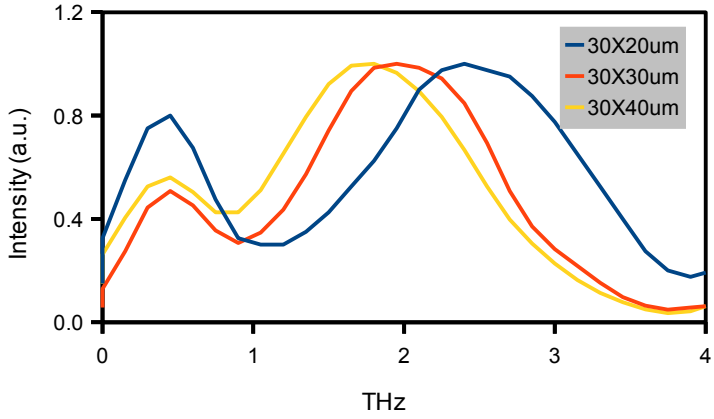


**Figure 4.17**: Spectra from three patch antennas devices with varying *L*

Figure 4.18 shows the results of varying *g* (3um, 1um, 500nm), for 45x30 um patches

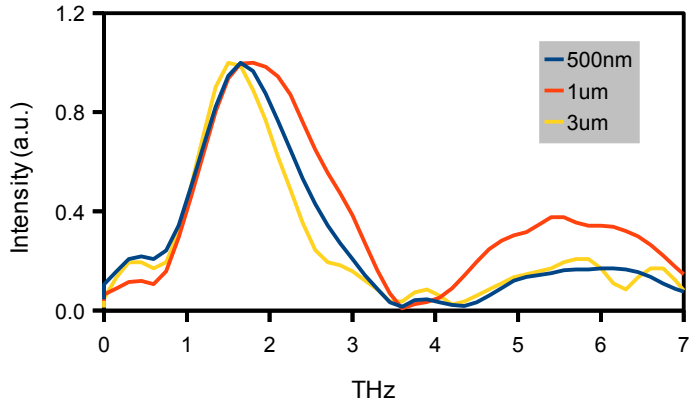


**Figure 4.18**: Spectra from three different patch antennas with varying *g*

Evident from the figure, there was no clear trend when we changed the gap length *g*. Nevertheless, by changing *g*, we changed the effective SWCNT length, and consequently expected to probe any length modulated geometric resonances [38]

predicts plasmon resonances that depend on the length and that furthermore, are affected by the mean free path. Therefore, by varying *g*, as earlier described we effectively varied the SWCNT length. We conclude that there is no observable dependence of the spectrum on the SWCNT length. However, it appears that the patch antennas dominate the spectrum and any effect of the length or order of the tubes across the gap is washed out. The question as to whether or not we can observe plasmon resonances is left for future work.

Figure 4.19 is a comparison of two 9um bar devices (without patches), one with an $SiO_2$ passivation layer and the other without passivation. The two spectra have the same main feature, the single broad peak, which contrasts the prior results of figures 4.16,4.17,4.18. This result supports the conclusion that the patch antennas determine the resonances (and not the SWCNTs)

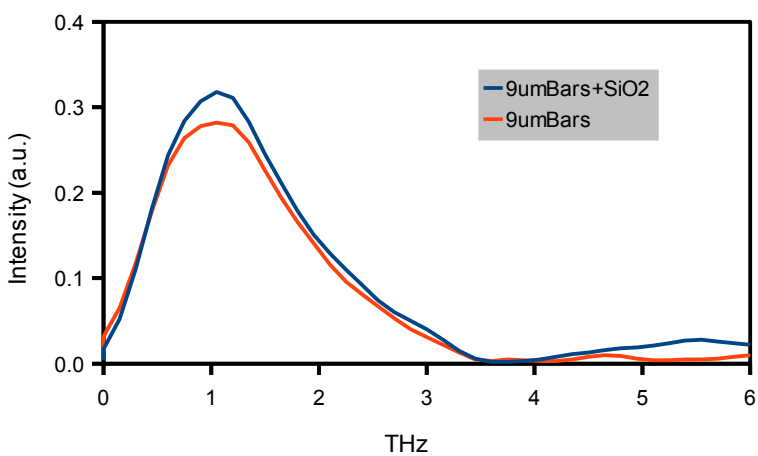


**Figure 4.19**: Spectra from 9um bar coupled devices

In summary, we draw the following conclusions from the various spectra; We note that the patch antennas have two resonances which we interpret as coupled resonances:

- Resonance $f_2$ is a dipole type resonance due to the patches, and is not sensitive to $W$ or $g$.
- A resonance near $f_1$ occurs both with patches (Figure 4.16,17,18) and without (4.19). This resonance must be related to dipole radiation from the 9um bar structure . $f_1$ is emphasized by making $W$ smaller, which would facilitate feeding the currents from the SWCNTs through the patches to the 9um bars.
- Suspending the SWCNTS results in similar spectra (not shown) to those of devices with on-substrate SWCNTs. We observed that the spectra are dominated by antenna effects and not due to intrinsic SWCNT properties.

### 4.4.2 Bias Dependence

Based on the Joule heating model of emission, changing the electronic temperature changes the electronic distribution and therefore the intensity of the emitted radiation. To investigate the bias dependency, we experimented with 9um bar devices, patch-antenna devices and suspended tubes as shown in figure 4.20

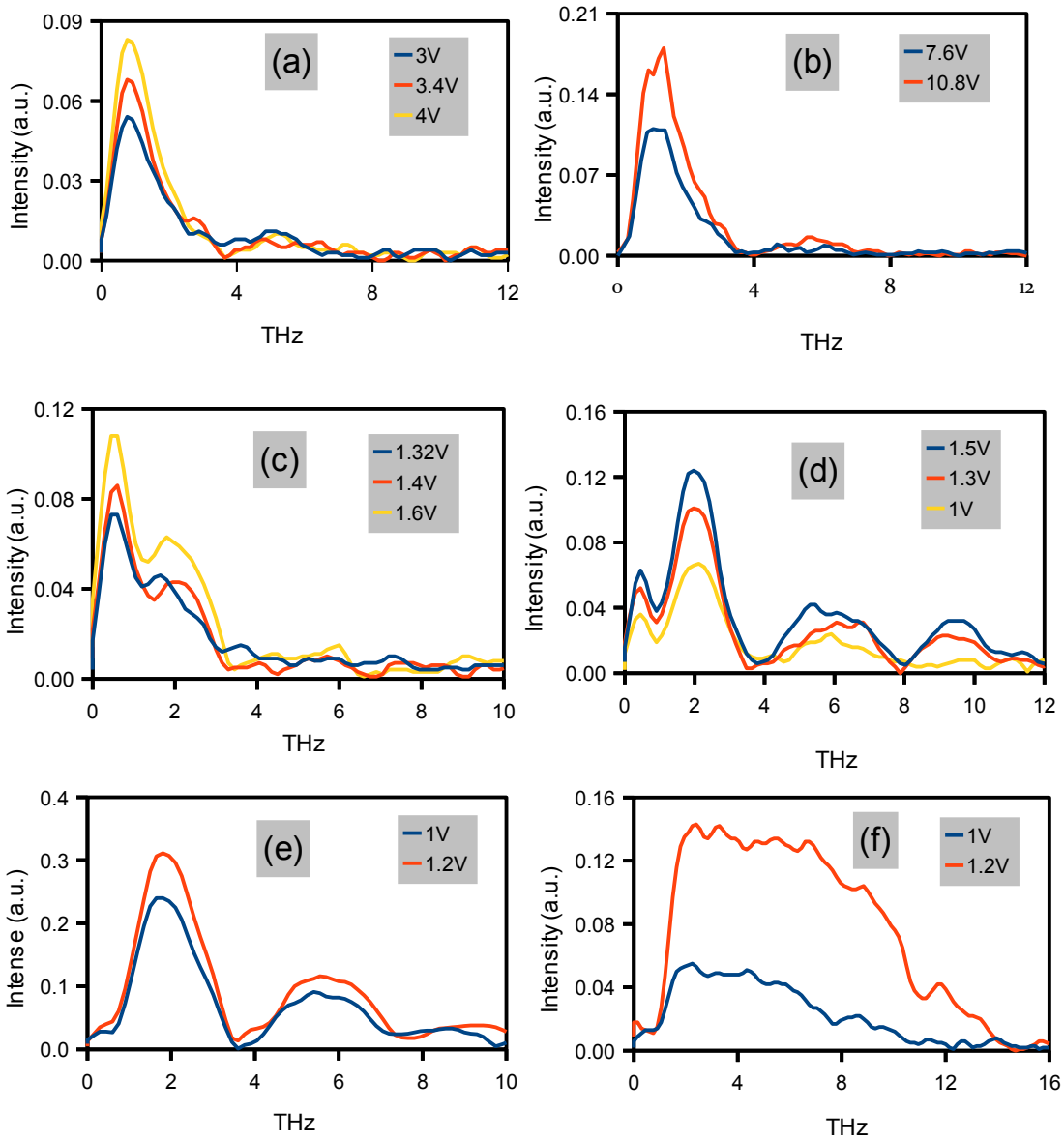


**Figure 4.20**: Spectra showing bias dependency for 9um bars(a,b), patch devices (c,e,f) and a suspended device (d). (f) is from same device as (e) but taken using 6um mylar

Increasing the bias voltage increased the total power emitted, but did not modulate the peak frequency, indicating that the spectrum was determined by the antenna.

## 4.5 Polarization

The polarization of the THz beams were measured using a wire grid polarizer placed in the path of the beam. Table 4.1 shows some typical results from polarization measurements when the electric field was horizontal and vertical respectively.

| | | Signal (mV) | | | |
|---|---|---|---|---|---|
| **Device** | **Type** | **No Grid** | **Horizontal** | **Vertical** | **Ratio(V/H)** |
| A2 | Patch | 10.5 | 3.85 | 7.6 | 1.97 |
| B3 | Patch | 1.85 | 0.5 | 1.5 | 3 |
| B1 | Patch | 1.2 | 0.25 | 1.02 | 4.08 |
| D3 | Patch_Suspended | 2.2 | 0.61 | 1.77 | 2.9 |
| A2 | LPA2 | 0.18 | 0.1 | 0.1 | 1 |
| A4 | 9um Bars | 2.12 | 1.51 | 1.55 | 1.03 |

**Table 4.1**: Typical Results from polarization measurements

From the results, the E-field is perpendicular to the slots and parallel to the SWCNTs. In general, the polarization ratio,defined as vertical/horizontal signal is ~ 2-4 for antenna coupled devices and ~1 for 9um bar coupled devices.

## 4.6 Power Considerations

The THz output from the SWCNT devices varied linearly with the dc input power ($P_{input} = I^2R$) needed to produce THz radiation, as shown in figure 4.21 (a). This was consistent with an assumption that the radiation was thermal, that is $P \alpha \Delta T$, where $\Delta T$ is the temperature change due to the dc bias. Power calibration was performed as described in section 3.5. Results for laser attenuation using the

manilla folders are shown in figure 4.21 (c) and (d) for the 184um (1.63 THz) laser line. (b) shows results from bolometer 1, obtained using the 27um filter and (c) for bolometer 2 obtained using the 12.5um and 27um filters.

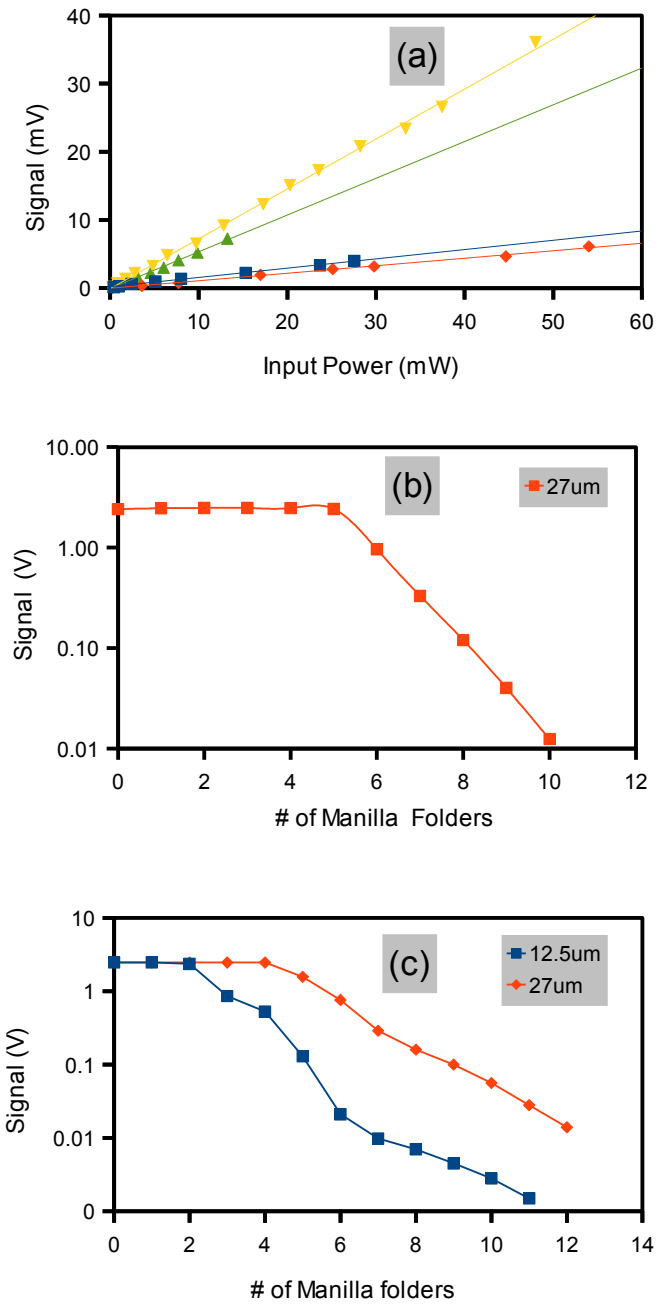


**Figure 4.21**:(a) Results for output signal versus input power for a variety of devices and signal attenuation per manilla folder for bolometer 1 (b) and bolometer 2 (c).

In 4.21 (b) there were two regions: first when the bolometer was saturated and the signal independent of the # of manilla folders and the region after 5 folders where the signal fell off linearly with every additional folder.

In (b) however, there were three regions: one when the bolometer is saturated and thereafter two regions with different slopes. We consider the bolometer to be unsaturated after 6 folders, and ignore the intermediate part. Following section 3.5, we find:

*Bolometer 1 Results:*

A = 2.386 $A^{10}$ = 5980

$$Power\left(\frac{W}{mV}\right)=\frac{10^{-3}(W)}{5980}\times\frac{1}{124(mV)} = 13.5\times10^{-9}=13.5\ \left(\frac{nW}{mV}\right)$$

*Bolometer 2 Results:*

$A_{12.5um}$ = 1.455 $A^{11}$ = 62.1

$A_{27um}$ = 1.94 $A^{12}$ = 2842

$$Power_{12.5um}\left(\frac{W}{mV}\right)=\frac{1.7\times10^{-3}(W)}{62.1}\times\frac{1}{1.5(mV)} = 18\times10^{-6}=18\ \left(\frac{\mu W}{mV}\right)$$

$$Power_{27um}\left(\frac{W}{mV}\right)=\frac{0.55\times10^{-3}(W)}{2842}\times\frac{1}{14(mV)} = 13.82\times10^{-9}=13.82\ \left(\frac{nW}{mV}\right)$$

The result from the 12.5um filter in 4.21(c) shows an unexpected attenuation curve, with varying slopes and could explain the inconsistent power calibration result. We therefore focus on the results from the 27um filters.

In the course of this work, we have had SWCNT sources with signals as strong as 100mV from rope device like in figure 4.1(d) and ~31mV from patch antenna devices like in figure 4.4. Furthermore we've measured signals as meager as 1mV. Using the calibration results, we estimate that our devices have power in the range of:

$$13\,nW \;\leq\; \boldsymbol{P}_{\boldsymbol{SWCNT}} \;\leq 1.3\,\mu W \qquad (Rope\ devices)$$

$$13\,nW \;\leq\; \boldsymbol{P}_{\boldsymbol{SWCNT}} \;\leq 465\,nW \qquad (Patch\ antennas)$$

We note that this power is lower than the actual source power due to losses in system, specifically through the Silicon lens (~30% loss) and air.

To compare with the power given by the Nyquist formula: $P = K_b BT$, we estimate the bandwidths as shown in figure 4.22, to account for the beam splitter effect and estimate nominal SWCNT temperatures based on [67] .

Therefore, assuming impedance match, with

$$B \sim 2\text{-}3\ \text{THz} \quad \text{and}$$

$$\Delta T \sim 200\text{-}500$$

We get,

$$5.5\,nW \;\leq\; \boldsymbol{P}_{\boldsymbol{Nyquist}} \;\leq\; 20.7\,nW$$

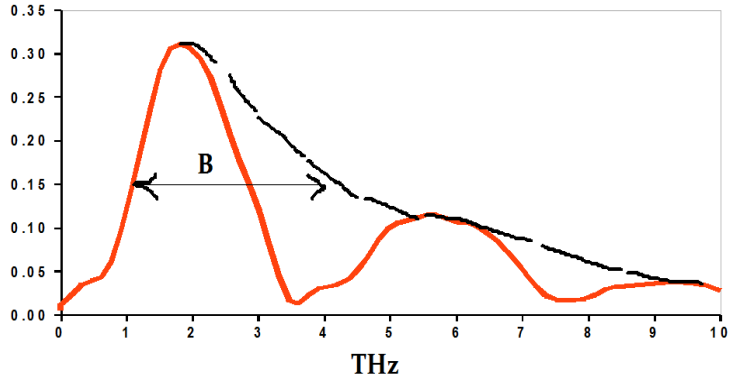


**Figure 4.22**: Bandwidth estimation illustration

For the devices with relatively high signals measured close to the bolometer, it is possible that they had a high level of side lobe power in their antenna pattern, spread over wide angles and would therefore not be detected in the far field measurement. Nevertheless, as long as we can rely on the power calibration method, we seem to be exceeding the theoretical Nyquist limit as shown in the results.

# CHAPTER 5

# FUTURE WORK

## 5.1 Antenna Designs

So far in this work we have primarily coupled SWCNTs to patch antennas and have successfully measured spectra from such devices. The results indicate that the main resonances were determined by the antenna, and could be tuned by changing the antenna dimensions. We therefore propose to couple SWCNTs to different types of antennas, specifically bow-tie and slot antennas as shown in figure 5.1. Due to the different antenna properties like bandwidth and efficiency, using a variety of antennas may allow us to tune the resonances differently or observe resonances mediated by the SWCNTs (instead of the antennas).

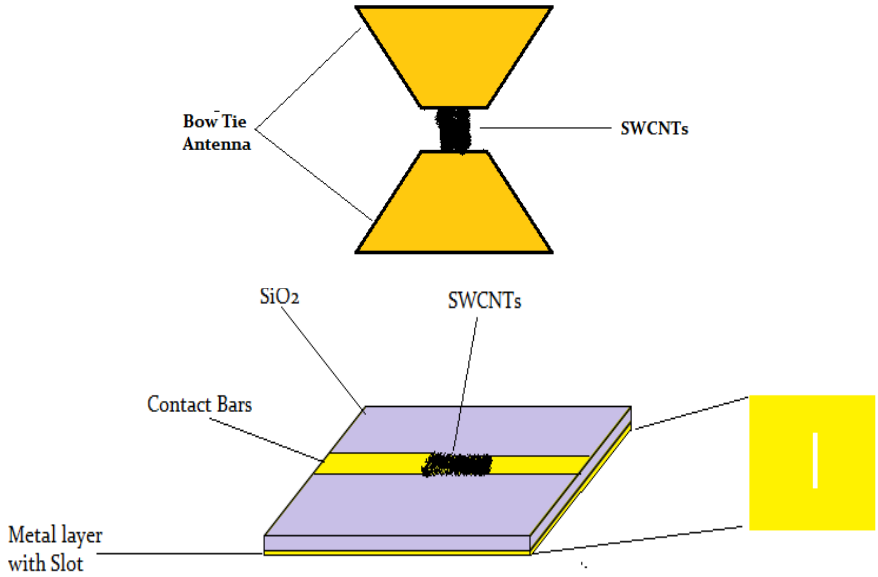


**Figure 5.1**: Antenna-coupling schemes.(top) Bowtie (bottom) Slot

## 5.2 THz Detection Using Patch Antenna devices

From our previous work in THz detection using SWCNTs, we primarily employed Log-periodic antennas for coupling [70,71]. Since the patch antennas have shown good response in the 0.5 – 2.5 THz range, depending on the antenna dimensions, we will seek to investigate THz detection in the same devices. We expect to correlate the responsivity to device dimensions for a given frequency. Furthermore, since the patch antennas offer a wider area on which to suspend devices, we expect to observe better responsivity from our previous work in detection using suspended SWCNTs, due to an enhanced bolometric effect.

## 5.3 Terahertz Integrated Circuits

The main idea behind a THz IC is the integration of the source and detector on the same circuit. The source would be a SWCNT based emitter as described in this work, while the detector could be a microbolometer like Niobium [72], a SWCNT detector [70] or a CMOS based detector [73]. The main requirement is that they be lithographically compatible with the source. Transmission between the source and detector could be achieved through microstrips/waveguides. The implementation of such a circuit could pave way to a more sophisticated system, like an on-chip THz imaging system [73] .

## APPENDIX A

## PROCESS PARAMETERS

Reactive Ion Etch (RIE): STS Vision 320 Mark II RIE System
Target: $SiO_2$

- Process pressure: 40
- RF Setpoint: 250
- Stabilisation time: 15
- Steptime (m): 10
- CF4 (6): 24
- O2(5): 6

Plasma Enhanced Chemical Vapor Deposition (PECVD): STS Vision 320 Mark II PECVD System
Material: $SiO_2$

- Cload Position: 50
- Ctune Position: 50
- Drive match: 1
- Process Pressure: 800
- RF Setpoint: 30
- Stabilization time: 30
- Steptime(m): ~10min
- 2%$SiNH_4$/N2 (1): 400
- $N_2O$(3): 1420

Sputtering: ATC ORION 8 UHV
Material: Palladium

- Gun parameters: DC, 750W, 100V, 1000mA
- Argon flow 12 SCCM
- Power STPT(%) 26.70
- Shutter Delay: 15.0
- Coat time: 95s

UV Ltihography: Suss MicroTec MA6 Mask Aligner:
a) Wafer preparation for 1813 Positive photoresist

- HMDS: 3000*rpm*, 15*s*
- s1813: 3000rpm, 30s
- Softbake: 120$^o$s, 60s
- Exposure using 20mW/cm$^2$, 3s, vacuum contact
- Toulene Soak, 5min, blow dry

- Develop using Shipley 351 for 60-90s
- DI rinse followed by $N_2$ blow dry

b) Wafer preparation for 1813 Positive photoresist: *Suss MicroTec MA6 Mask Aligner*

- HMDS: 3000RPM, 15S
- NR9-1000: 3000rpm, 30s
- Softbake: 150°c, 60s
- Exposure using 20mW/cm$^2$, 2s, vacuum contact
- Post exposure bake: 100°c, 60s
- Develop in RD6 for 8s
- DI rinse followed by $N_2$ blow dry

Ebeam Lithography

- Acetone followed by IPA
- PMMA: 1500rpm, 60s
- Softbake: 180°c, 60s
- Exposure using JEOL JSM-7001F Ebeam Writer with Nanometer Pattern Generation System (NPGS v.9)
- Develop in MIBK:IPA (1:3) for 60s
- IPA rinse for 20s
- DI rinse for 20s followed by $N_2$ blow dry

## APPENDIX B

## INTERFEROGRAMS AND SPECTRA

**HR7I**

**A1 : 30X30 um**

Bias: 1V, Scan length: 2mm

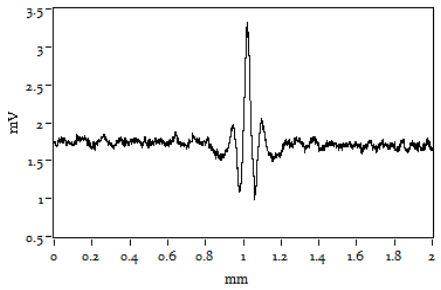


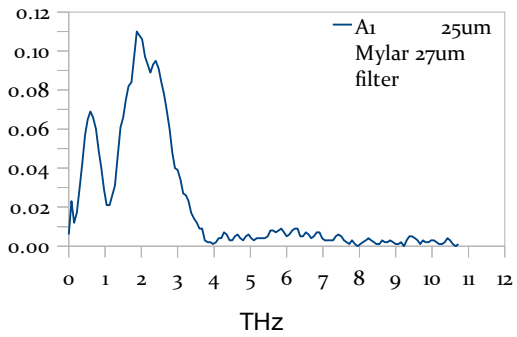


**A2 : 30X30 um**

Bias: 1.2V, Scan Length: 1mm

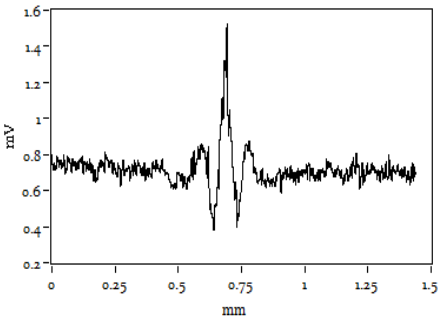


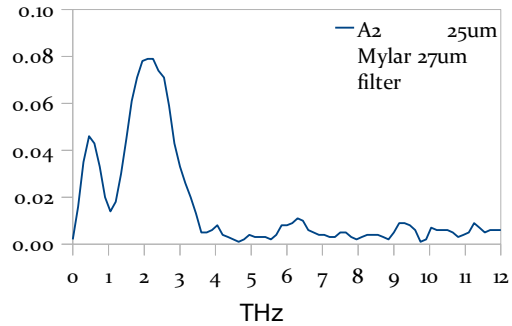


**A3 : 15X30 um**

Bias: 1.52V, Scan Length: 1mm

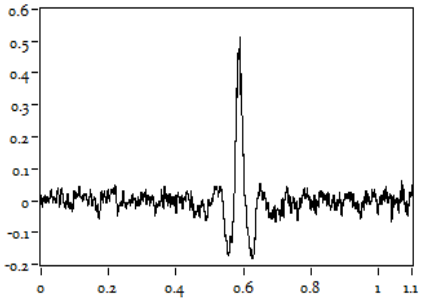

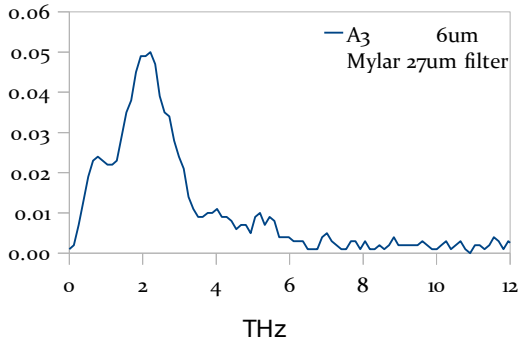

**A4 : 30x30 um**

Bias: 0.94V, Scan Length: 1mm

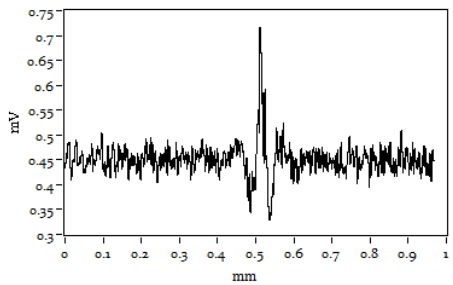


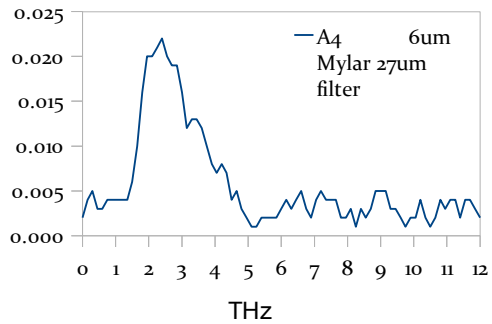


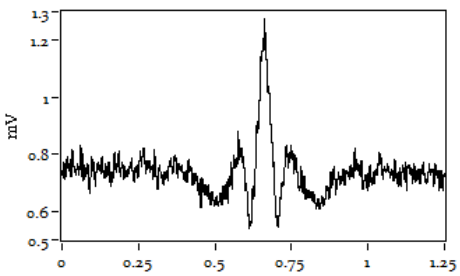


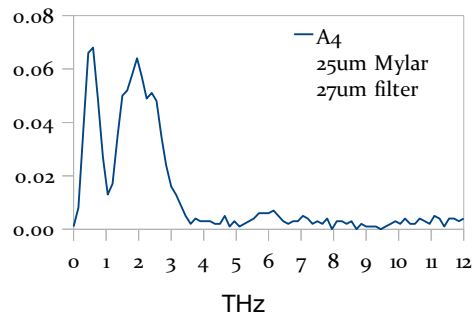


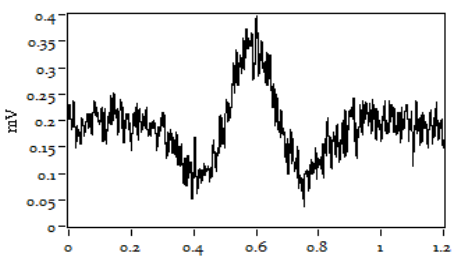


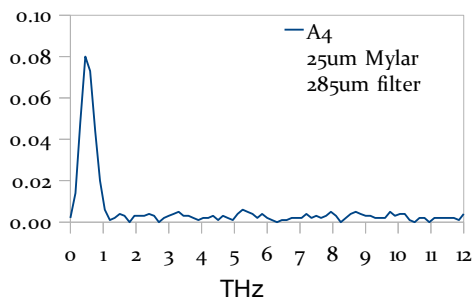


**A5 : 15X30 um**

Bias: 1.64V, Scan length : 1mm

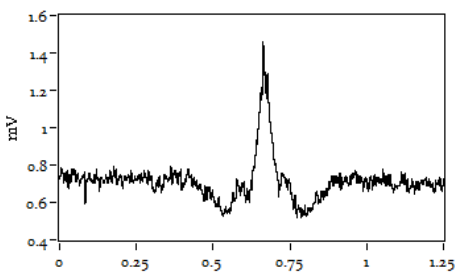


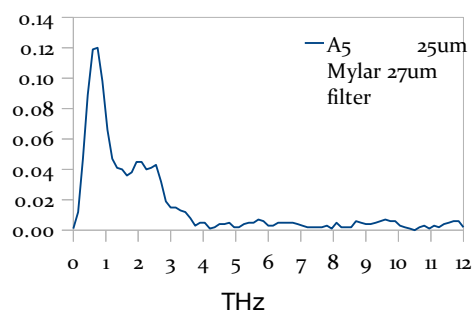

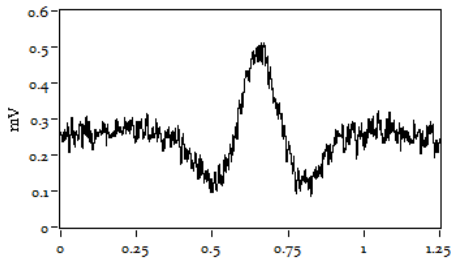


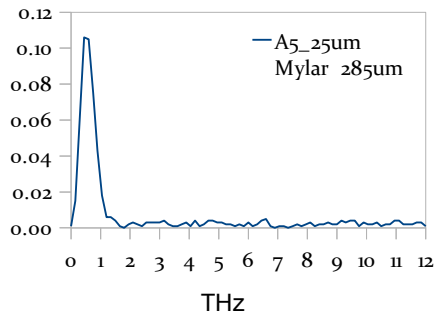


**B1 : 15X30 um**

Bias: 1.4V, Scan Length: 1mm

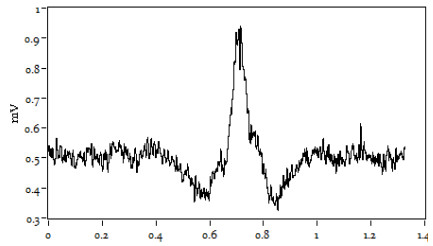


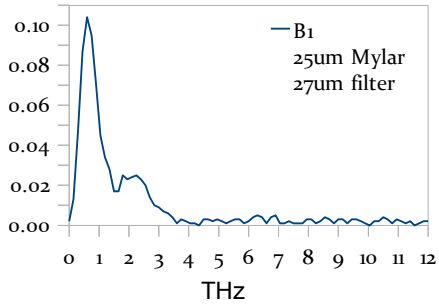


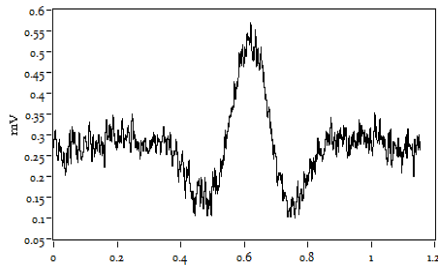


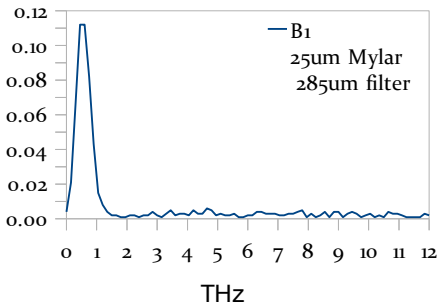


**B2 :30X30 um**

Bias: 1V, Scan Length 2mm

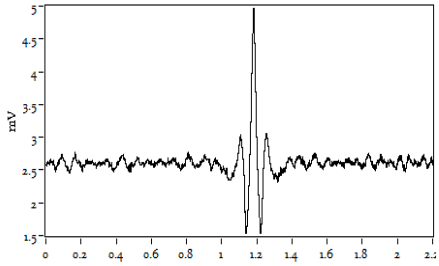


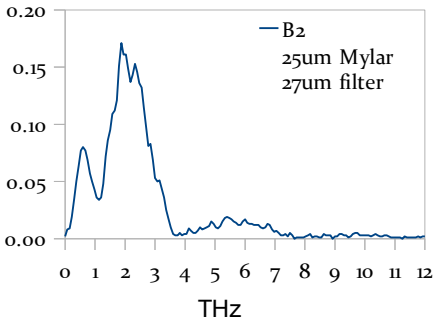

**B3 : 45X30 um**

Bias: 0.94V, Scan Length: 1mm

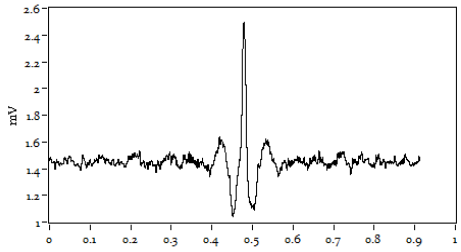


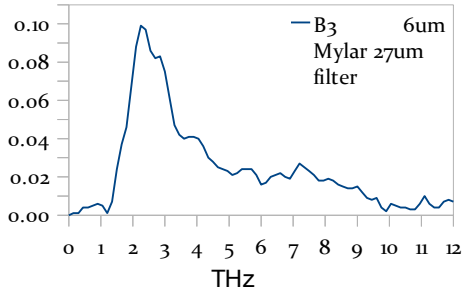


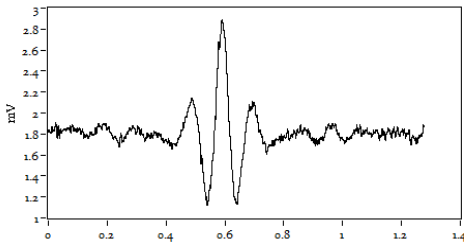


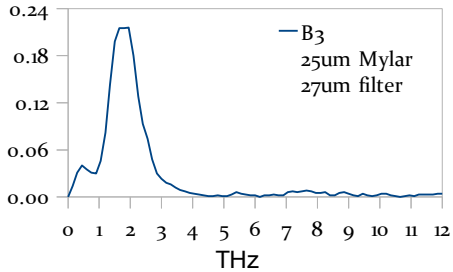


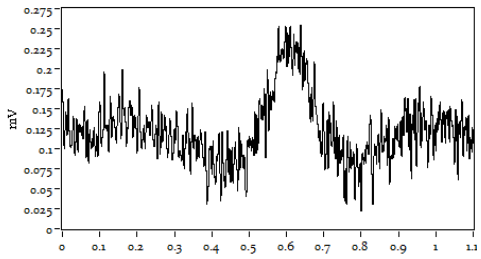


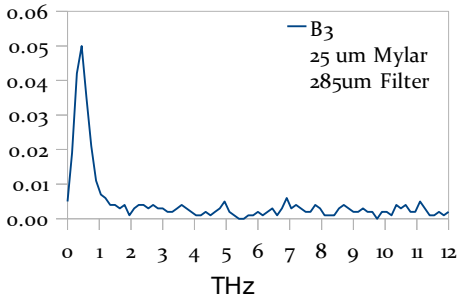


**C1 : 30X30um**

Bias: 1.1V, Scan Length: 1mm

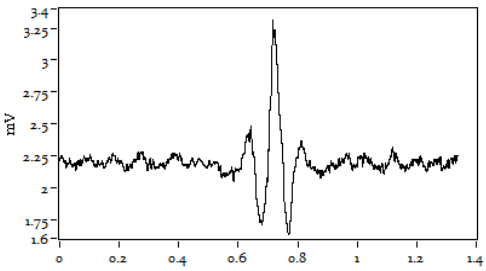


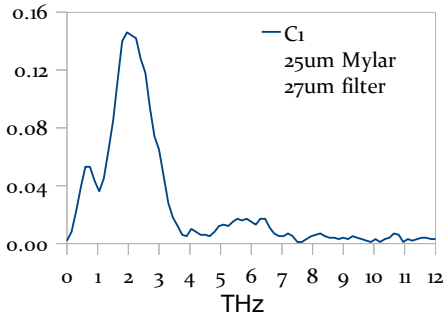

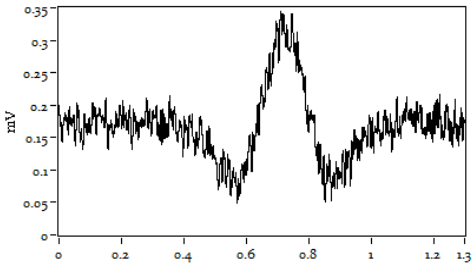


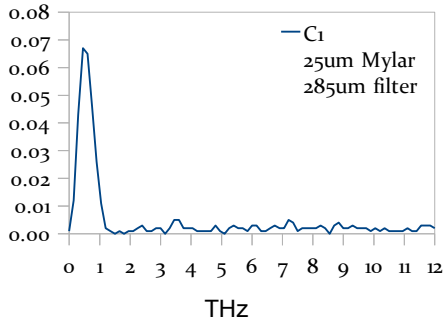


**C2 : 30X30 um**

Bias: 1V, Scan Length: 2mm

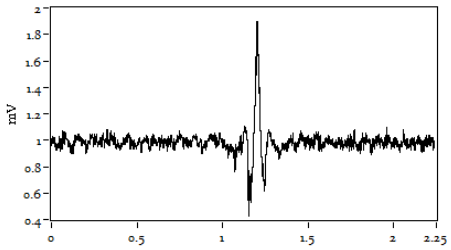


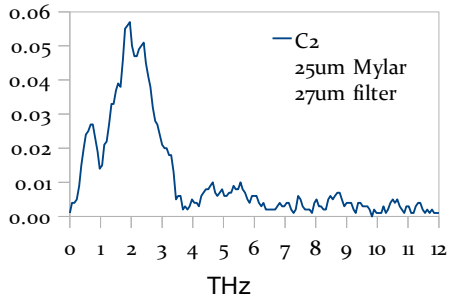


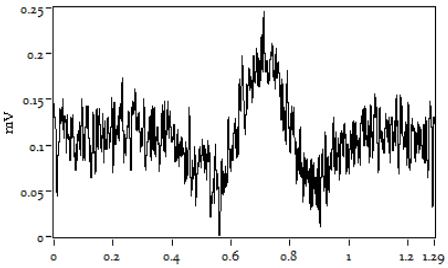


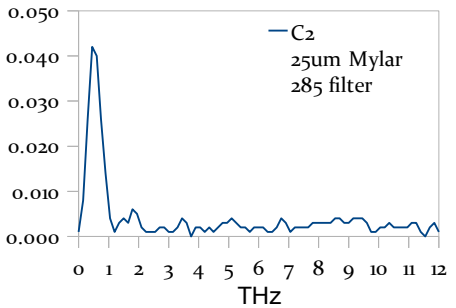


**C3 : 15X30um**

Bias: 1.6V, Scan Length: 1mm

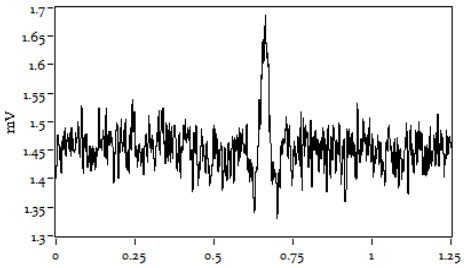


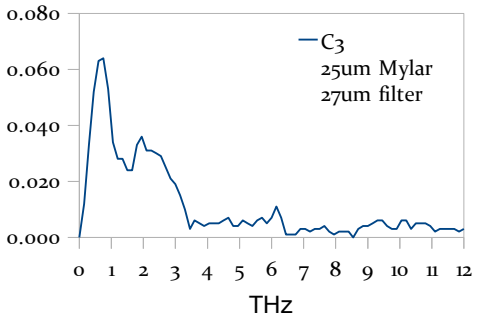

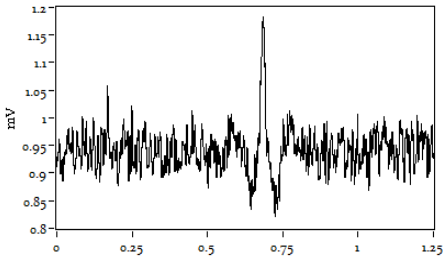


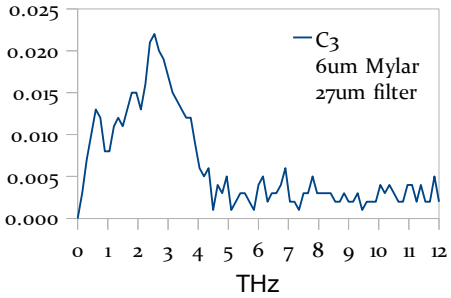


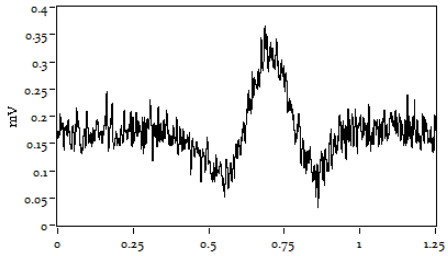


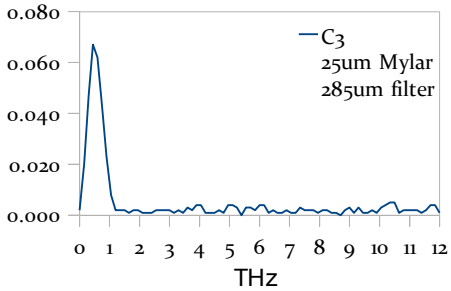


**C4 : 45X30 um**

Bias: 1V, Scan Length: 1mm

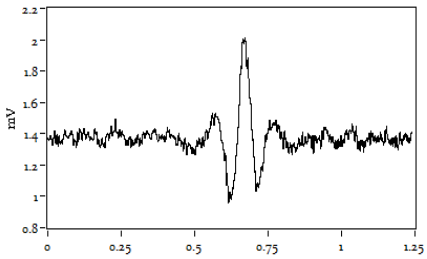


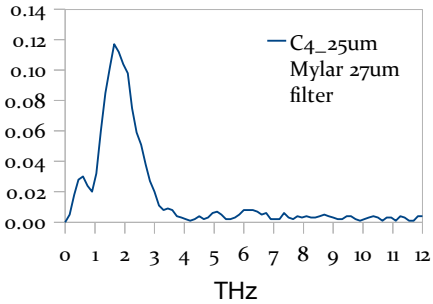


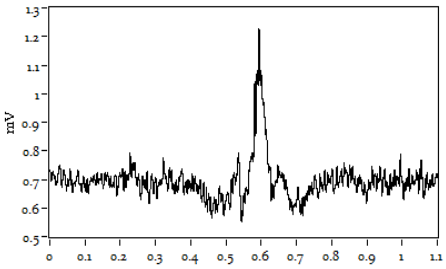


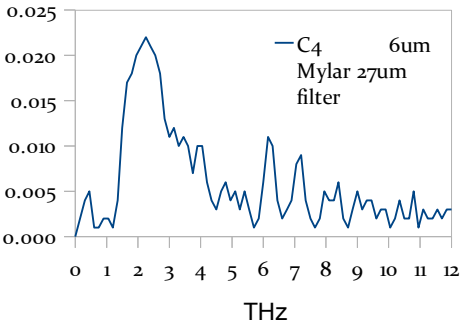

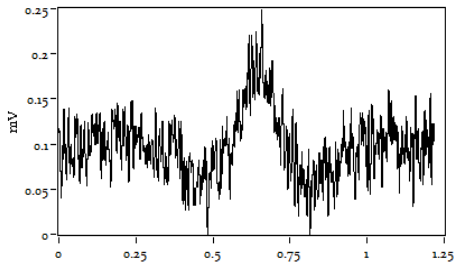


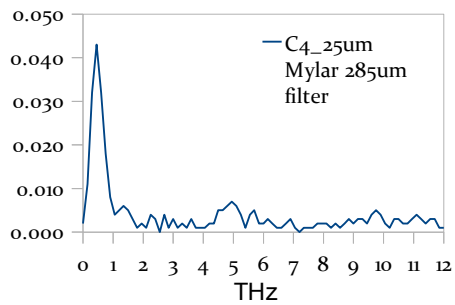


**C5 : 15X30 um**

Bias: 1.2V, Scan Length 2mm

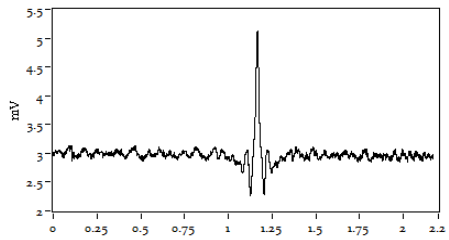


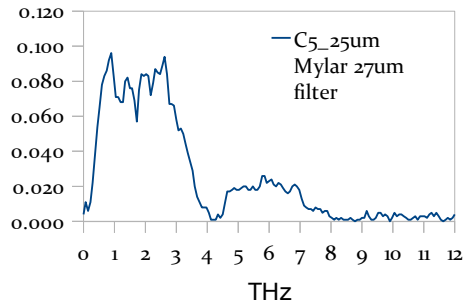


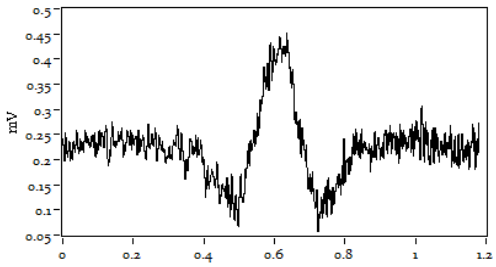


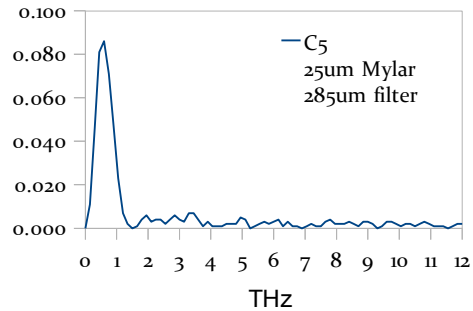


**D1 : 9um Bars**

Scan Length: 1mm

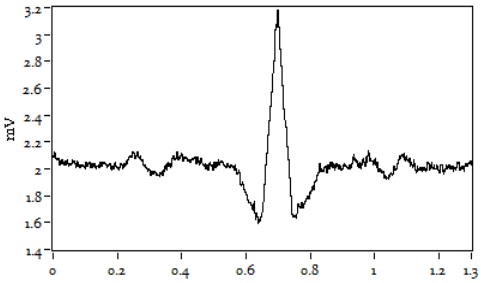


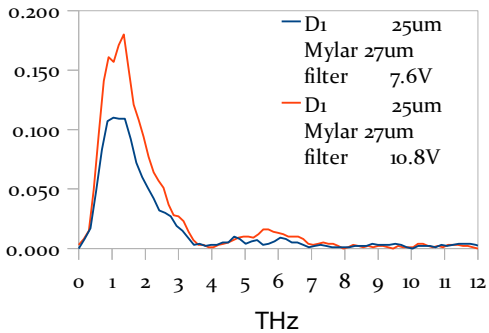

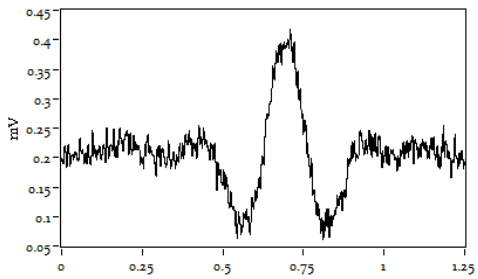


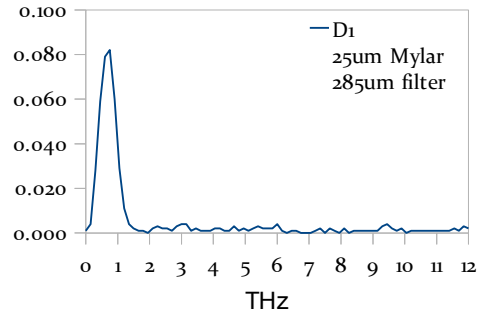


## D2 _ 9um Bars

Bias: 3.44V, Scan Length: 1mm

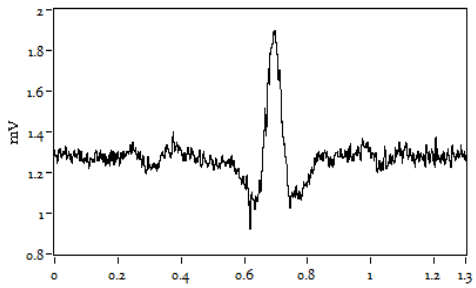


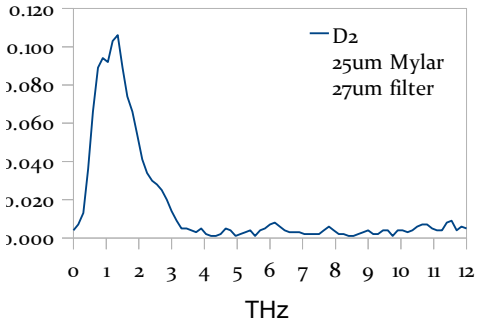

**HR7II**

**A1 : 75X30um**

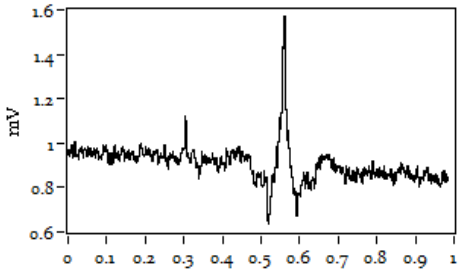


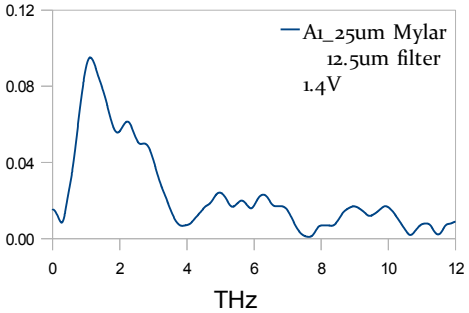


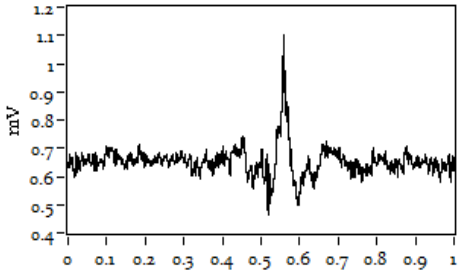


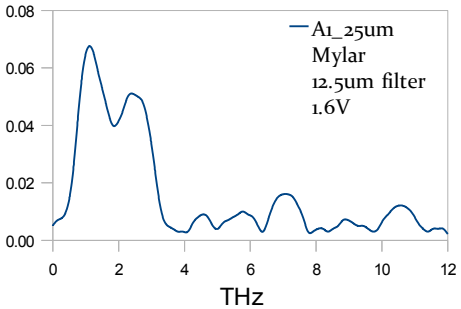


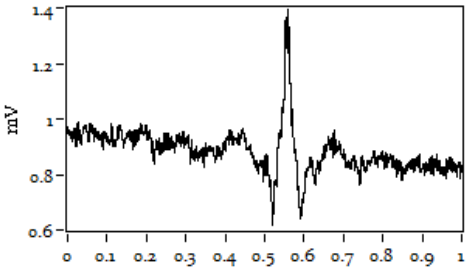


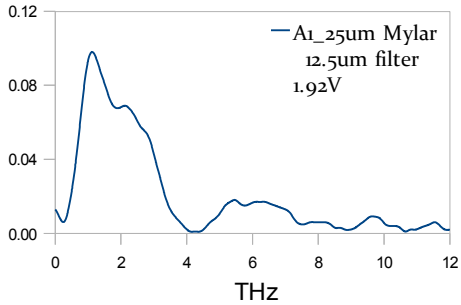


**A2 : 45X30um**

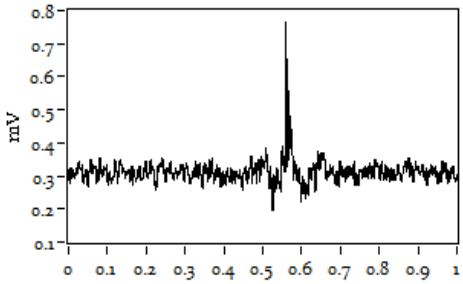


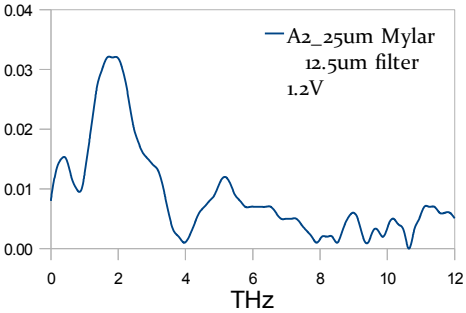

## A4 : 15x30um

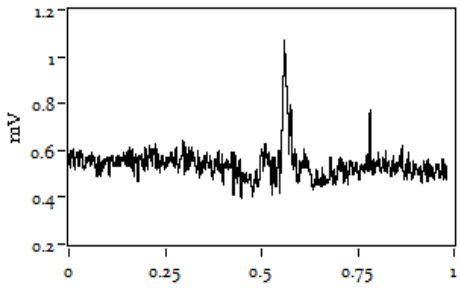


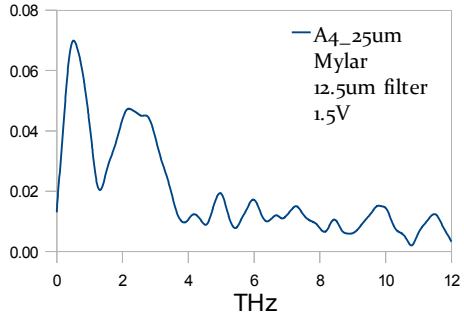


## A5 : 10x30um

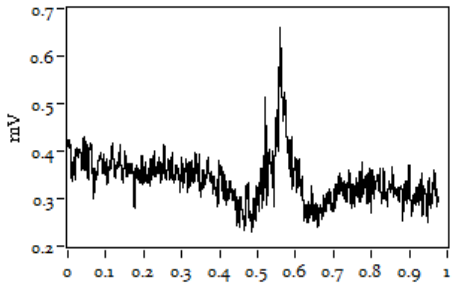


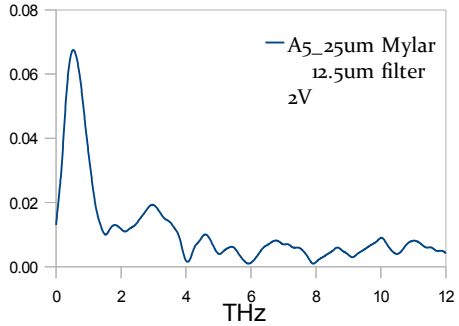


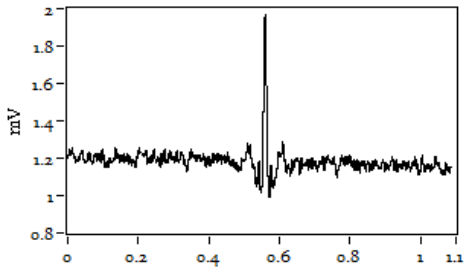


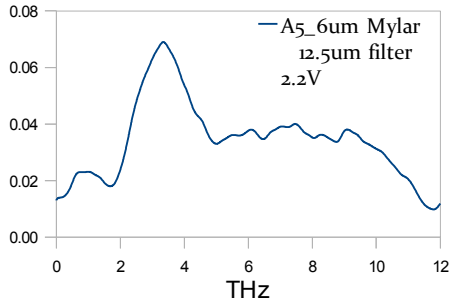


## B1 : 75x30um

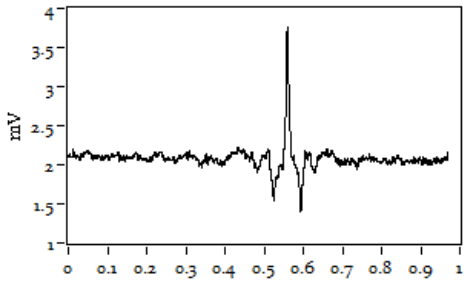


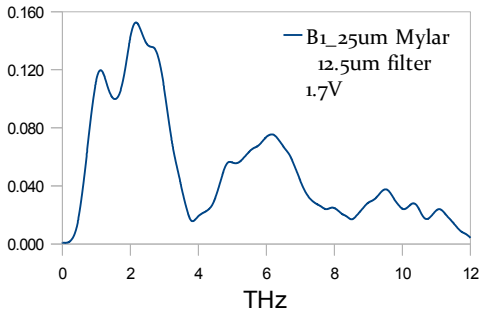

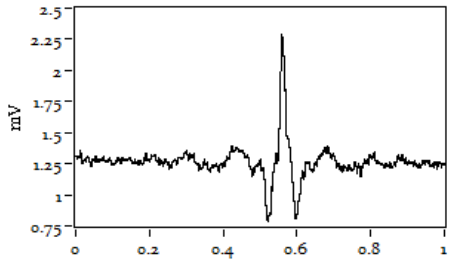
mV

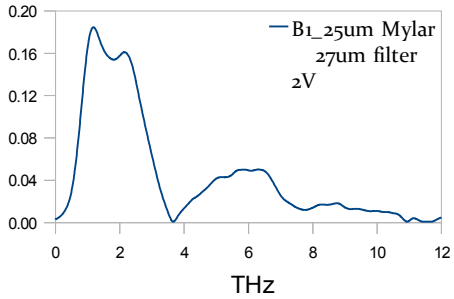
B1_25um Mylar
27um filter
2V
THz

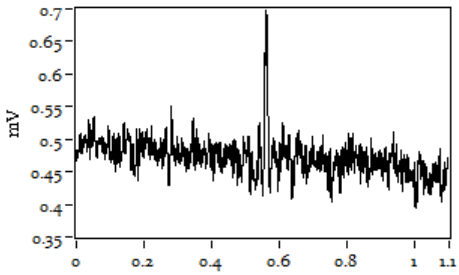
mV

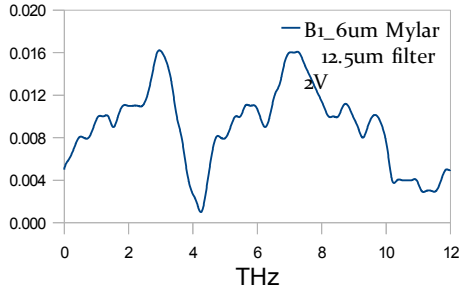
B1_6um Mylar
12.5um filter
2V
THz

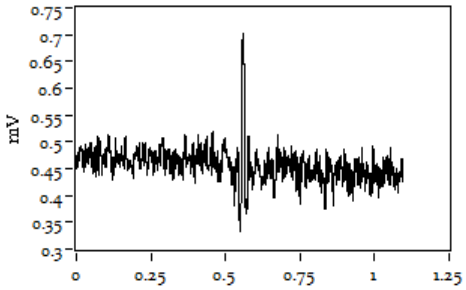
mV

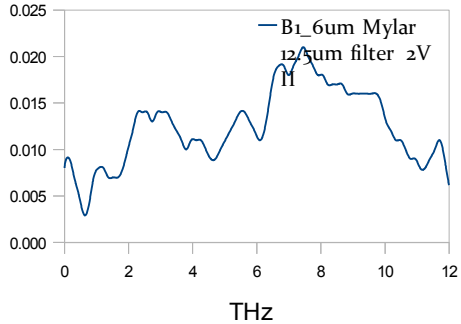
B1_6um Mylar
12.5um filter 2V
THz

## B2 :45x30um

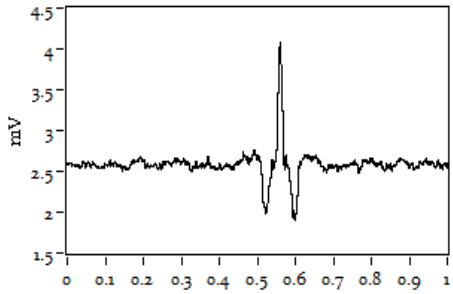
mV

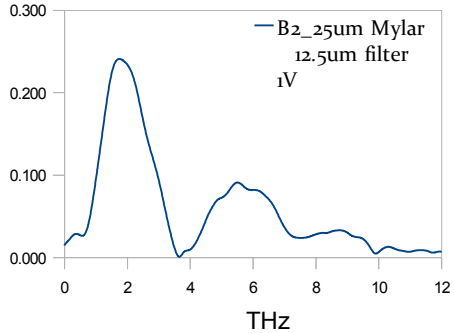
B2_25um Mylar
12.5um filter
1V
THz

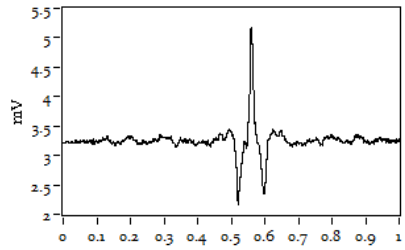
mV

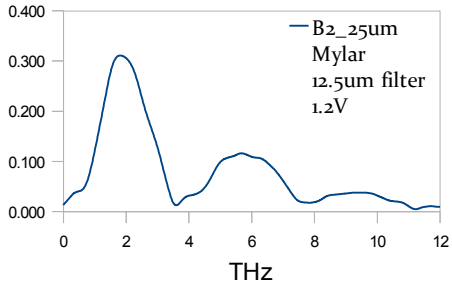
B2_25um
Mylar
12.5um filter
1.2V
THz

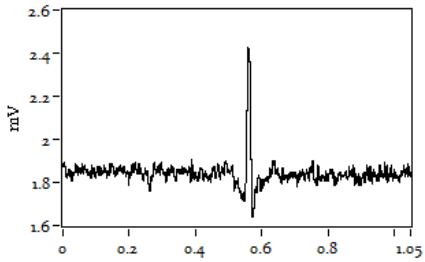
mV

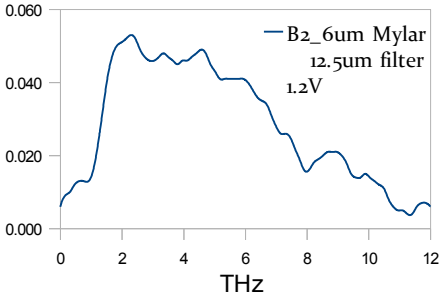
B2_6um Mylar
12.5um filter
1.2V
THz

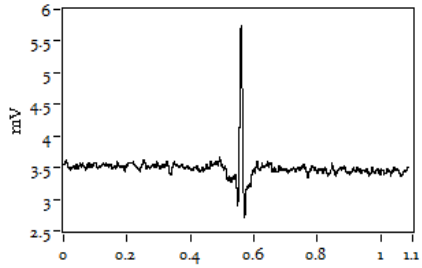
mV

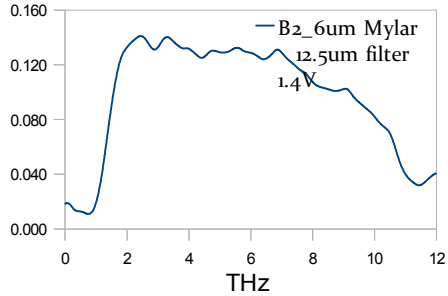
B2_6um Mylar
12.5um filter
1.4V
THz

## B3 : 30x30um

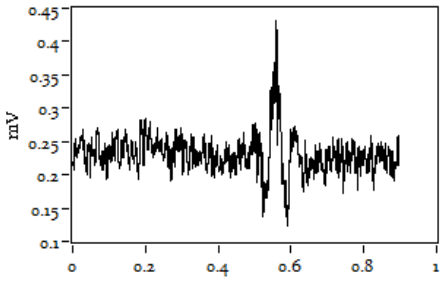
mV

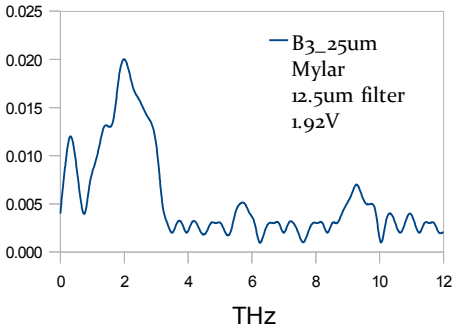
B3_25um
Mylar
12.5um filter
1.92V
THz

## B4 : 15x30um

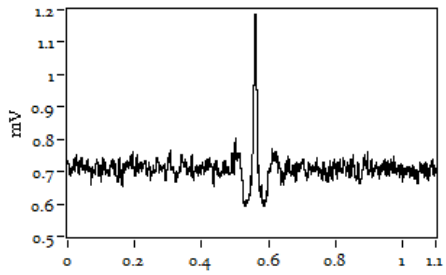


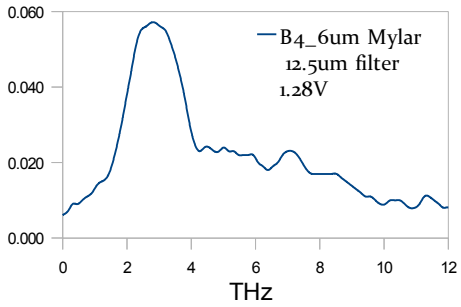


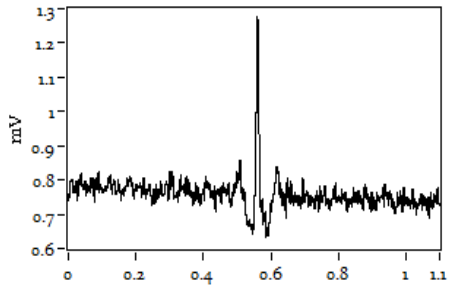


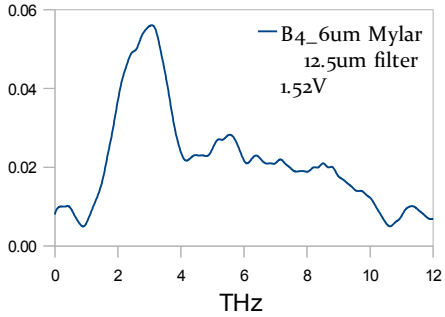


## B5 : 10x30um

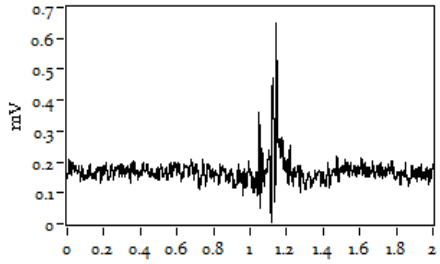


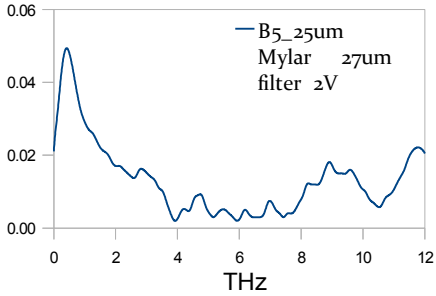


## C1 : 75x30um

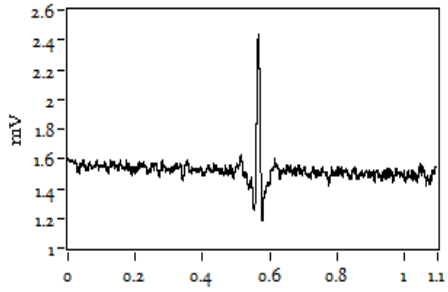


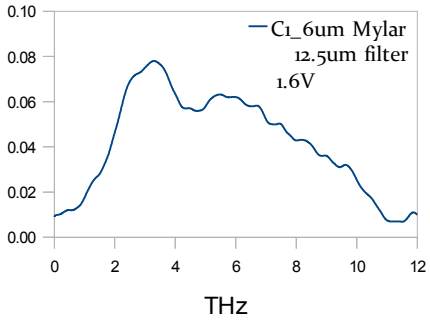

**C4 : 15X30 um**

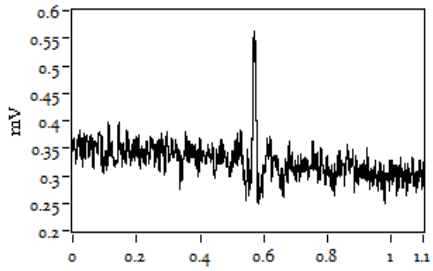


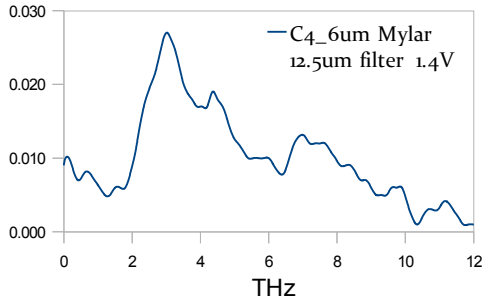


**HR7III**
**A2 : 45X30um – 500nm gap**

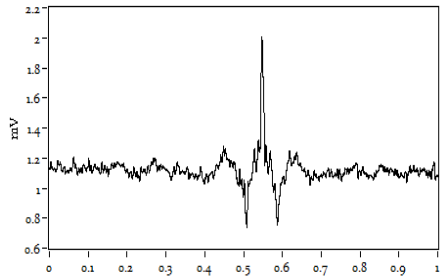


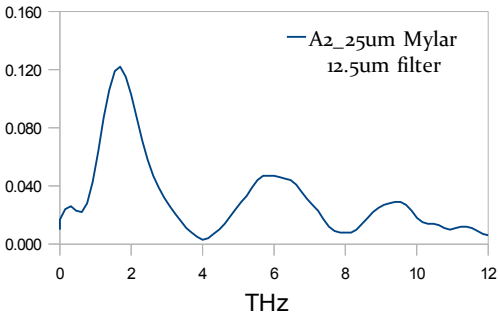


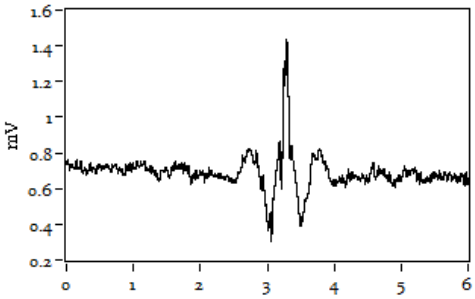


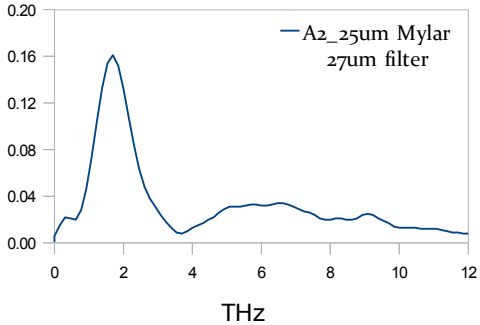

## A3 : 45X30um – 500nm gap

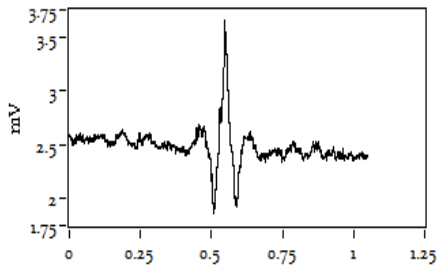


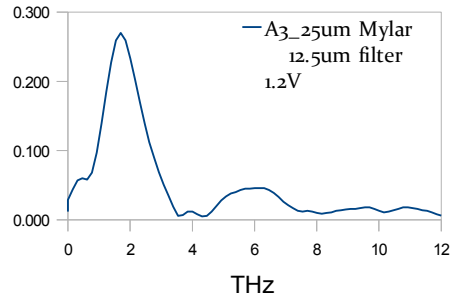


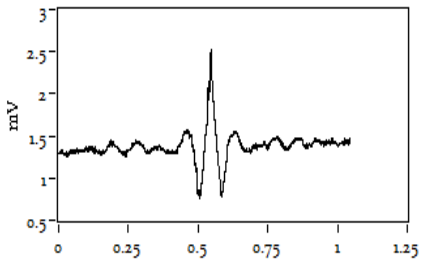


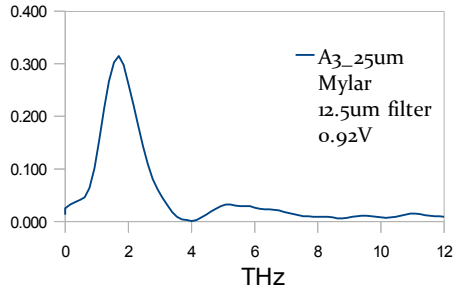


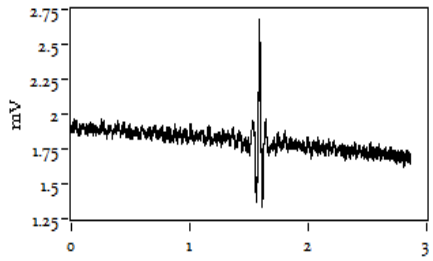


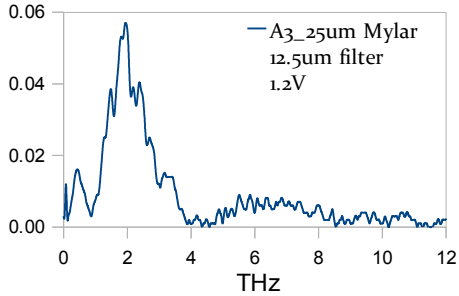


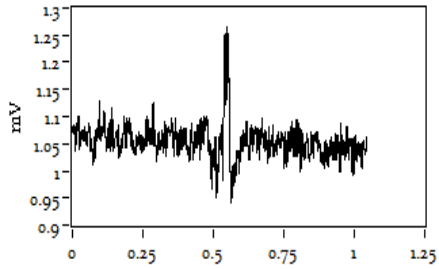


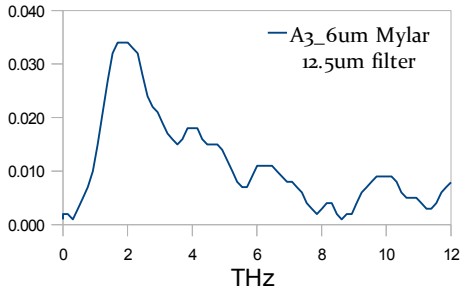

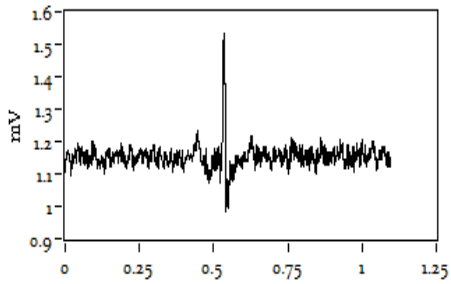


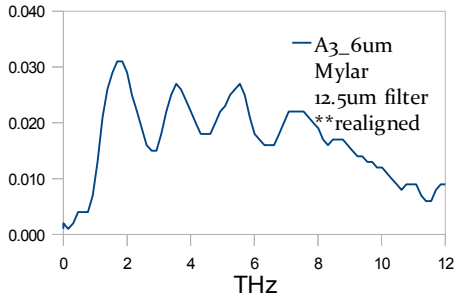


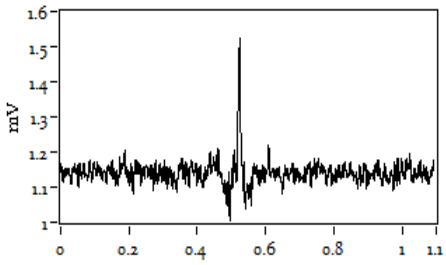


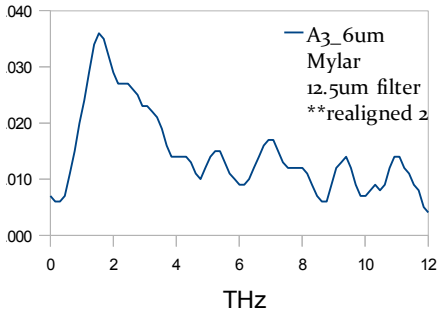


## A4 : 45X30um – 3um gap

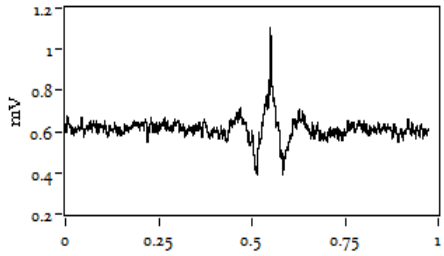


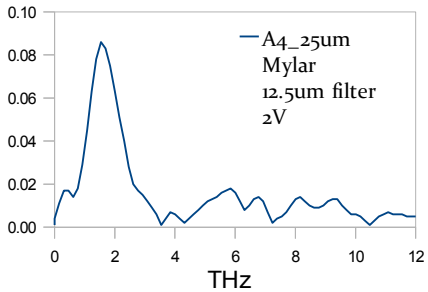


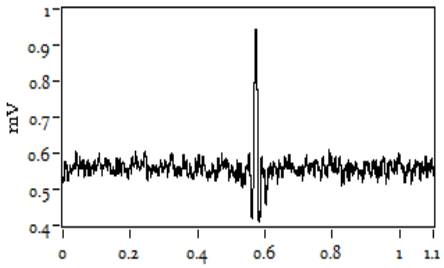


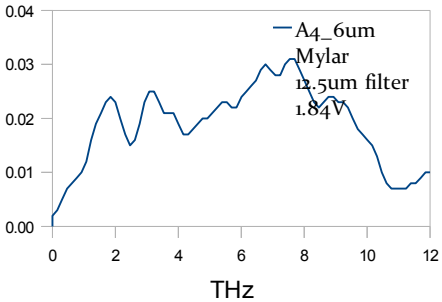

## A5 : 45X30um – 3um gap

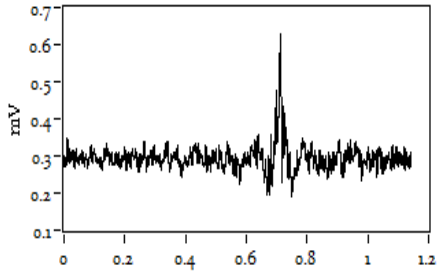


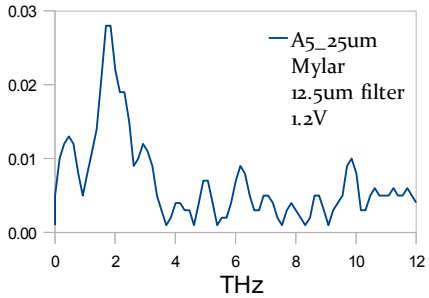


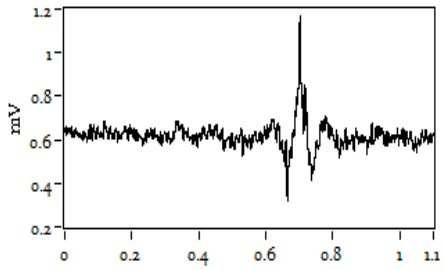


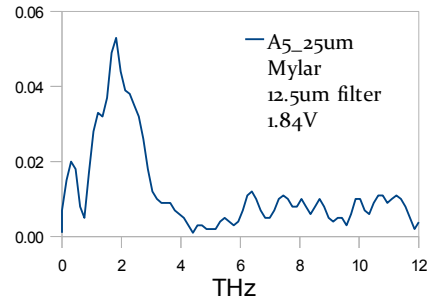


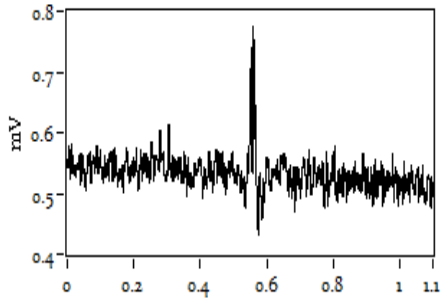


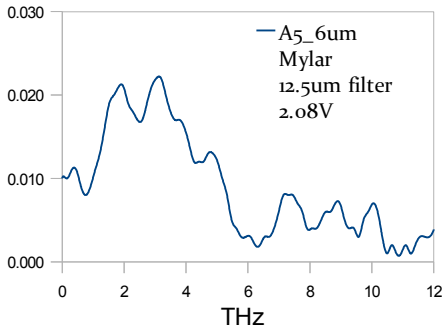


## B1 : 15x15um

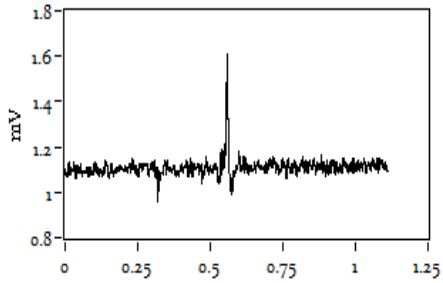


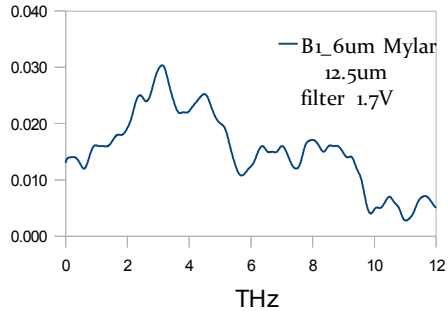

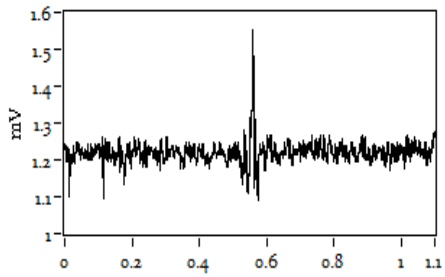
mV
1.6
1.5
1.4
1.3
1.2
1.1
1
0
0.2
0.4
0.6
0.8
1
1.1

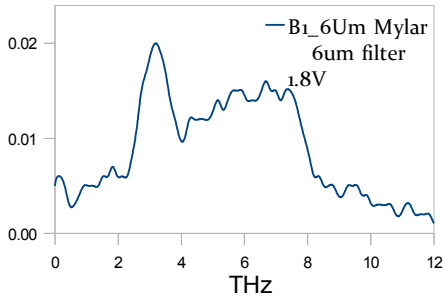
B1_6Um Mylar
6um filter
1.8V
0.02
0.01
0.00
0
2
4
6
8
10
12
THz

**B2 : 15x15um**

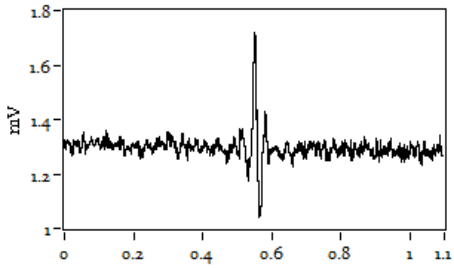
mV
1.8
1.6
1.4
1.2
1
0
0.2
0.4
0.6
0.8
1
1.1

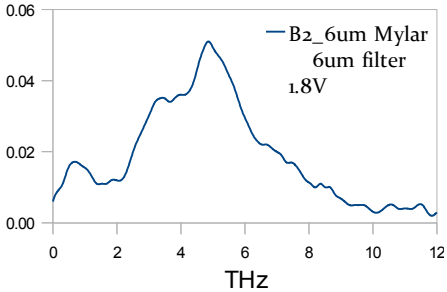
B2_6um Mylar
6um filter
1.8V
0.06
0.04
0.02
0.00
0
2
4
6
8
10
12
THz

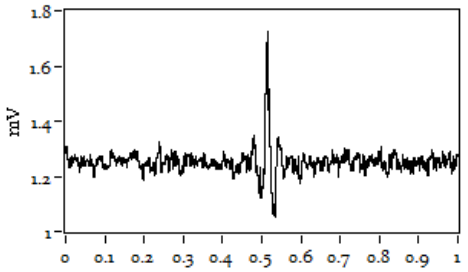
mV
1.8
1.6
1.4
1.2
1
0
0.1
0.2
0.3
0.4
0.5
0.6
0.7
0.8
0.9
1

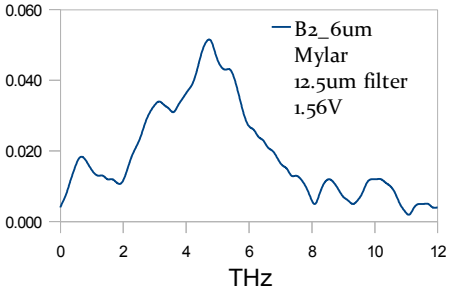
B2_6um
Mylar
12.5um filter
1.56V
0.060
0.040
0.020
0.000
0
2
4
6
8
10
12
THz

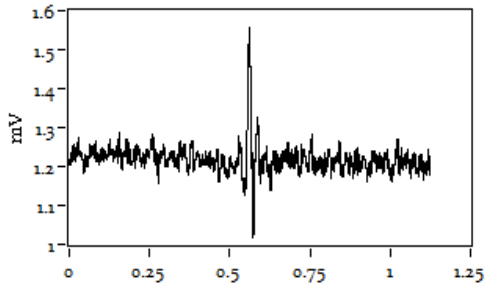
mV
1.6
1.5
1.4
1.3
1.2
1.1
1
0
0.25
0.5
0.75
1
1.25

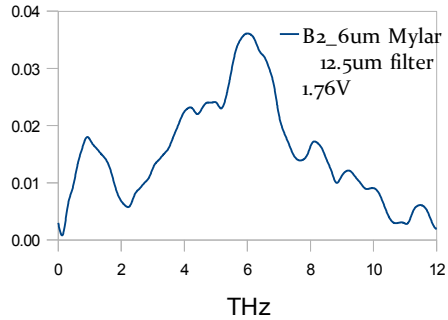
B2_6um Mylar
12.5um filter
1.76V
0.04
0.03
0.02
0.01
0.00
0
2
4
6
8
10
12
THz

**B3 : 15x45um**

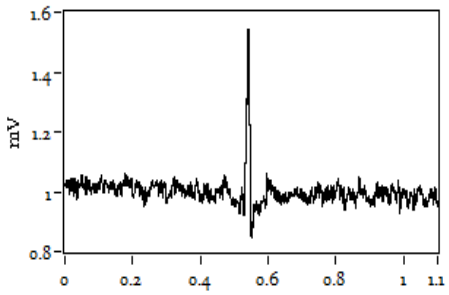


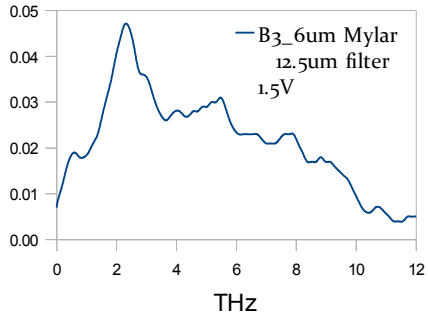


**HR7IV**
**A3: 30X40um**

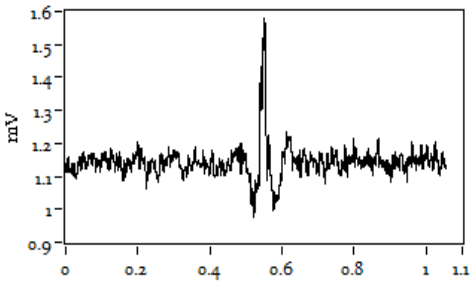


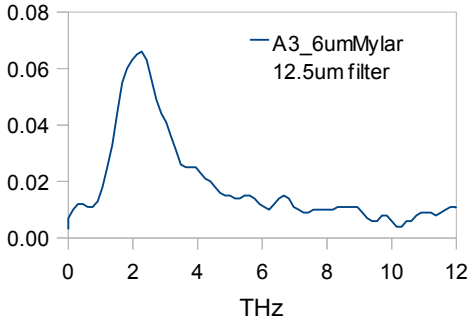


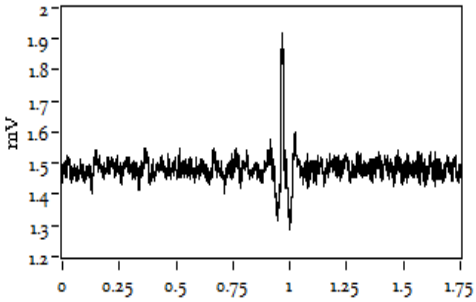


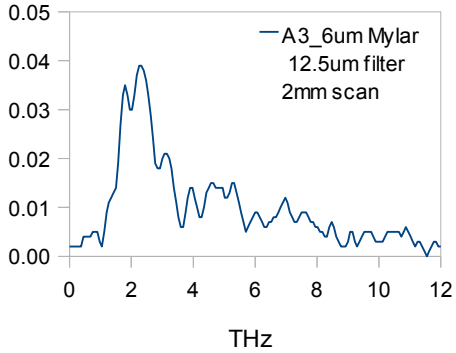

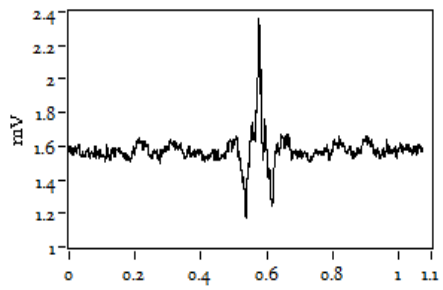


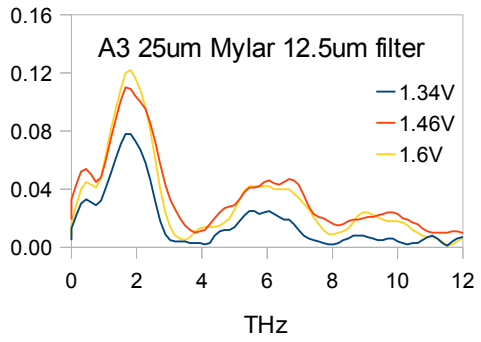


## A4: 30X40um

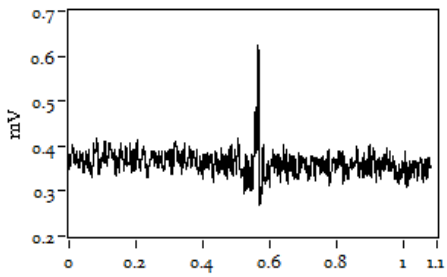


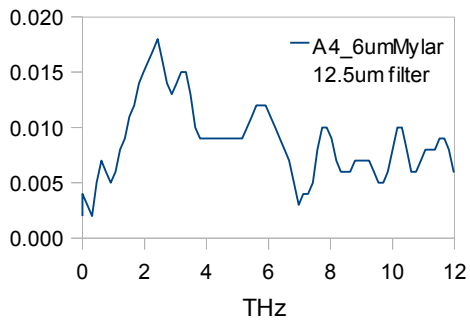


## A5: 45X30um 500nm gap

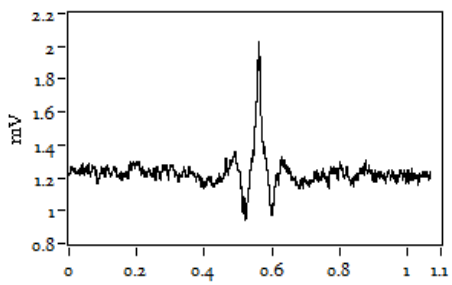


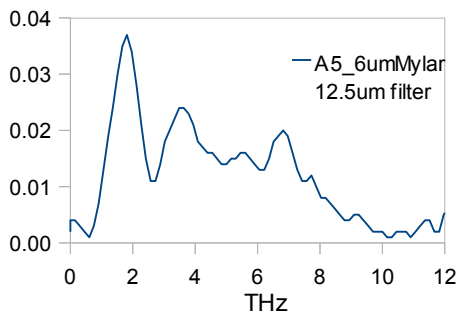


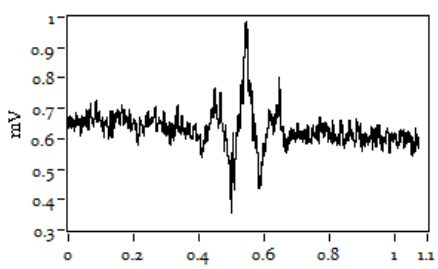


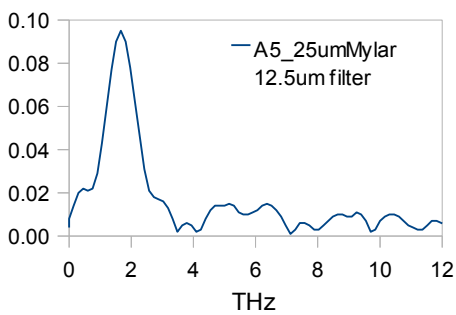

## B1: 30X20um

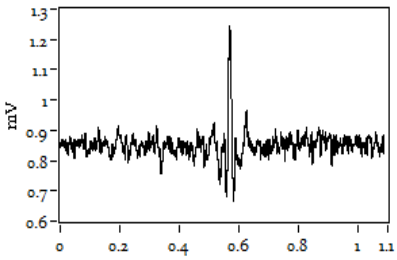


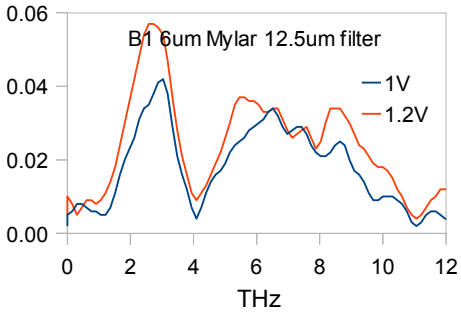


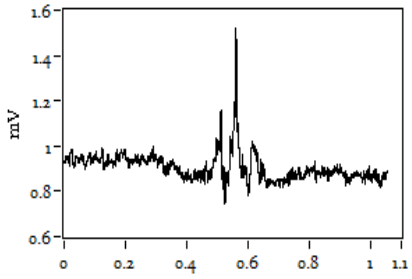


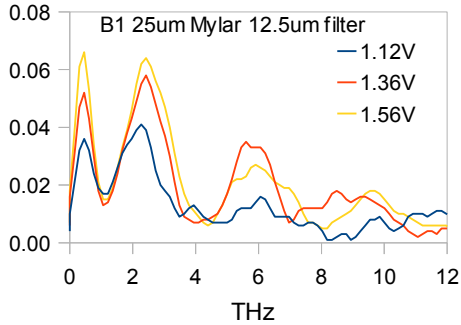


## B2: 30x20um

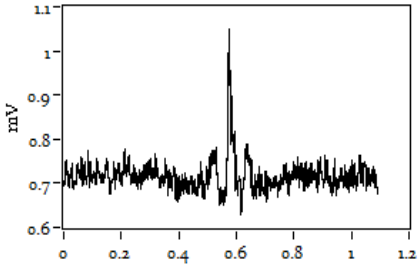


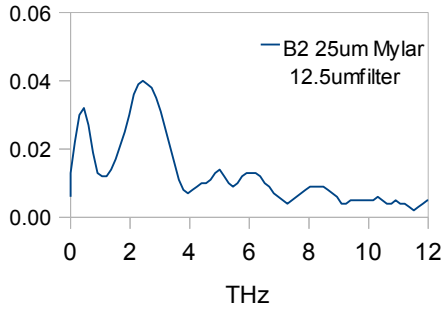


## B3: 30X20um

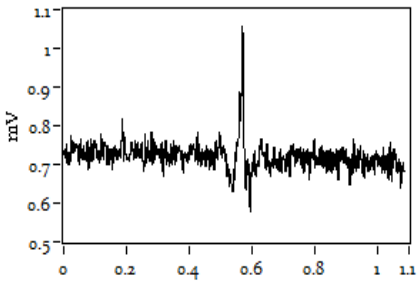


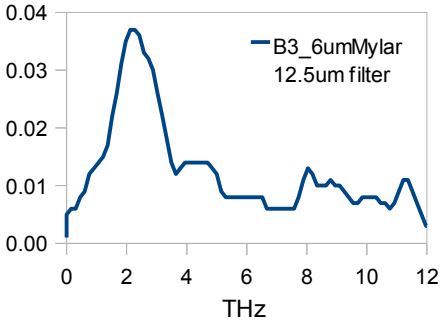

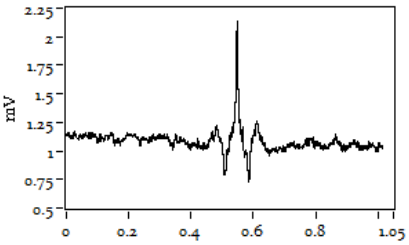


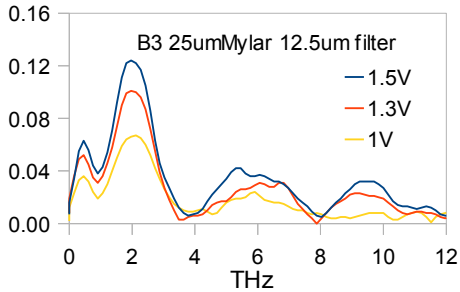


## B5: 9umBars w/PMMA passivation

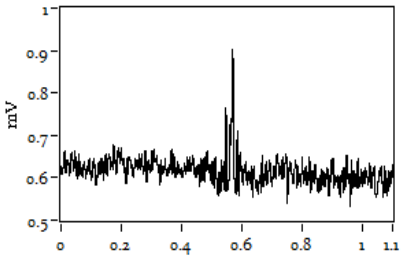


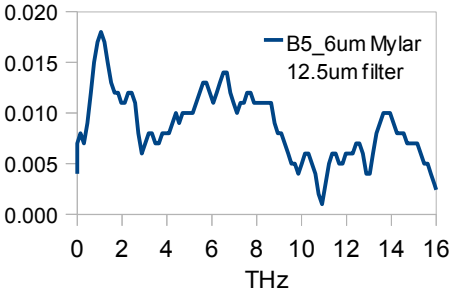


## C1: 9um Bars

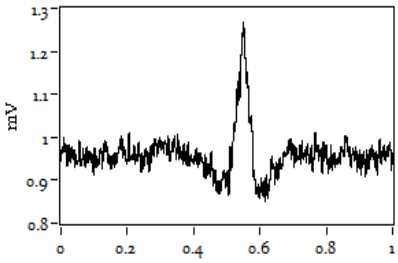


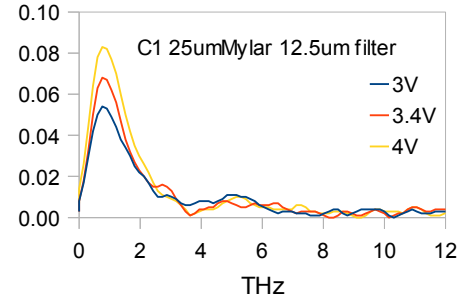


## C3: 9umBars w/ SiO2 passivation

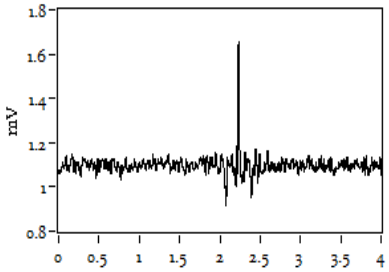


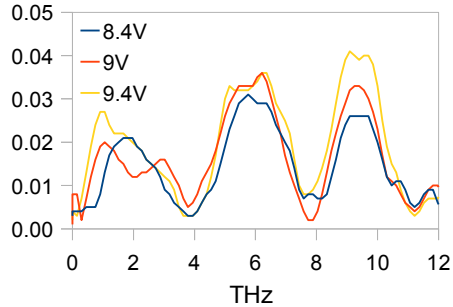

**C4: 9umBars**

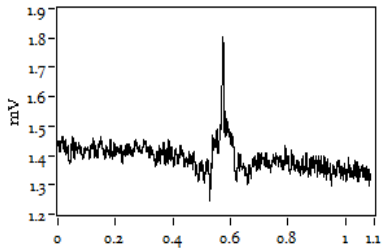


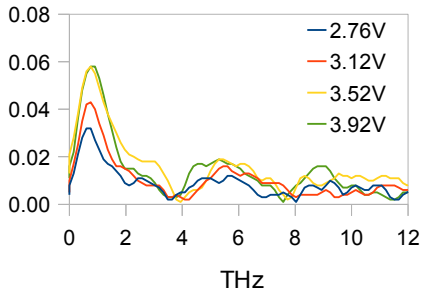


**HR4_A4**
**3.92v, 25um Mylar, 27um Filter**

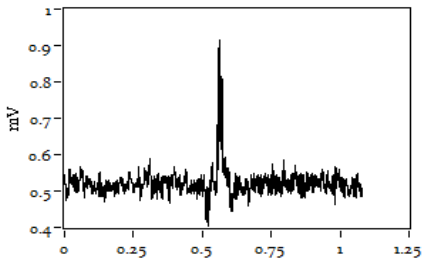


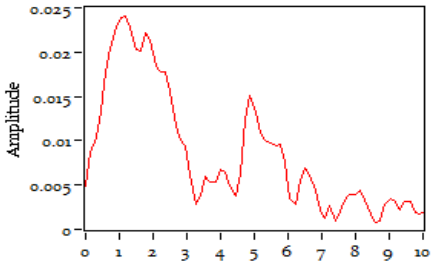


**3.92V, 6um Mylar, 27um Filter**

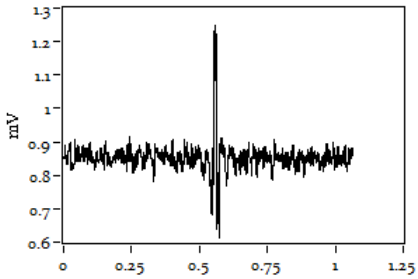


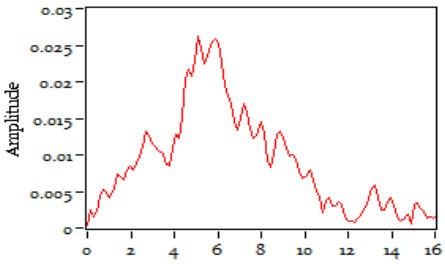

## APPENDIX C

## BOLOMETER FILTER TRANSMISSION CURVES

### a) Bolometer 1

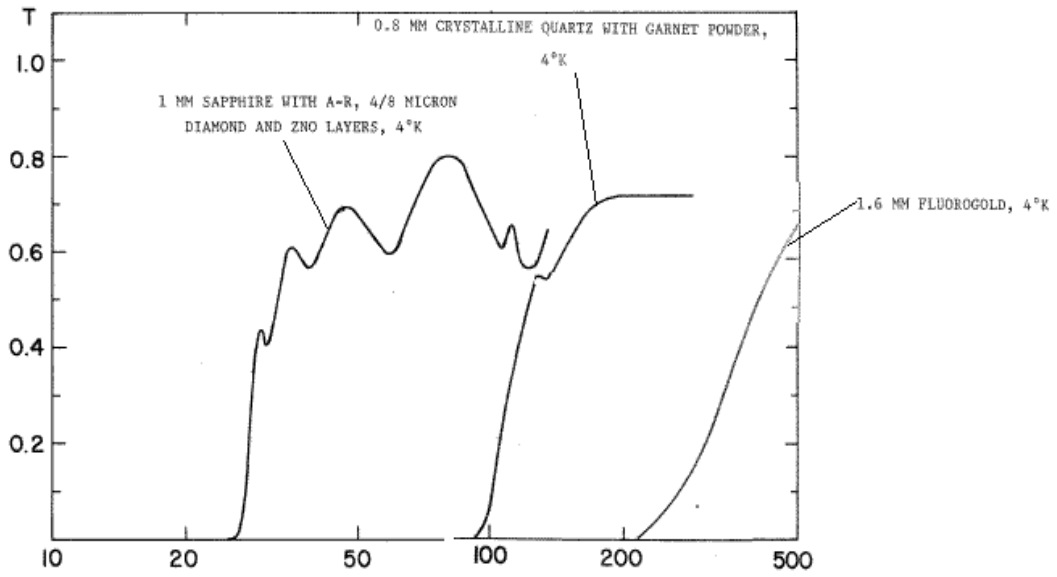


### b) Bolometer 2

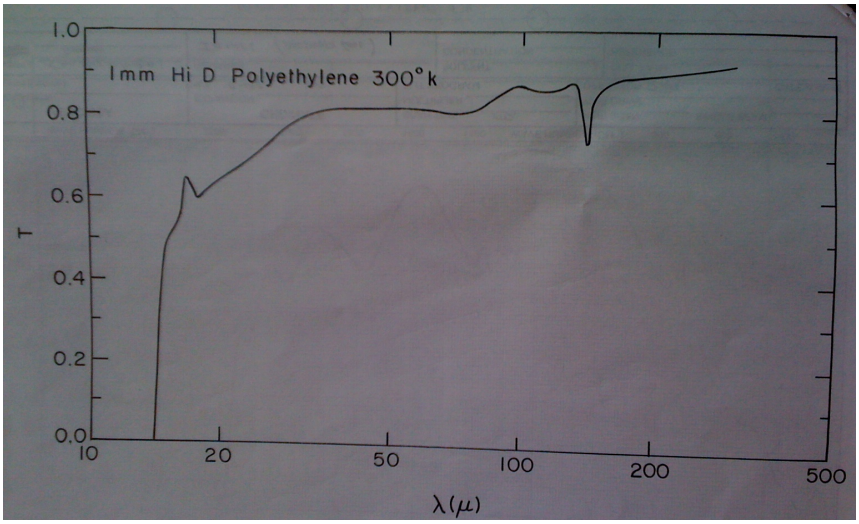

# BIBLIOGRAPHY


[1] K. Fu *et al*., " Terahertz detection in single wall Carbon nanotubes", *Appl. Phys. Lett.*, **92**, pp. 033105-033105-3, 2008.

[2] K. S. Yngvesson *et al.*, "Microwave and Terahertz detection in bundles of single-wall carbon nanotubes", Proc. 33rd International Conference on Infrared, Millimeter and Terahertz Waves, IRMMW-THz Sept. 2008.

[3] D. Mann *et al.*, "Electrically driven thermal light emission from individual single-walled carbon nanotubes", *Nature Nano.*,Vol 2 , pp. 33-38, 2007 .

[4] P. Li *et al*., "Polarized incandescent light emission from carbon nanotubes", Appl. Phys. Lett. **82**, pp. 1763–1765, 2003.

[5] O. V. Kibis *et al.*, "Generation of Terahertz Radiation by Hot electrons in Carbon Nanotubes", Nano Lett., ***7*** (11), pp 3414–3417, 2007.

[6] W. L. Chan *et al*., "Imaging with terahertz radiation," *Rep. Prog. Phys*. **70**(8), pp. 1325-1379, 2007.

[7] E. R. Mueller, "Terahertz Radiation: Applications and Sources," *The industrial physicist*., **9**, Part 4 : 27-30, 2003.

[8] M. Tonouchi, "Cutting-edge terahertz technology," *Nature Photonics,* **1**, pp. 97-105, 2007.

[9] S. Iijima, "Helical Microtubes of Graphitic Carbon". *Nature*, **354**, pp. 56-58, 1991.

[10] P. Avouris *et al*., "Carbon - nanotube photonics and optoelectronics," *Nature Photon.* **2**, pp. 341–350, 2008.

[11] Z. Liu *et al.*, "Carbon nanotubes in biology and medicine: in vitro and in vivo detection, imaging and drug delivery," *Nano Res*. **2**, pp. 85–120, 2009.

[12] A. Bachtold *et al.*, "Logic circuits with carbon nanotube transistors," *Science,* 294, pp. 1317–1320 (2001).

[13] A. Loiseau *et al*. "Synthesis Methods and Growth Mechanisms" in *Understanding Carbon Nanotubes: From Basics to Applications,* Lecture Notes in Physics, Berlin Heidelberg: Springer- Verlag, 2006, vol. 677, pp. 49–130.

[14] Available: *http://en.wikipedia.org/wiki/Carbon_nanotube*

[15] F. Ducastelle *et al*., "*Electronic Structure* " in *Understanding Carbon Nanotubes: From Basics to Applications, Lecture Notes in Physics*, Berlin Heidelberg: Springer- Verlag, 2006, vol. 677, pp. 199–276.

[16] C. L. Kane and E. J. Mele. "Size, Shape and Low Energy Electronic Structure of Carbon Nanotubes," *Phys. Rev. Lett*. **78**, pp. 1932-1935, 1997.

[17] M. V. Fischetti, Solid State Electronics II, *ECE 609 Class Notes (2010).*

[18] P. McEuen, "Nanostructures " in Introduction to Solid State Physics, *8th* ed., Hoboken, NJ, John Wiley & Sons, 2005, Chapter 18, pp. 515-562.

[19] J. W. Mintmire and C. T. White, "Universal Density of States for Carbon Nanotubes, " *Phys. Rev. Lett.* **81**, pp. 2506 -2509, 1998.

[20] F. Leonard, " Metallic Carbon Nanotubes for Current Transport" in *The Physics of Carbon Nanotube Devices,* New York, NY, William Andrew, 2008, pp. 27-50.

[21] S. Roche *et al.* "Transport properties," in *Understanding Carbon Nanotubes: From Basics to Applications, Lecture Notes in Physics*, Berlin Heidelberg: Springer- Verlag, 2006, vol. 677, pp. 335–437.

[22] Z. Yao *et al*., "High-Field Electrical Transport in Single-Wall Carbon Nanotubes", *Phys. Rev. Lett.* **84**, pp. 2941-2944, 2000.

[23] E. Rosencher and B. Vinter, *Optoelectronics,* Cambridge, UK, Cambridge Univ. Press, 2002.

[24] F. R. Arams, *Infrared to mm-wave Detectors*, Dedham MA, Artech House Inc., 1976.

[25] D. Mann *et al.*, "Electrically driven thermal light emission from individual single-walled carbon nanotubes", *Nature Nano.*,Vol 2 , pp. 33-38, 2007.

[26] L. Xie *et al*., "Electroluminescence from Suspended and On-Substrate Metallic Single-Walled Carbon Nanotubes". *Nano Letters*, 9, pp. 1747–1751, 2009.

[27] M. V. Fischetti, ECE 609 Lecture Notes, 2010.

[28] M .E. Portnoi *et al*., "Terahertz applications of Carbon nanotubes*", Superlattices and Microstructures,* 43, pp. 399–407, 2008.

[29] M. E. Itkis *et al*., "Spectroscopic study of the Fermi level electronic structure of single walled Carbon nanotubes", *Nano Lett.* **2**, pp. 155-159 ,2002.

[30] A. Pekker and K. Kamarás, "Wide-range optical studies on various single-walled carbon nanotubes: the origin of the low-energy gap", arXiv:1101.4586v2

[31] F. Borondics and K. Kamaras, "Charge Dynamics in Transparent single-walled carbon nanotube films from optical transmission measurements", *Physical Review* B74, pp. 045431-1 -045431-6, 2006.

[32] Available: *http://en.wikipedia.org/wiki/Terahertz_time-domain_spectroscopy*

[33] C. Schmuttenmaer, "Exploring Dynamics in the Far-Infrared with Terahertz Spectroscopy", *Chem. Rev.*, *104, pp.* 1759-1779, 2004

[34] T. Kampfrath *et al*., "Optical response of single-wall carbon nanotube sheets in the far-infrared spectral range from 1 THz to 40 THz", *Phys. Status Solidi B*, *244*, pp. 3950-3954, 2007.

[35] L. Novotny and B. Hetch, *Principles of Nano-Optics,* New York ,Cambridge University Press, 2006.

[36] D. Seliuta *et al.*, "Terahertz sensing with carbon nanotube layers coated on silica fibers: Carrier transport versus nanoantenna effects", *Appl. Phys.* Lett. 97, pp.073116 -073116-3, 2010.

[37] G. W. Hanson, "Fundamental Transmitting Properties of Carbon Nanotube Antennas", *IEEE Transactions on Antennas and Propagation*, Vol. 53, No. 11, pp. 3426-3435, 2005.

[38] T. Nakanishi and T. Ando, "Optical response of finite-length carbon nanotubes", *J. Phys. Soc. Jpn*. 78 pp. 114708-1 - 114708-9, 2009.

[39] S. A. Maksimenko and G. Y. Slepyan, "Electrodynamic properties of carbon nanotubes," in *Electromagnetic Fields in Unconventional Materials and Structures*, O. N. Singh and A. Lakhtakia, Eds. New York:Wiley, 2000.

[40] S. A. Maksimenko *et al.*, " Carbon nanotube antenna: Far-field, near-field and thermal-noise properties", *Physica E Amsterdam* 40, pp. 2360-2364, 2008.

[41] C. A. Balanis, *Antenna Theory*, 3rd ed. Hoboken, NJ: Wiley, 2005.

[42] K. S. Yngvesson *et al.*, "Microwave and Terahertz detection in bundles of single-wall carbon nanotubes", *33rd International Conference on* Infrared, Millimeter and Terahertz Waves, 2008.

[43] X. Zhao, "Integrated Antennas For Terahertz HEB Mixers" , *PhD Dissertation*, February 2005.

[44] D. F. Fillipovic *et al.*, "Double-Slot Antennas on Extended Hemispherical Dielectric Lenses", *IEEE Transactions on Microwave Theory and Techniques*, Vol. 41, No. 10, pp. 1738-1749, 1993.

[45] P. J. Burke, "Luttinger liquid theory as a model of the gigahertz electrical properties of carbon nanotubes", *IEEE Transactions on Nanotechnology*, vol. **1**, no. 3, pp. 129-144, 2002.

[46] D. Grischkowsky, S. Keiding, M. van Exter, C. Fattinger, "Far-infrared time-domain spectroscopy with terahertz beams of dielectrics and semiconductors", *J. Opt. Safety Am.*B7, 2006–2015 (1990 )

[47] Boston Piezzo Optics: *http://www.bostonpiezooptics.com/*

[48] H. A. Pohl, "Electrode geometries for various dielectrophoretic force laws." *J. Appl. Phys.* 22, 869 (1951)

[49] R. Pethig, "Dielectrophoresis: Status of the theory, technology, and applications", *Biomicrofluidics* 4, 022811 (2010)

[50] M. Dimaki, P. Boggild, "Dielectrophoresis of carbon nanotubes using microelectrodes: a numerical study", *Nanotechnology* 15 1095 (2004)

[51] M. Duchamp, K. Lee, B. Dwir, J. Seo, E. Kapon, L. Forro, A. Magrez, "Controlled Positioning of Carbon Nanotubes by Dielectrophoresis: Insights into the Solvent and Substrate Role", *ACS Nano* 4 (1), 279-284, (2010)

[52] Brewer Science, Rolla, MO. Product used CNTRENE 100 ®

[53] S. Roche, E. Akkermans, O. Chauvet, F. Hekking, J.-P. Issi, R. Martel, G. Montambaux, and P. Poncharal, "Transport properties," in *Understanding carbon nanotubes*, ser. Lecture Notes in Physics, A. Loiseau, P. Launois, P. Petit, S. Roche, and J.-P. Salvetat, Eds. Berlin Heidelberg: Springer- Verlag, vol. 677, pp. 335–437,(2006)

[54] http://www.infraredlaboratories.com/uploads/IRLabs-Bolometers-WEB.pdf

[55] http://www.infraredlaboratories.com/uploads/IRLabs-WCB-WEB.pdf

[56] V. Saptari, "Fourier-transform spectroscopy instrumentation engineering," SPIE Press, Bellingham, WA, (2004).

[57] J. W. Cooley and J. W Tukey. “An algorithm for the machine calculation of complex Fourier series”. *Math. Comput*. 19:297-301, (1965).

[58] Eric Weinstein, “Millimeter/Submillimeter Fourier Transform Spectroscopy of Jovian Planet Atmospheres”, *PhD Dissertation* (1996)

[59] C.C. Homes, “Fourier Transform Infrared Spectroscopy”, http://infrared.phy.bnl.gov/pdf/homes/fir..pdf

[60] F. Kreupl, A. P. Graham, M. Liebau, G.S. Duesberg, R. Seidel, E. Unger, " Carbon Nanotubes for Interconnect Applications," *IEDM Tech. Dig*., pp. 683 - 686, (2004)

[61] E. Bekyarova, M. E. Itkis, N. Cabrera, B. Zhao, A. Yu, J. Gao and R. C. Haddon, “Electronic Properties of Single-Walled Carbon Nanotube Networks,” *J. Am. Chem. Soc*., 127, 5990, 2005.

[62] A. Javey, J. Guo, M. Paulsson, Q.Wang, D. Mann, M. Lundstrom and H. Dai, “High-Field, Quasi-Ballistic Transport in Short Carbon Nanotubes,” *Cond-mat/0309242*.

[63] S. Roche, E. Akkermans, O. Chauvet, F. Hekking, J.-P. Issi, R. Martel, G. Montambaux, and P. Poncharal, “Transport properties,” in *Understanding carbon nanotubes*, ser. Lecture Notes in Physics, A. Loiseau, P. Launois, P. Petit, S. Roche, and J.-P. Salvetat, Eds. Berlin Heidelberg: Springer- Verlag, vol. 677, pp. 335–437, 2006.

[64] Z. Yao, C.L. Kane and C. Dekker, “High-Field Electrical Transport in Single-Wall Carbon Nanotubes,” *Phys. Rev. Lett.*84, p. 2941, 2000.

[65] A. Javey, P. Qi, Q.Wang, H. Dai, “Ten- to 50-nm-long quasi-ballistic carbon nanotube devices obtained without complex lithography,” *Proc. Natl. Acad. Sci. U. S. A.* 2004, 101, 13408.

[66] V. Derycke, R. Martel, J. Appenzeller, Ph. Avouris, “Controlling doping and carrier injection in carbon nanotube transistors,” *Appl. Phys. Lett.* **80**, 2773, 2002.

[67] E. Pop, D. Mann, K. E. Goodson, H. Dai, "Electrical and Thermal Transport in Metallic Single-Wall Carbon Nanotubeson Insulating Substrates," *J. Appl. Phys.*, *101*, 93710, 2007.

[68] M. C. Llaguno, J. Hone, A. T. Johnson, and J. E. Fischer, "Thermal Conductivity of Single Wall CarbonNanotubes: Diameter and Annealing Dependence," AIP Conference Proceedings 591, 384, 2001.

[69] J. Ruze, "Lateral Feed Displacement in a Paraboloid," IEEE *Trans. Antennas Propagation,* September, 1965.

[70] K.S. Yngvesson, K. Fu, B. Fu, R. Zannoni, J. Nicholson, S.H. Adams, A. Ouarraoui, J. Donovan and E. Polizzi, "Experimental detection of terahertz radiation in bundles of single walled carbon nanotubes," Proc. 19th Intern. Symp. Space Terahertz Technol., Groningen, The Netherlands, April 28-30, 2008.

[71] E. Carrion, M. Muthee, Z. Chen, J. Nicholsosn, E. Polizzi, and K.S. Yngvesson. "Single Wall Carbon Nanotube (SWCNT) Devices as THz detectors and Mizers," Proc. 21th Intern. Symp. Space Terahertz Technol., Oxford, March 23-25, 2010.

[72] M. E. MacDonald and E. N. Grossman, "Niobium microbolometers for far-infrared detection," *IEEE Trans. Microwave Theory Tech.*, vol. 43, pp. 893–896, Apr.,1995.

[73] U.R. Pfeiffer, and E. Ojefors, "Terahertz imaging with CMOS/BiCMOS process technologies," 36th European solid-state circuits Conference. 13–17.09, 2010.